

University of Mosul
College of Electronic Engineering



Investigation into Metamaterial Applications for Microwave Devices

A Dissertation Submitted by

Mamoon Ammar Al-atrakchii

To

The Council of College of Electronic Engineering

University of Mosul

In Partial Fulfillment of the Requirements

For the Degree of Master of Sciences

In

Communication Engineering

Supervised by

Prof. Dr. Khalil Hassan Sayidmarie

Prof. Dr. Raed A. Abd-Alhameed

2019 A.C.

1440 A.H.



Supervisor's Certification

We certify that the dissertation entitled (Investigation into metamaterial applications for microwave devices) was prepared by Mamoon A. Al-atrakchii under our supervision at the Department of Communication Engineering, University of Mosul, as a partial requirement for the Master of Science Degree in Communication Engineering.

Signature: 

Name: Prof. Dr. Khalil H. Sayidmarie

Department of Communication Engineering
/Ninevah University

Date: 12/7/2019

Signature: 

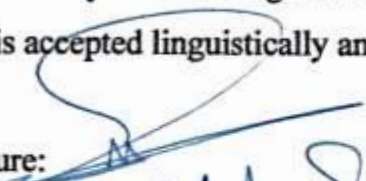
Name: Prof. Dr. Raed A. Abd-Alhameed

School of Electrical Eng. and Computer
Science / Bradford University / UK

Date: 12 July 2019

Report of Linguistic Reviewer

I certify that the linguistic reviewing of this dissertation was carried out by me and it is accepted linguistically and in expression.

Signature: 

Name: Dr. Maher Sami Hassan

Date: August 3rd 2019

Report of the Head of Department

I certify that this dissertation was carried out in the Department of Communication Engineering. I nominate it to be forwarded to discussion.

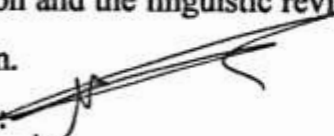
Signature: 

Name: Dr. Younis M. Abbosh // Dr. mahmed, A. meh mod

Date: 4/8/2019

Report of the Head of Postgraduate Studies Committee

According to the recommendations presented by the supervisors of this dissertation and the linguistic reviewer, I nominate this dissertation to be forwarded to discussion.

Signature: 

Name: Dr. Younis M. Abbosh / DR. Mehmed. A. mah mod

Date: 4/8/2019

Abstract

Microstrip band-reject filters for the WLAN applications using new metamaterial approach are proposed in this present work. The proposed filters operate on a common resonant element in the form of a slot that is folded to reconstruct a U-shape structure and embedded into a microstrip line. The length of the slot is $\frac{1}{4}$ the effective wavelength, and its width is no more than that of the microstrip line. This is a considerable size reduction in comparison with the filters, using resonant elements like rings or coupled short-circuited and open-circuited stubs. The first of the four proposed filters uses a single U-shaped slot, while in the other three filters two U-slots are placed in face-to-face, back-to-back, and interlaced configurations. The designed filters are investigated using the CST Microwave Studio.

The two U-slots structure shows a better performance compared to that of the single U-slot, whereas, the interlaced U-slot provides a wider spectrum band. The folding of the slot into the U-shape results in E-field vectors inside the two legs in opposite directions. Thus, the radiation from the slot is minimal. The effective permittivity and permeability are extracted from the S-parameters to confirm the operation of metamaterial. The filters are designed and tested using a vector network analyzer.

The frequency selective property of the U-shape slot is utilized for Frequency Selective Surfaces (FSS). The conducting strips printed on a dielectric substrate and the slots in a conducting screen are proposed and investigated as FSS using the unit cell approach provided by CST Microwave Studio.

The E-field direction of the incident plane wave with respect to the slot or strip controls the FSS behavior. The electric field and the current density are examined inside the slot and on the strip which shows that the resonance is

linearly proportional to slot or strip length when it is an integer multiple of half the guided wavelength. The far-field radiation confirms the transfer characteristics of a band-reject property of U-shaped strip and band-pass property of U-shaped slot.

TABLE OF CONTENTS

Subject		Page
Abstract		I
Table of Contents		III
List of Figures		VI
List of Tables		XIII
List of abbreviations		XIV
List of Symbols		XV
CHAPTER ONE		
INTRODUCTION		
1.1	Preface	1
1.2	Literature Review	2
1.3	Aims of The Dissertation	8
1.4	Thesis Layout	9
CHAPTER TWO		
BASICS OF METAMATERIALS AND THEIR APPLICATIONS		
2.1	Introduction	10
2.2	Properties of Metamaterials	10
2.3	Realization of Metamaterials	14
2.4	Estimating the Effective Permittivity and Permeability	18
2.5	Applications of the Metamaterials	20
2.5.1	Metamaterials as Transmission Lines	20
2.5.2	Superlens	21
2.5.3	Clocking Devices	22

Subject		Page
2.5.4	Metamaterial Antennas	23
2.5.5	Couplers	24
2.5.6	Microwave Filters	25
2.5.6.1	Band Pass Filters (BPF)	26
2.5.6.2	Band Stop Filters (BSF)	27
2.5.6.3	Low Pass Filters (LPF)	28
2.5.6.4	High pass Filters (HPF)	30
CHAPTER THREE		
DESIGN AND INVESTIGATION OF BANDSTOP FILERS USING U-SHAPED SLOTS		
3.1	Introduction	32
3.2	The Band-Stop Filter Using U-Shaped Slot.	32
3.3	Improving the Band Rejection Properties by Using Two Slots	36
3.4	Explanation of the Bandstop Behavior of the Filters	44
3.5	The Effective Permittivity and Permeability of the U-slot	46
3.6	The Design with Thicker Substrate	48
3.7	The Effect of The Loss Tangent of The Substrate	49
3.8	The Electric Field Distribution on the Slot	52
3.9	The Radiated Field from the Slots	55
3.10	Experimental Assessment of the Proposed Filters	60
3.11	Comparison with Other Designs	64
CHAPTER FOUR		
APPLICATION OF THE U-SHAPED GEOMETRY INTO FREQUENCY SELECTIVE SURFACES FSS		
4.1	Introduction	66

Subject		Page
4.2	U-shaped Conducting Strips on A Dielectric Sheet	66
4.2.1	E-field is Parallel to the U-Strip ($E \parallel U$)	67
4.2.2	E-field is Perpendicular to the U-Strip ($E \perp U$)	73
4.3	U-slots in a Conducting Sheet	77
4.3.1	E-field is Perpendicular to the U-Slot ($E \perp U$).	78
4.3.2	E-field is Parallel to the U-Slot ($E \parallel U$).	83
CHAPTER FIVE		
CONCLUSIONS AND FUTURE WORK		
5.1	Conclusions	87
5.2	Future Work	90
REFERENCES		
References		91

LIST OF FIGURES

Figure	Title	Page
CHAPTER TWO		
2.1	(a) conventional materials: ϵ , μ are obtained from atoms that composed. (b) in metamaterials: μ_{eff} , ϵ_{eff} are obtained from the sub-units which contain a huge number of atoms.	11
2.2	Materials classification depends on their permittivity ϵ and permeability μ values	13
2.3	First metamaterial structures proposed by Pendry. (a) TW (Thin Wire) structure is working as ENG metamaterial. (b) SRR (Split-Ring Resonator) structure is constituting an MNG metamaterial.	14
2.4	LH structures are combining TWs and SRRs. (a) LH unidimensional structure. (b) LH bidimensional structure	15
2.5	Two configurations of the SRR, metal parts are represented in grey; (a) The SRR with equivalent circuit model. (b) The CSRR with equivalent circuit model.	16
2.6	Various configurations of the SRR and equivalent models; (a) NB-SRR. (b) D-SRR. (c) SR. (d) DSR. (e) Broadside coupled split-ring resonator (BC-SRR). (f) OSRR	17
2.7	The equivalent circuit models of metamaterial transmission lines; (a) right-handed (b) left-handed	21
2.8	The equivalent circuit of the composite right-hand/left-hand metamaterial transmission line	21
2.9	Radio Cloaking. (a) Two-dimensional microwave cloaking structure. (b) State of transmission of electromagnetic waves.	22
2.10	A practical example of the beam scanning of a radar antenna.	24
2.11	Backward Coupler.	24
2.12	(a) The basic cell of the left-hand (LH) metamaterial microstrip line. (b) equivalent circuit model.	26
2.13	(a) The symmetric split ring resonator (SSRR). (b) Fabricated Metamaterial substrate using combined SSRR's dielectric strips.	28
2.14	The stopband filter was employing periodic loading of CSSR's in the ground plane; (a) 3 CSSR's, (b) 7 CSSR's.	28
2.15	The topology of embedded hex-omega structures underneath LPF in the ground plane.	29

Figure	Title	Page
2.16	Distributed Bessel LPF design; (a) without CSRR, (b) with CSRR.	29
2.17	An array of V structures placed underneath the loaded LPF.	30
2.18	The HPF; (a) basic cell design, (b) equivalent (T-circuit) model.	30
2.19	The layout of the filter formed by three CSRR cells.	31
CHAPTER THREE		
3.1	The geometry of the proposed band-stop filter using a U-shaped slot etched on a microstrip line.	33
3.2	Transfer characteristics of the U-slot filter; ($l = 18.2\text{mm}$, $c = 0.5\text{mm}$, and $d = 1.0\text{mm}$).	34
3.3	Transfer characteristics of the U-slot filter for various slot lengths (l), ($c = 0.5\text{mm}$, $d = 1.0\text{mm}$).	35
3.4	Transfer characteristics of the U-slot filter for various slot widths (c); ($l = 18.2\text{mm}$, $d = 1.0\text{mm}$).	35
3.5	Geometry of the filter with the U-slot positioned at distance (a) from the end of the microstrip line.	35
3.6	Transfer characteristics of the U-slot filter for various locations of the slot (a) ($l = 18.2\text{mm}$, $d = 1.0\text{mm}$, $c = 0.5\text{mm}$).	36
3.7	Geometry of the filter with two vis-a-vis U-slot's spaced by t ; $l = 18.2\text{mm}$, $d = 1.0\text{mm}$, and $c = 0.5\text{mm}$	36
3.8	Transfer characteristics of the filter with two vis-à-vis U-slot's for ($l = 18.2\text{mm}$, $d = 1.0\text{mm}$, $c = 0.5\text{mm}$).	37
3.9	Transfer characteristics of the filter for various slot width c of two vis-à-vis U-slot's for ($l = 18.2\text{mm}$, $d = 1\text{mm}$, $t = 1\text{mm}$).	37
3.10	Transfer characteristics of the filter two vis-à-vis U-slot with various separation d ; ($c = 0.5\text{mm}$, $t = 1\text{mm}$).	37
3.11	Geometry of the filter with two back-to-back U-slot's with separation of w ; ($l = 18.2\text{mm}$, $d = 1.0\text{mm}$, $c = 0.5\text{mm}$).	38
3.12	Transfer characteristics of the filter with two back-to-back U-slot's for various separation w at ($l = 18.2\text{mm}$, $d = 1.0\text{mm}$, $c = 0.5\text{mm}$).	38
3.13	Transfer characteristics of the filter for various slot width c of two back-to-back U-slot for ($l = 18.2\text{mm}$, $d = 1\text{mm}$, $w = 1\text{mm}$).	39
3.14	Transfer characteristics of the filter for various distances between two slots d and slot lengths l of two back-to-back U-slot for ($c = 0.5\text{mm}$, $w = 1\text{mm}$).	39

Figure	Title	Page
3.15	Geometry of the filter with two interlaced U-slots with separation h ; ($l=18.3\text{mm}$, $d=1.2\text{mm}$, $c=0.4\text{mm}$).	40
3.16	Transfer characteristics of the filter with two interlaced U-slots for various separation h ($l=18.3\text{ mm}$, $d=1.2\text{mm}$, $c=0.4\text{mm}$).	40
3.17	Transfer characteristics of the filter with two interlaced U-slots with various separations h ($l=18.3\text{mm}$, $d=1.2\text{mm}$, $c=0.4\text{mm}$).	41
3.18	Transfer characteristics of the filter with two interlaced U-slots for various separation h ($l=18.3\text{mm}$, $d=1.2\text{mm}$, $c=0.4\text{mm}$).	41
3.19	Transfer characteristics of the filter with two interlaced U-slot's for various slot widths c for ($l=18.3\text{mm}$, $d=1.2\text{mm}$).	42
3.20	Transfer characteristics of the filter with two interlaced U-slot's for various distances between two slots d ($c=0.4\text{mm}$).	42
3.21	Comparison of the filter reflection coefficient S_{11} for a single slot, 2-slots face-face, 2-slots back-back, and interlaced slots.	43
3.22	Comparison of the filter transmission coefficient S_{21} plots for a single slot, 2-slots face-face, 2-slots back-back, and interlaced slots.	43
3.23	An equivalent circuit representation of the U-slot filter.	46
3.24	Extracted real and imaginary parts of the effective parameter of the single U slot ($l=18.2\text{ mm}$, $d=1.0\text{ mm}$, $c=0.5\text{mm}$). The solid line represents the real part, while the dashed line represents the imaginary part.	46
3.25	Extracted effective electric permittivity and magnetic permeability of two back-to-back U-slots ($l=18.2\text{ mm}$, $d=1.0\text{ mm}$, $c=0.5\text{mm}$, $w=1\text{mm}$). The solid line represents the real part, while the dashed line represents the imaginary part.	47
3.26	Extracted effective electric permittivity and magnetic permeability of two face-face U-slots ($l=18.2\text{ mm}$, $d=1.0\text{ mm}$, $c=0.5\text{mm}$, $t=1\text{mm}$). The solid line represents the real part, while the dashed line represents the imaginary part.	47
3.27	Extracted real and imaginary parts of the effective parameter of interlaced U slots ($l=18.3\text{mm}$, $d=1.2\text{mm}$, $c=0.4\text{mm}$, $h=1\text{mm}$). The solid line represents the real part, while the dashed line represents the imaginary part.	47

Figure	Title	Page
3.28	Transfer characteristics of resized U-slot filter ($l=17.45\text{mm}$, $d=2.5\text{ mm}$, $c=0.7\text{mm}$).	48
3.29	Transfer characteristics of resized filter with two back-to-back U-slot's ($l=17.45\text{mm}$, $c=0.7\text{mm}$, $d=2.5\text{ mm}$ and separation between two slots 1mm).	48
3.30	Transfer characteristics of resized filter with two vis-à-vis U-slot's ($l=17.45\text{mm}$, $c=0.7\text{mm}$, $d=2.5\text{ mm}$ and separation between two slot's 1mm).	49
3.31	Transfer characteristics of resized filter with two interlaced U-slot's ($l=17.85\text{mm}$, $c=0.6\text{mm}$, $d=2.55\text{mm}$ and separation between two slot's 2mm).	49
3.32	Transfer characteristics of the U-slot filter for tangent loss equal to 0.0025 ; ($l=18.2\text{mm}$, $c=0.5\text{mm}$, $d=1.0\text{mm}$).	50
3.33	Transfer characteristics of filter with two back to back U-slot's for tangent loss equal to 0.0025 ; ($l=18.2\text{mm}$, $d=1.0\text{mm}$, $c=0.5\text{mm}$, $w=1\text{mm}$).	50
3.34	Transfer characteristics of filter with two vis-à-vis U-slot's for tangent loss equal to 0.0025 ; ($l=18.2\text{mm}$, $d=1.0\text{mm}$, $c=0.5\text{mm}$, $t=1\text{mm}$).	50
3.35	Transfer characteristics of filter with two interlaced U-slots for tangent loss equal to 0.0025 ($l=18.3\text{ mm}$, $d=1.2\text{mm}$, $c=0.4\text{mm}$, $h=1\text{mm}$).	51
3.36	Simulated E-field distribution inside the single slot. (a) at 2.5GHz . (b) at 4GHz .	52
3.37	Simulated E-field distribution inside the two slots facing each-other. (a) at 2.5GHz . (b) at 4GHz .	53
3.38	Simulated E-field distribution in the back-to-back U-slots. (a) at 2.5GHz . (b) at 4GHz .	54
3.39	Simulated E-field distribution inside the two interlaced U-slots. (a) at 2.5GHz . (b) at 4GHz .	54
3.40	Radiation pattern of the microstrip line without any slot at; (a) 2.45 GHz , and (b) at 4 GHz frequency.	56
3.41	Radiation pattern of the filter with the U-slot at; (a) 2.45 GHz , and (b) at 4 GHz frequency. ; ($l=18.2\text{mm}$, $d=1.0\text{mm}$, $c=0.5\text{mm}$).	56
3.42	Radiation pattern of the filter with the two back-back slots at; (a) 2.45 GHz , and (b) at 4 GHz frequency. ($l=18.2\text{mm}$, $d=1.0\text{mm}$, $c=0.5\text{mm}$, $w=1\text{mm}$).	57

Figure	Title	Page
3.43	Radiation pattern of the microstrip line with the two face-face slots at (a) 2.45 GHz, and (b) at 4 GHz frequency. ;($l = 18.2\text{mm}$, $d = 1.0\text{mm}$, $c = 0.5\text{mm}$, $t = 1\text{mm}$).	58
3.44	Radiation pattern of the filter with the two interlaced slots at (a) 2.45 GHz, and (b) at 4 GHz frequency. ($l = 18.3\text{ mm}$, $d = 1.2\text{mm}$, $c = 0.4\text{mm}$, $h = 1\text{mm}$).	59
3.45	Photographs of the fabricated prototypes; (a) the filter with the interlaced U-slots, (b) the transmission line, and (c) the filter with a single U-slot.	60
3.46	Comparative results between simulation and measurement S-parameters of the fabricated microstrip line with no slot.	61
3.47	Comparative results between simulation and measurement S-parameters of the fabricated U-slot filter; ($l = 18.2\text{mm}$, $c = 0.5\text{mm}$, $d = 1.0\text{mm}$).	62
3.48	Comparative results between simulation and measurement S-parameters of the fabricated filter with interlaced U-slot; ($h = 1\text{mm}$, $l = 18.3\text{ mm}$, $d = 1.2\text{mm}$, $c = 0.4\text{mm}$).	62
3.49	Comparison of measured S11 plots for no slot, single slot, and interlaced slots filters.	63
3.50	Comparison of measured S21 plots for no slot, single slot, and interlaced slots filters.	63
Chapter Four		
4.1	The geometry of the proposed FSS structure with the U-shaped strips.	67
4.2	Simulation setup for the unit cell in CST. The E-field of the incident wave is along the Y-axis ($E \parallel$ to the strip legs).	67
4.3	Transfer characteristics of the U-shaped strip when the E-field is Y-directed ($c = 1\text{mm}$, $l = 30.5\text{mm}$, and d is 10mm).	68
4.4	Transfer characteristics of the U-shaped FSS structure for various total length ($d = 10\text{mm}$, $c = 1\text{mm}$).	68
4.5	Transfer characteristics of U-shaped FSS structure for various line width c ($l = 30.5\text{mm}$ and $d = 10\text{mm}$).	69
4.6	Transfer characteristics of U-shaped FSS structure for various center part lengths d ($l = 30.5\text{mm}$ and $c = 10\text{mm}$).	70
4.7	Extracted effective permittivity and permeability of the U-shaped ($l = 30.5\text{mm}$, $c = 1\text{mm}$, and $d = 10\text{mm}$). (b) Zoom figure of the extracted effective permittivity. The solid line represents the real part, while the dashed line represents the imaginary part.	70

Figure	Title	Page
4.8	Simulated E-field distribution around the U-shaped strip. The E-field of the incident wave is along the Y-axis ($E \parallel$ to the strip legs).	72
4.9	Simulated current distribution on the U-shaped strip. The E-field of the incident wave is along the Y-axis ($E \parallel$ to the strip legs).	72
4.10	Radiation pattern of the U-shaped strip (a) 3.5Ghz, and (b)5GHz. The E-field of the incident wave is along the Y-axis ($E \parallel$ to the strip legs).	73
4.11	Simulation setup for the unit cell in CST. The E-field of the incident wave is along the X-axis, ($E \perp$ to the strip legs).	74
4.12	Transfer characteristics of U-shaped strip when the E-field is X-directed ($l = 30.5\text{mm}$, $c = 1\text{mm}$, and $d = 10\text{mm}$).	74
4.13	Transfer characteristics of the U-shaped strip when the E-field is X-directed ($l = 13\text{mm}$, $c = 1\text{mm}$, and $d = 6\text{mm}$).	75
4.14	Extracted effective electric permittivity and magnetic permeability of U-shaped ($c = 1\text{mm}$, $l = 13\text{mm}$, and $d = 6\text{mm}$).	75
4.15	Simulated E-field distribution inside the U-shaped strip. (a) at 3.5GHz. (b) At 5GHz. The E-field of the incident wave is along the X-axis, ($E \perp$ to the slot legs).	77
4.16	Simulated surface-current distribution around the U-shaped strip. (a) at 3.5GHz. (b) At 5GHz. The E-field of the incident wave is along the X-axis, ($E \perp$ to the slot legs).	77
4.17	The geometry of the proposed U-slots FSS structure.	78
4.18	Simulation setup for the unit cell in CST. The E-field of the incident wave is along the X-axis, ($E \perp$ to the slot legs).	79
4.19	Transfer characteristics of the U-slot when the E-field is X-directed ($c = 1\text{mm}$, $l = 29\text{mm}$, and $d = 10\text{mm}$).	79
4.20	Transfer characteristics of the U-slot FSS structure for various total length ($d = 10\text{mm}$, $c = 1\text{mm}$).	80
4.21	Transfer characteristics of the U-slot FSS structure for various slot widths c ($l = 29\text{mm}$ and $d = 10\text{mm}$).	81
4.22	Transfer characteristics of the U-slot FSS structure for various center part lengths d ($l = 29\text{mm}$ and $c = 1\text{mm}$).	81
4.23	Extracted effective permittivity and permeability of the U-Slot ($c = 1\text{mm}$, $l = 29\text{mm}$, and d is 10mm). The solid line represents the real parts, while the dashed line represents the imaginary parts.	81

Figure	Title	Page
4.24	Simulated E-field distribution inside the U-slot. (a) at 3.5GHz. (b) at 5GHz. The E-field of the incident wave is along the X-axis, ($E \perp$ to the slot legs).	82
4.25	Radiation patterns of the U-slot; (a) at 3.5GHz, (b) at 5GHz. The E-field of the incident wave is along the X-axis, ($E \perp$ to the slot legs).	83
4.26	Simulation setup for the unit cell in CST. The E-field of the incident wave is along the Y-axis ($E //$ to the slot legs).	83
4.27	Transfer characteristics of the U-shaped slot when the E-field is Y-directed ($l = 29\text{mm}$, $c = 1\text{mm}$, and $d = 10\text{mm}$).	84
4.28	Transfer characteristics of the U-shaped strip when the E-field is Y-directed ($l = 13\text{mm}$, $c = 1\text{mm}$, and $d = 6\text{mm}$).	84
4.29	Extracted effective permittivity and permeability of U-Slot ($l = 13\text{mm}$, $c = 1\text{mm}$, and $d = 6\text{mm}$). The solid line represents the real part, while the dashed line represents the imaginary part.	85
4.30	Simulated E-field distribution inside the U-slot. (a) at 3.5GHz. (b) at 5GHz. The E-field of the incident wave is along the Y-axis ($E //$ to the slot legs).	86

LIST OF TABLES

Table	Title	Page
CHAPTER THREE		
3.1	Frequency response characteristics of different designs of the filter with various configurations of the U-shaped slot.	57
3.2	Comparison of the S11 and S21 parameters for the two substrates	58
3.3	Radiation pattern characteristics for the four filter designs compared to that of the microstrip line.	60
3.4	Comparison of the characteristics of the proposed filters with other published designs.	60

LIST OF ABBREVIATIONS

Abbreviation	Name
BC-SRR	Broadside Coupled Split-Ring Resonator
BPF	Band Pass Filter
BSF	Band Stop Filter
CPW	Coplanar Waveguide
CRLH	Composite Right/Left-Handed Material
CSRR	Complementary Split-Ring Resonator
DNG	Double Negative Metamaterial
DPS	Double Positive Material
DSR	Double Spiral Resonator
D-SRR	Double-Split Resonator
e.m.	Electromagnetic Wave
EBG	Electromagnetic Band-Gap Material
ENG	Epsilon- Negative
FSS	Frequency Selective Surface
HPF	High Pass Filter
LH	Left-Handed
LHM	Left-Handed Material
LPF	Low Pass Filter
MIMO	Multiple Input Multiple Output
MNG	Mu-Negative Material
M-NURR	M-Band Nested U-Ring Resonator
NB-SRR	Non-Bianisotropic Split Ring Resonator
NIM	Negative Index Metamaterial
OLR	Open Loop Resonator
OSRR	Open Split-Ring Resonator
RH	Right-Handed
SCSRR	Semi-Complementary Split Ring Resonator
SIR	Stepped-Impedance Resonator
SNG	Single- Negative Material
SR	Single-Spiral Resonant
SRR	Split Ring Resonator

LIST OF SYMBOLS

Symbol	Name
a	Slot distance from the end of the microstrip line
c	Slot width
d	Separation between the U-slot legs
d_{eff}	Metamaterial slap thickness
f_0	Resonance frequency
h	Interlaced U-slots distance separation
h_s	Substrate height
k_0	Wave number
l	Slot leg length
n_{eff}	Effective refractive index
S_{11}	Reflection coefficient
S_{21}	Transmission coefficient
t	Face-to-face U-slot's separation
u	Back-to-back U-slot's separation
w	Microstrip Line width
Z	Impedance
Z_{eff}	Effective impedance
Z_0	Impedance of the microstrip line without the slot
Γ	Reflection coefficient
δ	Loss tangent
ϵ	Permittivity
ϵ_{eff}	Effective permittivity
ϵ_r	Relative dielectric constant
λ_0	Wavelength in air
λ	Wavelength
λ_e	Effective wavelength
λ_g	Guided wavelength
μ	Permeability
μ_{eff}	Effective permeability

CHAPTER ONE

INTRODUCTION

CHAPTER ONE

INTRODUCTION

1.1 Preface

The physical characteristics of material play a significant role in its interaction with the electric and magnetic field components of the electromagnetic (e.m.) waves. When the material structure is considerably smaller than the wavelength λ , its interaction with the e.m. wave is constant, and it is called "Constitutive Parameters". The two important parameters that describe the properties are permittivity ϵ which is related to the electric field E and permeability which is associated with the magnetic field H . In complex materials, these parameters may rely on the wave direction which can be described by anisotropic materials [1]. Natural materials have positive real parts of constitutive parameters, except a class of materials named plasma whose effective permittivity has negative values when the frequency is lower than the plasma frequency. In this case, the wave number k_0 turns into imaginary, and the propagating electric field is evanescent [2]. The possibility of having a simple media with a negative permeability and a negative permittivity at some frequency, such that the e.m. wave propagates with a real wave number k_0 , was studied in 1967 by Victor Veselago [3].

Metamaterials are artificial materials designed to offer properties that are not available in nature. They usually gain their characteristics from structures instead of compositions, as they use the inclusion of small inhomogeneities in the material to exhibit effective macroscopic behavior. The word "meta" refers to the resulting effective properties whose e.m. responses are "beyond" those of their constituent materials [4].

Traditional materials have their properties caused by the individual atoms and molecules composing these materials. The macroscopic e.m. fields are

averaged across the spatially varying local fields. Such averages are very well defined as there are billions of molecules contained in a cube of a material whose size is larger than one wavelength. In metamaterials, this concept is extended to a much larger scale where the molecules are replaced with man-made structures. These structures usually have dimensions of nanometers for visible light applications or few millimeters at the GHz frequencies, but they are still much less than the wavelength. In this way, the properties are engineered through “structure” rather than through “chemical textures”[5].

Metamaterials have been used in the field of electromagnetics in a very range of applications such as Frequency Selective Surfaces FSS, polarization conversion, gain enhancement of antenna, filtering, isolation, cloaking of e.m. waves, and more. In particular, the e.m. waves in a composite media interact with the inclusions that produce electric and magnetic polarizations. This, in turn, affects the macroscopic effective permeability and permittivity of the bulk composite medium. Since metamaterials are synthesized by embedding artificial inclusions inside the hosting medium, then the designer is offered an extensive collection of independent parameters such as size, shape, and the compositions of the inclusions as well as the properties of host materials. All these design parameters have a significant role in the resulting properties of the composed material [6].

1.2 Literature Review

The metamaterials history started in 1967 when the theoretical concept was put by Viktor Veselago [3]. He notes that a plane-wave propagation in a material whose permittivity and permeability are negative at specific operating frequency leads to a very uncommon e.m. phenomenon, such as negative refractive index, the opposite signs of Poynting vector, the wave vector of propagating e.m. waves and that the Cherenkov radiation cone in the direction of backwards rather than forwards. In 1996, Pendry proposed a negative

permittivity structure as an array of metallic wires arranged like a mesh. This structure produces a negative effective permittivity at microwave frequencies and positive permeability with relatively small losses, and the structure is called “epsilon- negative (ENG)” [7]. In 1999, he demonstrated that a split ring resonator (SRR) structure (that have 'C' shape) with an axis along the direction of the propagating wave could provide a positive permittivity and a negative permeability called mu-negative (MNG) materials [8]. Pendry also showed that periodic structures whose unit cells had a size p much smaller than the guided wavelength ($p \ll \lambda_g$) of both of wires and that a split ring resonator could lead to a negative refractive index. In 2000, he put the concept of the superlenses, materials with negative refractive index, which were able to recreate perfect 2D images of an object for both the propagating waves and evanescent waves [9]. Pendry's theories have inspired the realization of the first left-handed structure.

Following up the work of Pendry, Smith created a material with negative refractive index [10]–[13]. They demonstrated the first left-handed material by using theories provided by Veselago and Pendry. To composite new structure, two structures of an array of conducting thin wires and another array of split ring resonator are combined to achieve simultaneously negative values of effective permeability μ and permittivity ϵ that exhibit at a specific resonant band in the microwave frequencies. It is predicted that such phenomena as the Doppler effect, Cherenkov radiation, and even Snell's law were inverted [10].

In 2001, Smith and Shelby experimentally verified the phenomenon of a negative refractive index by using material constructed from periodic structures of two square split rings (each ring opening on the opposite side) and parallel rod to the plane of the rings. The structure produces negative permeability when the incident magnetic field frequency is near to the resonant

frequency of the split rings, otherwise the incident electric field parallel to the rods produces negative permittivity over a narrow frequency band [11].

In 2004, Falcone et al. proposed a new design of metasurfaces having a high-frequency selectivity and planar metamaterials with a negative dielectric permittivity using complementary counterpart of the SRR. The complementary split-ring resonator where the rings forming the resonator are slots etched on a metallic surface. This is inspired by the idea of the Babinet principle to the SRR [14].

In 2004, Chen et al. proposed a new two oppositely placed S-shaped SRRs metamaterial, which provided negative permittivity and negative permeability response without using a rod in the design. Left-handed behavior happens for a wide frequency band with very low losses [15].

In 2005, Ran et al. studied experimentally several types of metamaterials which exhibited LH properties over a wide frequency band. The samples were constructed by Ω -like metallic patterns and S-shaped resonators [16].

In 2005, García-García et al. fabricated efficient stopband structures using split-ring resonators (SRRs), which were magnetically coupled to microstrip lines depending on the idea of single negative permeability material. These structures offer a high frequency-selectivity for the small number of SRR stages, which lead to a compact size for the planar device. By increasing the SSR stages, narrow passband filters with symmetric and high-frequency responses are obtained[17][18].

In 2006, Wu et al. studied the transmission characteristic of the split-ring resonator defected ground structure to enhance the out-band suppression[19]. In the same year, Zhou et al. introduced the structure of periodic arrays of pairs of H-shaped metallic wires to build negative-index materials[20].

In 2007, Pan et al. designed a novel compact of left-handed transmission line (LH-TL) metamaterial which was improved by periodic split rings etched on the microstrip line without vias or virtual ground to provide a wide band-pass filter [21]. In the same year, Gil et al. designed a broadband high pass filter by making a balance between composite right/left-handed (CRLH) transmission lines and complementary split rings resonators (CSRRs). The filter has small dimensions and achieved a good performance [22].

In 2007, Ekmekçi et al. demonstrated a “V-Shaped” metamaterial over both faces of the substrate. This structure exhibits double-negative characteristics at only 8.10 GHz [23].

In 2008, Kshetrimayum et al. designed stop band filters by etching an array of complementary split ring resonators (CSRRs) in the microstrip line ground plane which enhanced the performance of the stop-band filter and offered an overall size miniaturization [24]. In 2009, Amiri et al. presented a novel spiral-S-shaped resonator with two wires on the side of the substrate unit cell. This structure exhibits very low losses and metamaterial double negative behavior [25]. In the same year, Fallahzadeh and Tayarani proposed a novel microstrip filter by etching a square split ring on the microstrip line which achieved compact size and high rejection level bandstop filter [26].

In 2009, Qi et al. proposed a novel metamaterial microstrip cross-coupled resonator bandpass filter which verified the double negative characteristics with good passband property. It has been shown to have a high rejection with small dimension and low insertion loss [27].

In 2010, Ya-nan and Ling-ling proposed metamaterial transmission lines that were consisted of two SRRs placed closely at both sides of the central conductor strip and one CSRR was etched on the ground plane below the central conducting strip to achieve a backward-wave propagation at resonance frequencies [28].

In 2011, Lu and et al. proposed a cascaded uniplanar double spiral resonant cells (UDSRCs) which achieved enhanced rejection level, wide bandstop, and compact size [29]. In the same year, Naghshvarian-Jahromi and Tayarani proposed a bandstop filter using a defected ground pane. The notch frequency is obtained by the array of two semi-complementary split ring resonators (SCSRRs), that are etched in the ground plane as well as two line resonators etched out of the microstrip line [30]. In 2011, Sahu et al. introduced a complimentary hexagonal-omega metamaterial unit cell with negative μ and ϵ property and used it in the ground plane of microstrip line which achieved compact, low pass filter with low insertion loss and sharp cut-off [31].

In 2012, Ouda and Abutahoun proposed a new infinity-shaped split ring resonator planner metamaterial unit cell. It is composed of two identical infinity-shaped copper parallel patterns etched on both sides of the dielectric substrate. That design achieves wider bandwidth, around 11.35 GHz, and negative refractive index [32]. In the same year, Turkmen et al. proposed a novel metamaterial topology of M-band nested U-ring resonator (M-NURR), for multiple band resonators and compact in size unit cell. Wider negative effective permeability bandwidths were achieved using three nested U-ring [33].

In 2013, Raad et al. proposed a novel μ -Negative MNG unit cell based on two SRRs connected at the center by the bridging technique to enhance the bandwidth rejection [34]. Mallik in the same year proposed a two rectangular U-shaped metamaterial to construct four different configurations which achieved simultaneously negative permeability & permittivity. Left-handed attributes were displayed at approximately 5, 6, and 11 GHz for different configurations [35].

In 2014, Slam, et al. presented a design of a novel two split-H-shaped structure connected to each other by a metal link to construct a metamaterial unit cell which achieved negative permeability and permittivity in a multiband frequency range [36]. In the same year, Nesimoglu and Sabah presented a new way to check the metamaterial characteristic by using the S shape unit cell by exciting it on the ground plane of the microstrip transmission line to verify the existence of metamaterial properties [37].

In 2015, Bhaskar et al. proposed bandstop filters by etching periodic patterns of two types of hexagonal CSRR on the ground plane, which achieved high performances for rejection stopband and nearly flat passband [38].

In 2015, Hossain et al. proposed a new design of a wide-band double-negative metamaterial. The structure consists of two G-shaped SSR linked by a metal line which achieved negative permittivity and permeability for the two bands [39].

In 2016, Hasan et al. proposed a compact modified Z-shaped double negative metamaterial for wideband applications, which exhibited a wider bandwidth in the DNG region [40]. In 2016, Krishna et al. proposed band stop metamaterial using split ring resonator (SRR) and Open Loop Resonator (OLR) using microstrip line [41].

In 2017, Ali et al. proposed a novel planar rectangular CSRR design for dual passband characteristics at 2.95 and 5.23 GHz that achieved negative magnetic permeability [42]. In the same year, George et al. proposed a novel edge coupled triangular and pentagonal Open Loop Resonators OLR to realize a metamaterial unit cell [43].

In 2018, Smith and Adams introduced a three-dimensional spherical spiral metamaterial unit cell that achieves negative permeability, negative permittivity over much bandwidth than normal ring resonators [44].

In 2018, Choudhary's proposed a compact coplanar waveguide (CPW) dual bandpass load by modifying a complementary split ring resonator (CSRR) structure on the ground plane which provided compactness and flexibility design with a multiband bandpass filter with controllable transmission zero [45]. In the same year, Alam et al. proposed a compact and joint two split P-shaped metal ink connected metamaterial unit cell that is successful for dual-band frequency showing negative effective permeability and permittivity for different band frequency [46].

In 2018, Marathe and Kulat designed a new compact dual-resonant and triple-resonant microwave metamaterials evolved by a combination of individual Z-shaped and S-shaped like geometries which achieved compactness in size with enhanced electric coupling and negative permittivity property at the resonant frequencies [47]. In the same year, Danaeian et al. proposed three compact metamaterial unit-cells depending on the idea of the stepped-impedance resonator (SIR) technique to reduce the size of CSRRs. The unit-cells consist of two modified rings to obtain SIR-CSSRs which are etched on the surface of the waveguide to obtain a forward passband with a high quality-factor, low insertion loss, and compact size [48].

The above survey shows that patches and/or slots in various shapes have been used to achieve the metamaterial behavior. The used shapes have been split ring, square ring, S-shape, Ω -like patterns, H-shape, V-Shape, spiral-S-shape, nested U-ring, split-H-shape, Z-shape, and many other shapes.

1.3 Aims of The Dissertation

1. Study the various types and important features of metamaterials.
2. Study the various applications of metamaterials in the field of microwaves, and antennas.

3. Focus on the design and analysis of passive microwave devices, such as filter and Frequency Selective Surfaces FSS based on the metamaterial principle.
4. Design and investigate the metamaterial properties exhibited by the U-shaped slot and U-shaped strip.
5. Utilize the U-shaped slot in the design of filters and FSS structures.

1.4 Thesis Layout

This thesis is divided into five chapters. Chapter one gives an introduction and literature review. Chapter two explores the background and the theory of metamaterial phenomena and its applications. Chapter three gives design details of a U-shaped utilization in a compact band reject filter. The experimental results are also shown in this chapter. Chapter four explores the use of the U-shaped slot and U-shaped strips into FSS applications. Chapter five gives the conclusions and some suggestions for future work.

CHAPTER TWO

BASICS OF

METAMATERIALS AND THEIR

APPLICATIONS

CHAPTER TWO

BASICS OF METAMATERIALS AND THEIR APPLICATIONS

2.1 Introduction

Metamaterials are artificial materials that are designed to offer some characteristics, which “may not be readily available in nature.” The properties of the metamaterials are attributed to the structures rather than compositions of the ingredients. They include small inhomogeneity to exhibit effective macroscopic behavior. The word “meta” refers to the resulting effective properties whose electromagnetic (e.m.) responses are “beyond” those of their constituent materials [4]. The metamaterials were invented in the ends of 1960s when Veselago first studied the electrodynamics of materials, which possessed dielectric permittivity ϵ and magnetic permeability μ of negative values at the same time. Veselago studied the propagation of plane waves in materials whose permittivity and permeability were assumed simultaneously negative. He suggested many properties of these materials that could be obtained at specific frequencies such as inverse refraction, negative radiation pressure, and inverse doppler effect [3].

2.2 Properties of Metamaterials

The properties of conventional materials originate from the different atoms and molecules of which they are composed. The e.m. fields inside the material are the fluctuating averages inside the local fields. These averages are typically a huge amount of molecules that is contained inside one cubic wavelength of the material. The concept of metamaterials extends this view to a larger scale by replacing the containing material with human-made structures

which are called inclusions. The dimensions of these structures made in nanometers for visible light usage meanwhile these dimensions are increased to few millimeters in microwave frequencies, which are smaller than a wavelength. Hence, metamaterial properties are designed from the structures, not through constituent atoms. Fig. 2.1 shows this notion [5].

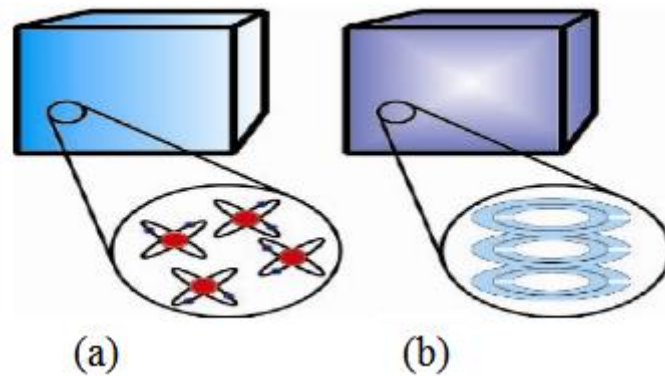


Fig. 2.1. (a) conventional materials: ϵ , μ are obtained from atoms that are composed. (b) in metamaterials: μ_{eff} , ϵ_{eff} are obtained from the sub-units which contain a huge number of atoms [5].

Metamaterials having a negative permittivity and a negative permeability are commonly referred to as left-handed materials (LHM) [49]. These artificial materials imply that the included structures and the separations between them are much smaller than the wavelength. Consequently, such media is usually described by its macroscopic constitutive parameters. This is not the case with other artificial structures (e.g., Electromagnetic Band-Gap materials, EBG) in which the distance between the inclusions is within half a wavelength or more, and the main behavior is dominated by periodic concepts [50]. Metamaterials have been used in many electromagnetic applications. The important property of metamaterials is the unusual and desired features that they offer because of their particular design and structure. In certain composite media, the e.m. wave interacts with these structures which produce moments for electric and magnetic. These moments

have an effect on the effective permeability μ_{eff} and permittivity ϵ_{eff} of a composite medium slab. The metamaterials are usually fabricated by synthesized structures artificially into a particular host medium.

Therefore, they provide the researcher with a large number of structures collection of various parameters, such as hosting materials properties, shape, size, and embedded structures configurations. These parameters have a significant role in the resulting properties of the composed material [5].

The properties of the materials determine the response of a system to the electromagnetic field, which is described by defining the macroscopic parameters permeability μ and permittivity ϵ of these materials. Based on this idea, the classification of metamaterials can be graphically illustrated in Fig. 2.2 [51]. If permittivity ϵ and permeability μ have positive real parts, as shown in the first quadrant in Fig. 2.2, such as natural materials (e.g., dielectrics), the material will be defined as “double positive (DPS).” In contrast, when both permittivity ϵ and permeability are negative, as shown in the third quadrant in Fig. 2.2, the material will be defined as “double-negative (DNG).” This class of materials has only been demonstrated with artificial constructions. DNGs are also referred to as negative index metamaterials (NIM). Other names for DNGs are “left-handed media” and “backward-wave media.” With materials having only one negative parameter, as shown in quadrants two and four in Fig. 2.2, the material will be defined as “single-negative (SNG).” The negative permittivity ϵ in the second quadrant will be defined as “epsilon- negative (ENG).” Such as the plasma layers of the ionosphere at AM radio frequencies as well as plasmonic materials behavior at the optical range frequencies.

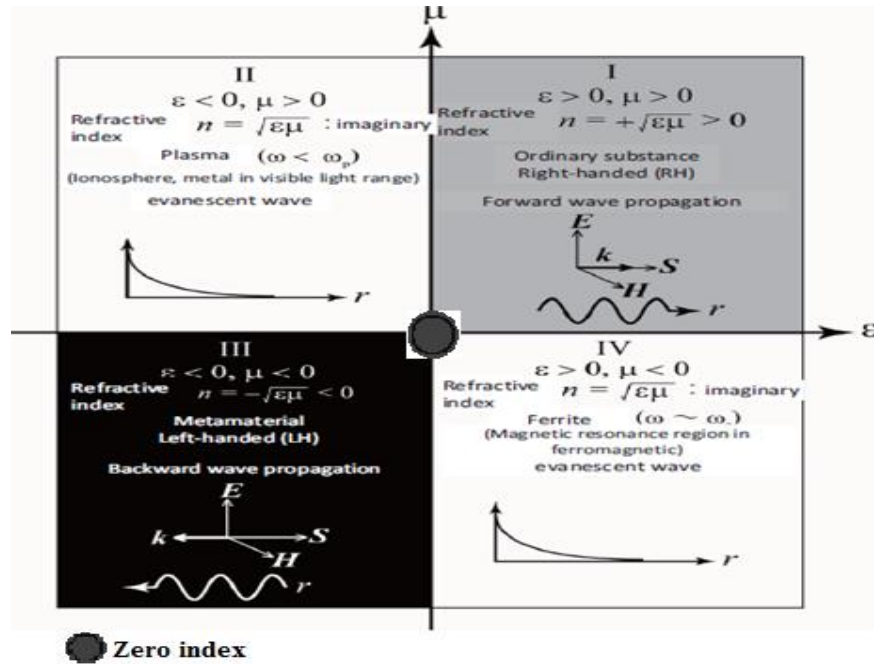


Fig. 2.2 Materials classification depends on their permittivity ϵ and permeability μ values [51].

If the permeability is negative, as, in the fourth quadrant, these materials will be defined “mu-negative (MNG).” Ferromagnetic materials exhibit such behavior in the VHF and UHF range of frequencies. Experiments have been conducted by adding two SNG layers to form a single metamaterial that effectively shows another form of DNG metamaterial [52]. Two slabs of ENG material and MNG material have been combined to demonstrate the process of wave reflection. This configuration gives properties such as anomalous tunneling, resonances, transparency, and zero reflection. If both permittivity ϵ and permeability μ are zero or near to zero, these materials will be defined as “zero indexes.” The process to realize the SNG materials may be relatively easier compared to that for the DNG materials. Therefore, many recent efforts are aiming to explore if the SNG media can be used to achieve some of the applications proposed initially for DNG media [4][50][51][53].

Veselago predicted in 1967, the existence of substances having negative values of permittivity ϵ and permeability μ at the same time [3]. Veselago used

the term "LH" substances to note that these materials would allow the propagation of e.m. waves with an LH triplet. He also predicted that the negative refractive index with respect to vacuum have opposite signs of propagating e.m. waves concerning the Poynting vector. Thus, the Doppler effect has an opposite sign concerning to that for the conventional materials.

2.3 Realization of Metamaterials

This section discusses the former efforts of researchers to realize metamaterial properties. Pendry introduced the ENG and MNG structures in the microwave range. Both metamaterials were periodic structures whose unit cells size p were much smaller than the guided wavelength ($p \ll \lambda_g$). Thus, these structures can be considered as homogeneous metamaterials. ENG structures are constructed from Thin-Wire cells (TW), as shown in Fig. 2.3.a. MNG metamaterial unit-cell is the Split-Ring Resonator (SRR), which is shown in Fig. 2.3.b [7][8].

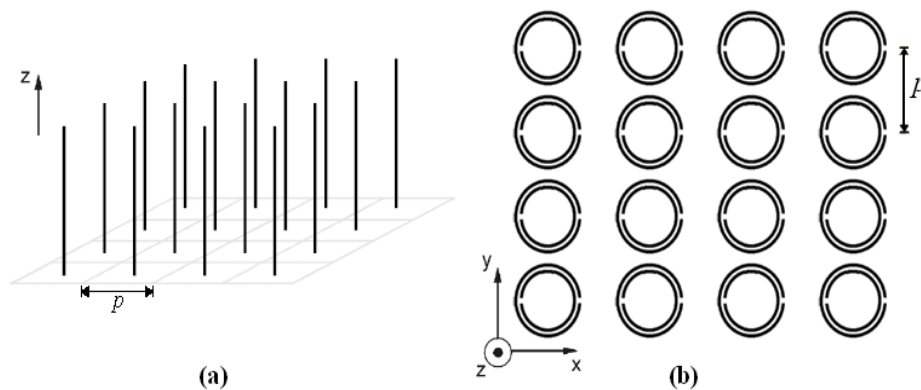


Fig. 2.3 First metamaterial structures proposed by Pendry. (a) TW (Thin Wire) structure is working as ENG metamaterial [7]. (b) SRR (Split-Ring Resonator) structure is constituting an MNG metamaterial [8].

Smith and et al. combines Pendry's structures to develop the first LH metamaterial implementation shown in Fig. 2.4 [10]. They considers a composite medium containing a periodic array of interspaced conducting nonmagnetic split ring resonators and continuous wires. This structure gives

simultaneously negative values of effective permeability μ and permittivity ϵ at microwave frequencies. In such phenomena, it is predicted that the Doppler Effect, Cherenkov radiation, and even Snell's law are inverted [10].

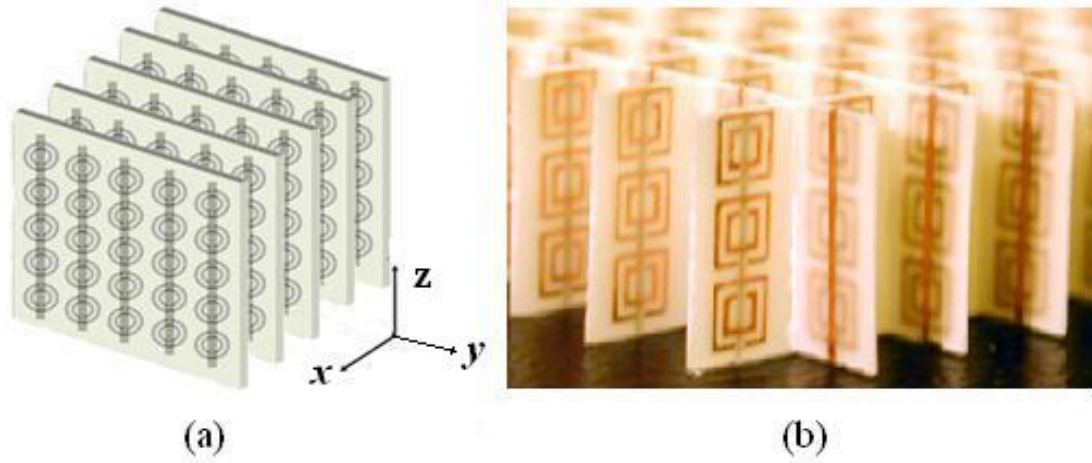


Fig. 2.4 LH structures combine TWs and SRRs. (a) LH unidimensional structure. (b) LH bidimensional structure [11].

The idea of the SRR is used to design various resonators of sub-wavelength sizes and similar configurations. One example is a complementary split-ring resonator (CSRR) which is a counterpart of the SRR, the (see Fig. 2.5). In this case, the resonating rings are circular slots on the metallic surface [14]. The SRR has the form of two open metallic concentric rings, as illustrated in Fig. 2.4.a. The currents in the rings are produced when the resonator is excited by a z-directed or axial magnetic field. The gaps in the rings work as capacitors to allow the induced AC to flow through the gaps as displacement current. The resonator can be modeled by the equivalent circuit depicted in Fig. 2.5.a [54].

In Fig 2.5, C_o is the total capacitance between the two rings. SRR resonance frequency is obtained by $f_o = (L_s C_s)^{-1/2} / 2\pi$, where C_s is the upper and lower halves split-ring resonator series capacitance, i.e. $C_s = C_o / 4$. The inductance value L_s is estimated from only one ring of an average radius r_o and width c [54][55].

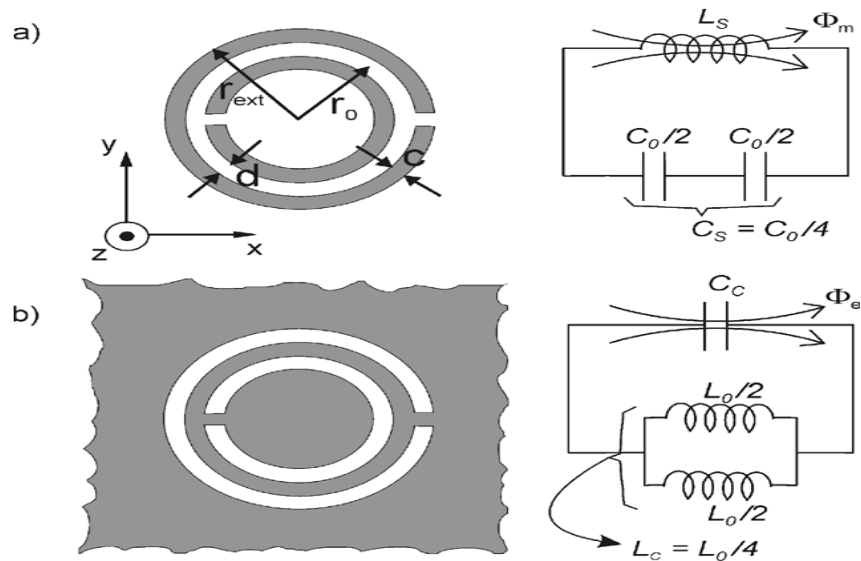


Fig. 2.5 Two configurations of the SRR, metal parts are represented in grey; (a) The SRR with equivalent circuit model. (b) The CSRR with equivalent circuit model [54].

When the Babinet principle is applied to the above complementary structures (see Fig. 2.5), the magnetic and electric fields, currents, interchange their roles. Therefore, both structures will be resonant at the same frequency. However, in contrast to the split-ring resonator, the complementary split-ring resonator CSRR shows negative permittivity values near its resonance, which feed by an average value of axial electric field [14].

Many other structures, based on the various configuration of the inclusions, such as multiple splits, different spiral, multi-layer topologies, resonators having different symmetries and smaller size have been proposed, and their performance investigated as shown in Fig. 2.6 [14][54][55].

The non-bianisotropic split ring resonator (NB-SRR) is a modified version of the basic split ring resonator (SRR) shape, which presents a rotation in the symmetry of 180° in the element plane. Consequently, the influence of cross-polarization in the NB-SRR is not suitable, although there is a similarity between the equivalent model and frequency response of the NB-SRR and

basic shape of SSR [54], [56]. The double-split SRR (D-SRR) also avoids the cross polarization due to its symmetry. However, according to the two equivalent circuits, the frequency of resonance of the D-SRR is doubled from the basic SRR (for the same size). The single-spiral resonant (SR) and the double spiral resonators (DSR) are used to reduce the frequency resonance with respect to basic SRR, which can be noted from the equivalent circuits model [54]. The open split-ring resonator (OSRR) also has a smaller electrical size (half that of the basic SRR) as the overall capacitance of the two halves has a parallel connection which is opposite in the SRR [56].

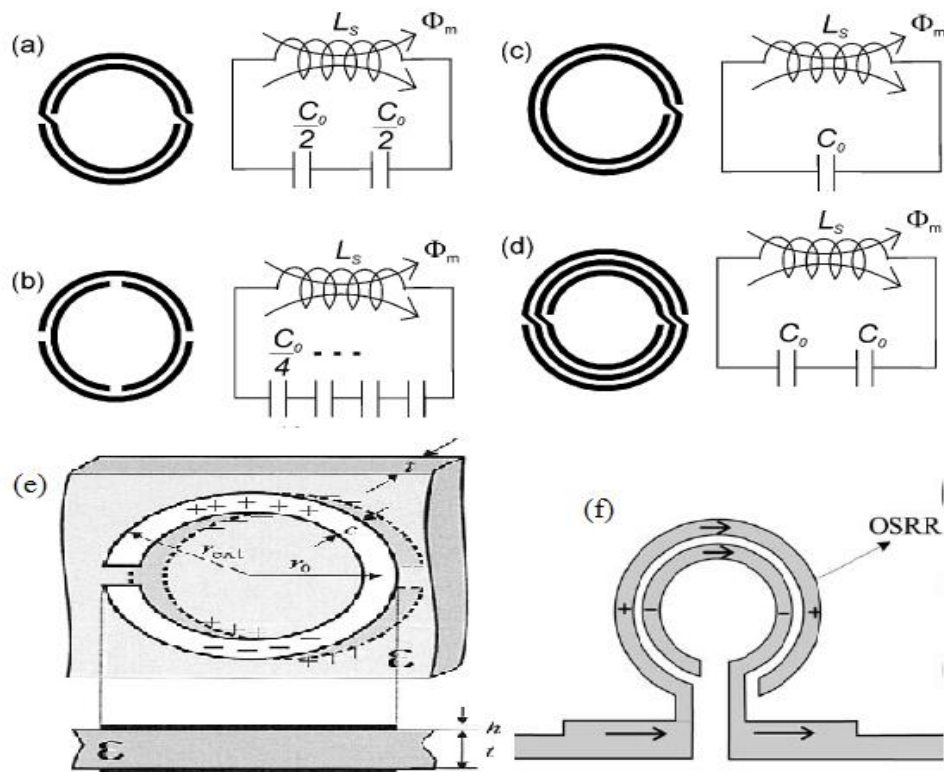


Fig 2.6 Various configurations of the SRR and equivalent models; (a) NB-SRR. (b) D-SRR. (c) SR. (d) DSR. (e) Broadside coupled split-ring resonator (BC-SRR). (f) OSRR [14][54][55].

A more size reduction can be accomplished by using the metallic strips shaping coupled with resonators through their broadsides. This design can be achieved using two parallel metal sheets implementing the resonators. In

broadside coupling, a higher capacitance is achieved, which reduces the resonance frequency of the resonator [55].

2.4 Estimating the Effective Permittivity and Permeability

To compute the effective parameters of the medium from the predicted S-parameters of the wave incident normally on the slab of metamaterial unit cell, the retrieval method presented in [57] is used. The thickness of the slab is also needed for the retrieval process. When a plane wave is normally incident on the slab of a metamaterial, then the constitutive effective impedance z_{eff} and the effective refractive index n_{eff} for the slab of metamaterial unit cell are extracted using the Fresnel's relations of the normally-incident wave by inverting S-parameter data.

$$z_{eff} = \mp \sqrt{\frac{(1+S_{11})^2 - S_{21}^2}{(1-S_{11})^2 - S_{21}^2}} \quad (2-1)$$

The correct sign of the z_{eff} in (2-1) is obtained by enforcing the conditions of passive material which the effective impedance real part and refractive index imaginary part is above zero.

$$e^{in_{eff}k_0d_{eff}} = \frac{S_{21}}{1-S_{11}R_{01}} \quad (2-2)$$

The refraction index can be calculated from;

$$n_{eff} = \frac{1}{k_0d_{eff}} \{Im[\ln(e^{in_{eff}k_0d_{eff}})] + 2m\pi - iRe[\ln(e^{in_{eff}k_0d_{eff}})]\} \quad (2-3)$$

$$m = 0, 1, 2, \dots$$

Where d_{eff} is the metamaterial slab thickness, k_0 is the wave number, m is the branch index of an integer number and $R_{01} = \frac{z_{eff}-1}{z_{eff}+1}$ depends on the obtained effective impedance. Though the imaginary part in (2-3) can be determined accurately, the real part has multiple solutions due to branch ambiguity of the complex logarithm function. To determine it uniquely and

accurately, the method [58] based on the Kramer-Kronig relationship can be achieved. Separating the real and imaginary parts of (2-3), the refractive index and the extinction coefficient become

$$N_{eff} = \frac{Im[\ln(e^{in_{eff}k_0d_{eff}})]}{k_0d_{eff}} + \frac{2m\pi}{k_0d_{eff}} = n_{eff}^0 + \frac{2m\pi}{k_0d_{eff}} \quad (2-4)$$

$$k_{eff} = -\frac{iRe[\ln(e^{in_{eff}k_0d_{eff}})]}{k_0d_{eff}} \quad (2-5)$$

Where n_{eff}^0 is the refractive index corresponding to the principal branch of the logarithmic function. The procedure of extracting the parameter takes advantage of the fact that the imaginary part of the refractive index is not affected by the branches of the logarithmic function. Therefore, it can be calculated from (2-5) without any ambiguity. By applying the Kramers–Kronig relation to determine the real part for the entire frequency range of the S-parameter the approximation of the Kramers–Kronig relation is:

$$\psi_{i,j} = \frac{\omega_j k_{eff}(\omega_j)}{\omega_j^2 - \omega_i^2} + \frac{\omega_{j+1} + k_{eff}(\omega_{j+1})}{\omega_{j+1}^2 - \omega_i^2} \quad (2-6)$$

$$n^{kk}(\omega_i) = 1 + \frac{\Delta\omega}{\pi} (\sum_{j=1}^{i-2} \psi_{i,j} + \sum_{j=i+1}^{N-2} \psi_{i,j}) \quad (2-7)$$

Substituting the refractive index predicted by the Kramers–Kronig relation in (2-4), the branch number is expressed as

$$m = Round[(n^{kk} - n_{eff}^0) \frac{k_0d_{eff}}{2\pi}] \quad (2-8)$$

Where the function rounds towards the nearest integer. The refractive index is calculated depending on predicted branch number which is substituted in (2-3), once z_{eff} and n_{eff} are obtained from the above equations. The effective permittivity ϵ_{eff} and the effective permeability μ_{eff} can then be calculated from the equations below:

$$\epsilon_{eff} = \frac{n_{eff}}{z_{eff}} \quad (2-9)$$

$$\mu_{eff} = n_{eff}z_{eff} \quad (2-10)$$

Another method can be used to estimate the effective medium parameters from the predicted S-parameters as mentioned in [59][60].

2.5 Applications of the Metamaterials

Metamaterials have found many applications in the microwave and optical frequencies due to their unusual properties which have been utilized in diverse fields. In the following various applications are described.

2.5.1 Metamaterials as Transmission Lines

Transmission lines using the Left-handed metamaterials are implemented in the form of coplanar, stripline and microstrip. These geometries are convenient in manufacturing planar processes which are appropriate in microwave devices design. These manufacture lines offer significant advantages such as compact size and design flexibility; in addition to the characteristic impedance and phase which allow manipulate the desired properties [61].

Fig. 2.7.a shows the equivalent circuit of the right-handed transmission line. The circuit comprises inductors in series and shunts capacitors, whose sizes are much smaller than the wavelength λ in frequency operation. The important properties of metamaterials are dispersions, characteristic impedance, phase velocity, and other properties which can be calculated from the circuit model. The left-handed transmission line equivalent circuit illustrated in Fig. 2.7.b in this model, the inductors of the right-handed transmission line model are swapped by capacitors. Moreover, inductors substitute all shunt capacitors. This ideal model gives the same performance, although it may not exist in nature. The CRLH transmission lines equivalent

circuit is an integration of both RH transmission lines and LH transmission lines equivalent circuits, as shown in Fig. 2.8 [62].

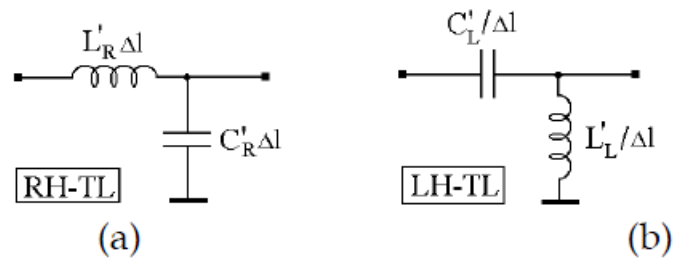


Fig. 2.7 The equivalent circuit models of metamaterial transmission lines; (a) right-handed (b) left-handed [62].

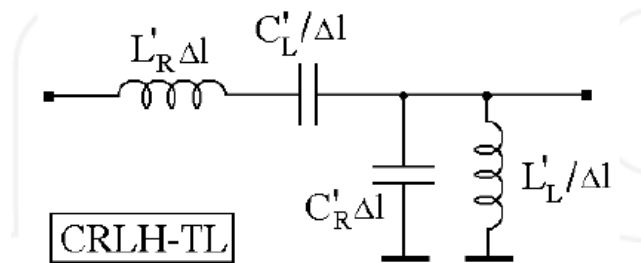


Fig. 2.8 The equivalent circuit of the composite right-hand/left-hand metamaterial transmission line [62].

2.5.2 Superlens

The superlenses use metamaterials to attain resolutions beyond that obtainable from conventional lenses that are limited by the diffraction limit which is an essential property of the conventional lenses. Due to the negative refractive index of metamaterials the first application was in optics when Pendry claimed that a metamaterial lens had a power of light focusing for slab material geometric size less than wavelength λ [9]. As an example in this case, the visible light wavelength is smaller than the slab atoms which can never be seen even by the use of optical microscopes.

The traditional lens used to focus the wave only therefore imperfect image is achieved from the target. The loss in the details of small wavelength target conveyed in the evanescent waves is caused by the high attenuation

when these waves move from the target to the image. The diffraction limit originates from this attenuation in the evanescent spectrum. In lenses based on metamaterials, perfect target image is achieved by helping the growing evanescent spectrum, which enhances the attenuated evanescent waves radiated from the target. In this way, the lens resolution is considerably improved [63].

2.5.3 Cloaking Devices

The cloak function is to deflect microwave beams falling on an object, so the wave propagate around and inside the object with low distortion. The result appears almost as if nothing were there in their way. Metamaterials form the basis that aims to build a practical cloaking device. Such a device usually involves surrounding the object to be cloaked with a region, which affects the passage of light or electromagnetic waves near the object.

With a target object surrounded by a left-handed metamaterial, and if the electromagnetic wave transmission in the metamaterial is properly optimized, the waves can act to circumvent the target object. Such technology is referred to as radio cloaking. Fig. 2.9 shows a prototype of a doughnut-shaped left-handed metamaterial. Radio waves are entering this body, change their traveling direction inside, propagate avoiding the center space, and are emitted out of the body again as if they have circumvented the body [64].

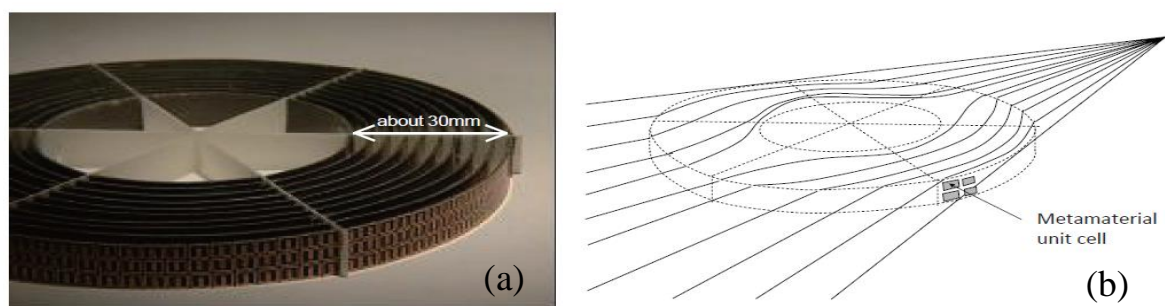


Fig. 2.9. Radio Cloaking. (a) Two-dimensional microwave cloaking structure [64]. (b) State of transmission of electromagnetic waves [65].

2.5.4 Metamaterial Antennas

Metamaterial antennas employ metamaterials to enhance their characteristics. Antenna radiated power can be improved using the metamaterials. Materials having a negative magnetic permeability (MNG) can offer the possibility to design electrically small antennas, achieve high directivity, and tunable operational frequency. Furthermore, metamaterial-based antennas have demonstrated improved efficiency-bandwidth.

An appreciable improvement in the antenna performance has been obtained by using metamaterials that exhibit a negative electric permittivity, a negative magnetic permeability, or both ENG/MNG. Antennas designed using these types of metamaterials have substantial potential for solving the limitation of efficiency-bandwidth in natural or conventionally electrically-small antennas.

Metamaterials employed in the ground planes of the antennas offer improved isolation between adjacent elements in multiple input multiple output (MIMO) antenna arrays. Metamaterials that produce a high impedance of ground planes are used to enhance the radiation efficiency, and axial ratio performance of low-profile antennas are located close to the ground plane surface [66].

In radar systems, mechanical scanning of a directional narrow-beam antenna can be replaced by phasing of the electromagnetic wave inside the antenna to scan the beam without rotation. A backward wave from a left-handed metamaterial can be used to effectively broaden the range of the beam scanning. Sweeping the frequency of the e.m. wave from the right-handed frequency band to the left-handed frequency band, both of the ordinary forward wave (e.m. wave in a right-handed medium) and the backward wave can be used. The doubled range in phase shift can double the scanning range by the antenna beam, as shown in Fig. 2.10 [51].

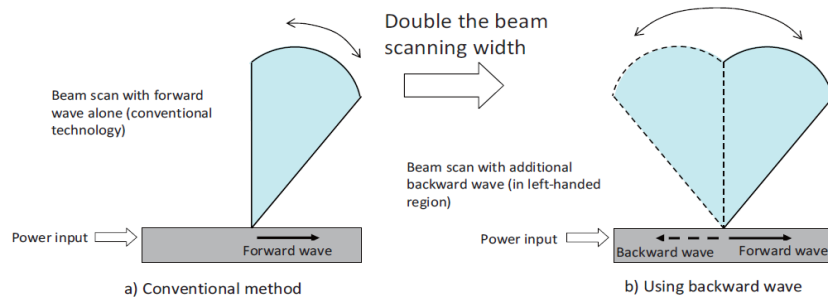


Fig. 2.10. A practical example of the beam scanning of a radar antenna [51].

2.5.5 Couplers

The characteristics of a left-handed transmission line can be utilized to provide a device that has a special effect applicable to electromagnetic appliances. Fig. 2.11 shows devices in which two transmission lines are placed close to each other. Such devices, called “couplers,” can transfer the e.m. waves propagating in each of the transmission lines to the other for power distribution or transmission, and are in use for various power handling purposes.

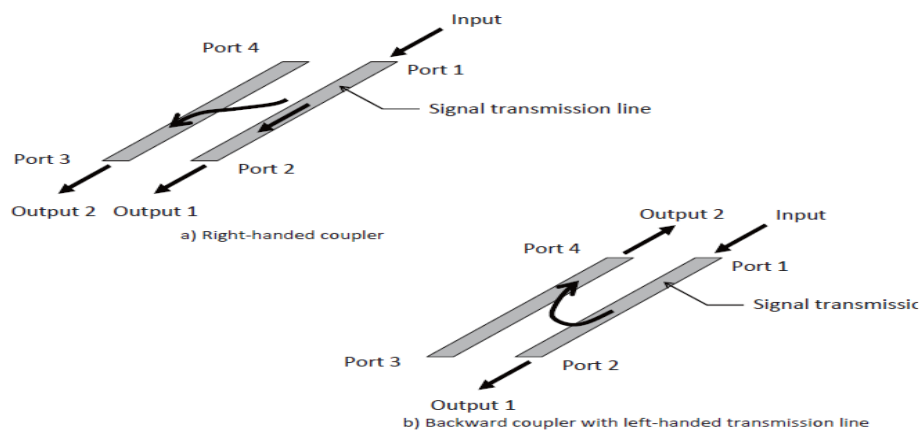


Fig. 2.11 Backward Coupler [51].

A backward coupler enables the adjustment of system characteristics for improved performance and size reduction. A coupler with ordinary right-handed transmission lines, Fig. 2.11.a splits and transmits the electromagnetic wave in the same direction, i.e., from port 1 to ports 2 and 3. If both of these

transmission lines are made of a left-handed metamaterial, Fig. 2.11.b, and if the parameters between the transmission lines are optimized as to form a backward coupler, the wave can couple the terminals on the same side, namely ports 1 and 4 in the diagram, to each other with the desired characteristics [51].

2.5.6 Microwave Filters

The first resonated metamaterial transmission lines have been extensively used to design different types of microwave devices. Such designs have shown improved performance, compact dimensions, multi-band operation, tunability, and other interesting characteristics. Transmission lines using metamaterials unit cell-like complementary split rings resonators (CSRRs) help to design microwave circuits that are compact as compared to conventional designs. Typical structures comprise microstrip lines with CSRRs embedded in the ground plane, as well as series capacitive gaps. Therefore, the dispersive transmission medium supporting the backward (left hand) of propagation wave at certain frequencies around the resonance is obtained [67].

The CSRR-based artificial transmission lines have been also applied to power dividers, making them suitable for narrowband applications where low loss and compact size are highly desirable. Moreover, there are no lumped elements in these structures, as the elements are distributed along the line leading to a simpler design and lower fabrication costs [67][68].

Metamaterial transmission lines offer a large number of degrees of freedom, thus allow controlling the line dispersion characteristics. The possibility to control dispersion can be utilized into bandwidth enhancement purposes. Dealing with dispersion can help in the design of devices such as baluns, phase shifters as well as hybrid couplers, which use two or more lines. Here the phase difference between the transmission lines is essential as the derivative the bandwidth from this difference's [61].

The sub-wavelength application of resonators into filter design is to combine a transmission line with a resonator that produces a stopband at those resonate frequencies where the structure behaves as SNG medium due to the resonators. It is possible to tune the resonators for rejecting signal at very small different frequencies so that to control a band rejection with a specific bandwidth, which is also controlled by many resonators [17]. In the following, various types of filters are discussed.

2.5.6.1 Band Pass Filters (BPF)

Gill et al. designed and fabricated BPF based on a left-handed microstrip line and periodically loaded by square SRRs and metallic vias [69]. The squared-SRRs are loaded periodically near the conducting microstrip line and metallic vias that illustrated in Fig. 2.12. The metallic via works as shunt connected inductors L_p . The squared-SRRs are represented by a resonant inductance L_s and capacitance C_s circuit. His design showed a narrow bandpass filter with compact size.

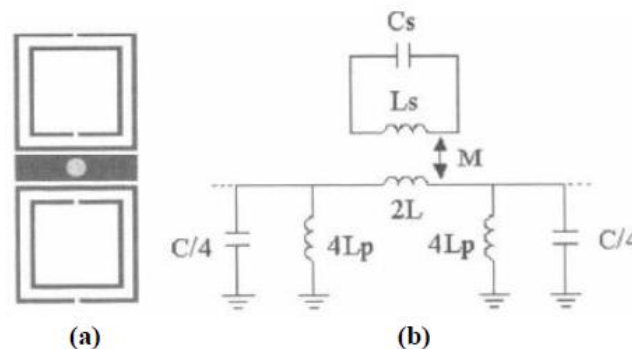


Fig. 2.12. (a) The basic cell of the left-hand (LH) metamaterial microstrip line. (b) equivalent circuit model [69].

Bonache et al. designed compact bandpass microstrip filters using the idea of CSRRs [67]. Based on cascading filter stages that consist of the combination of complementary split-ring resonators (CSRRs), series capacitive gaps, and grounded stubs offer the possibility to synthesize filter

with size compactness and ability to control the bandwidth. The equivalent circuit model filter has shunt stubs (inductors), and series gaps (capacitors) and the CSRR's have been modeled by the parallel resonant structure [67].

Jiusheng and Tieying proposed a left hand (LH) metamaterial using microstrip gap technology. Series microstrip gaps representing a capacitor and holes that represent a shunt inductor was used to build the unit cell. In such an arrangement, the unit cell represents a bandpass filter whose advantages are high return loss, low transmission loss, and low fabrication cost [70].

Singhal presented a compact bandpass filter using metamaterial resonator. His design shows a low insertion loss, narrow bandwidth, and compact dimensions. This structure has negative effective permittivity and permeability, leading to a compact size and excellent performance [71].

2.5.6.2 Band Stop Filters (BSF)

A super-compact band-stop microstrip based on CSRR's is proposed by Falcone et al. [72]. The structure is very compact and has flat and lossless passband with a deep band rejection and sharp cut-offs stopband. Thomas et al. designed a left hand (LH) metamaterial building from repeated symmetric split-ring resonators SSRRs, as shown in Fig. 2.13 [73]. The metallic SSRR's are printed sixteen times on the dielectric strip in order to realize the metamaterial substrate. The substrate behaves as a bandstop filter. The enhancement in the bandwidth of a $\frac{1}{4}$ wave stub stopband filter is attained by utilizing the natural stopband of the substrate.

Kshetrimayum et al. designed band-stop filters by etching periodic patterns of complementary split ring resonators (CSRR's) in the ground plane of a microstrip line [24]. The size of the sub-wavelength resonators of CSRR's is much smaller than that of the conventional microstrip resonators (see Fig.

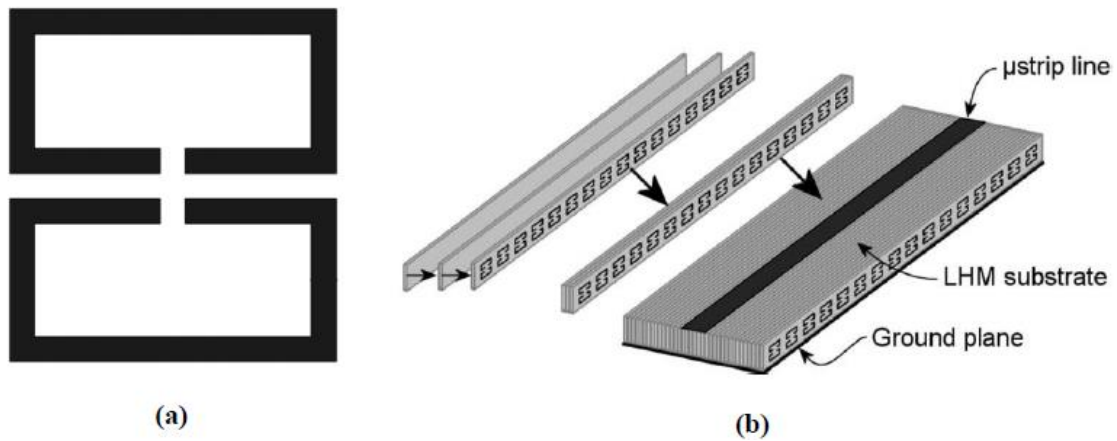


Fig 2.13. (a) The symmetric split ring resonator (SSRR). (b) Fabricated Metamaterial substrate using combined SSRR's dielectric strips [73].

2.14). The single CSRR in the ground plane has a very high Q factor that leads to a very low insertion loss along the stopband.

The period of the CSRR loaded microstrip line can be made as small as 0.1 the operating wavelength thereby achieving considerable size reduction. By increasing the number of the CSRR's and decreasing the periodic structure, the stop bandwidth increases and the insertion loss level in the mid stopband frequency decreases significantly [24].

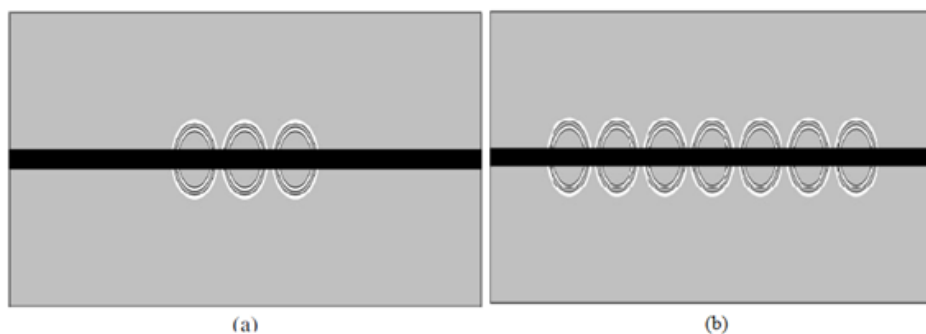


Fig. 2.14 The stopband filter was employing periodic loading of CSSR's in the ground plane; (a) 3 CSSR's, (b) 7 CSSR's [24].

2.5.6.3 Low Pass Filters (LPF)

Abid presented a maximally flat low-pass filter, which incorporated CSRR's to achieve high selectivity with compact design size [74]. LPF design

is integrated with the benefits stopband characteristic of the complementary split ring resonators (CSRR). The design enhances the roll-off, offers smaller size while keeping the passband performance. Sahu et al. designed an enhance characteristic with small size microstrip LPF using a complimentary hexagonal-omega cell in the ground shown in Fig. 2.15. This design improves the rolloff with maintaining passband performance and equivalent to an (LC) circuit resonant [31].

Karuppiah designed a new compact microstrip Bessel LPF using complementary split ring resonators (CSRR's) as shown in Fig. 2.16 [75]. The proposed LPF has a linear phase response and sharper cut-off behavior, leading to a constant group delay over the passband and rejects the undesired frequencies without the need to increase the order of the filter.

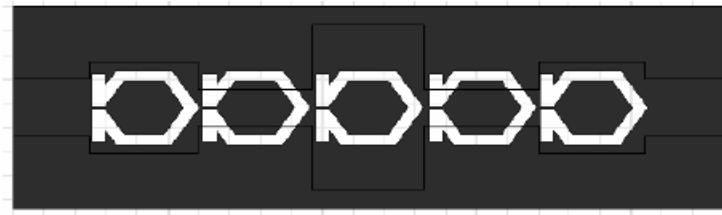


Fig 2.15 The topology of embedded hex-omega structures underneath LPF in the ground plane [31].

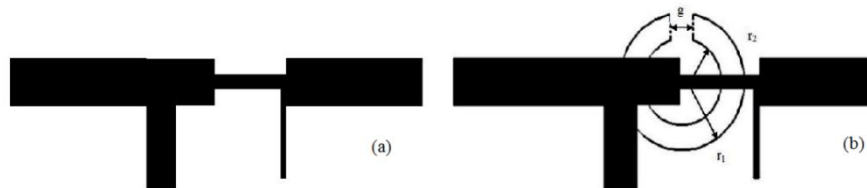


Fig 2.16. Distributed Bessel LPF design; (a) without CSRR, (b) with CSRR [75].

Suganthi et al. proposed a design of a third order Chebyshev type microstrip low pass filter (LPF) loaded with an array of split ring resonator (SRR) as an additional plane between the ground and filter sections for

superior performance [76]. The proposed SRR type metamaterial preparation is based on the V-shaped structures, as shown in Fig. 2.17. The novel V-shaped metamaterial structure as SRR array is laid as performance improving cover between filter section and the conventional ground layer.

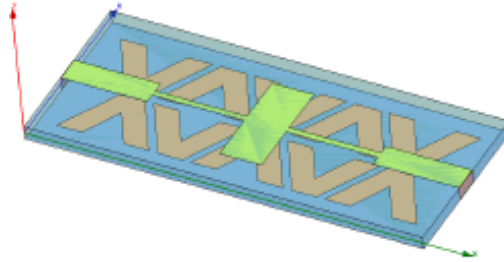


Fig 2.17. An array of V structures placed underneath the loaded LPF [76].

2.5.6.4 High Pass Filters (HPF)

Gil et al. designed high pass filters by using microstrip line etched complementary split rings resonators (CSRR) depending on balanced composite right-left handed (CRLH) transmission lines [22]. The design basic cell structure and the equivalent (T-circuit) model are shown in Fig. 2.18.

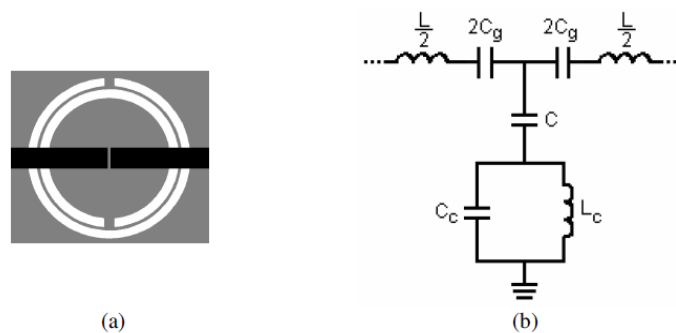


Fig. 2.18. The HPF; (a) basic cell design, (b) equivalent (T-circuit) model[22].

The design consisting embedded CSRR in a ground plane located underneath a capacitive gap (inter-digital capacitors) etched on the top layer (conductor strip), can use two to four cells. The three-cell structure shown Fig. 2.19 exhibits low in-band losses and reasonable return losses. The large bandwidth of the high pass filters is achieved [22]. Duvey et al. designed

highly selective filters based on the same structure of Gil who followed the same design to obtain high pass filters with very sharp cut-off, by cascading metamaterial resonant particles [77].

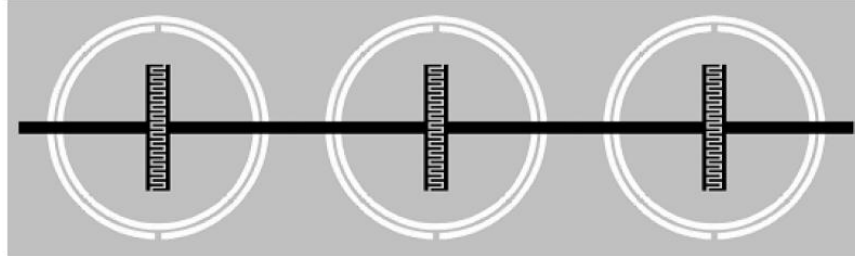


Fig. 2.19. The layout of the filter formed by three CSRR cells [22].

CHAPTER THREE

DESIGN AND INVESTIGATION OF BANDSTOP FILTERS USING U-SHAPED SLOTS

CHAPTER THREE

DESIGN AND INVESTIGATION OF BANDSTOP FILERS USING U-SHAPED SLOTS

3.1 Introduction

Planar metamaterial structures have been suggested to perform various functions regarding the electromagnetic waves in various applications such as reflection, transmission, and absorption. These structures can have the form of certain metallic patterns printed on a substrate. Devices built from such structures have shown performances that compete and even surpass those built from natural materials. In this chapter, a U-shaped slot is proposed as a metamaterial building unit. The U-shaped slot is deployed in the conventional transmission line formed in the microstrip technology. The slot is used in the proposal of various configurations for bandstop filters. The feasibilities of four proposed filters using single and double slots are investigated in the next sections. Experimental verification of the proposed designs is also given.

3.2 The Band-Stop Filter Using U-Shaped Slot.

The configuration of the proposed filter using a single U-slot etched on the microstrip line is shown in Fig.1. The used substrate is FR4 with a dielectric constant of 4.4 and 0.025 tangent loss, while copper (annealed) is used for the microstrip line and the ground plane. The dimensions of the substrate are chosen to be 60mm × 20mm × 1.6mm, and the microstrip line width was calculated according to Eq. 3.1 to be 3.05mm to achieve 50Ω impedance [78].

$$Z = \frac{120\pi}{\sqrt{\epsilon_r}[w/hs + 1.393 + 0.667 \ln(w/hs) + 1.444]} \quad (3.1-a)$$

$$\varepsilon_{eff} = \frac{\varepsilon_r + 1}{2} + \frac{\varepsilon_r - 1}{2} \left(1 + 12 \frac{hs}{w}\right)^{-0.5} \quad (3.1-b)$$

Where ε_r is the relative dielectric constant of the substrate, hs/w is the ratio of substrate height hs to the line width w .

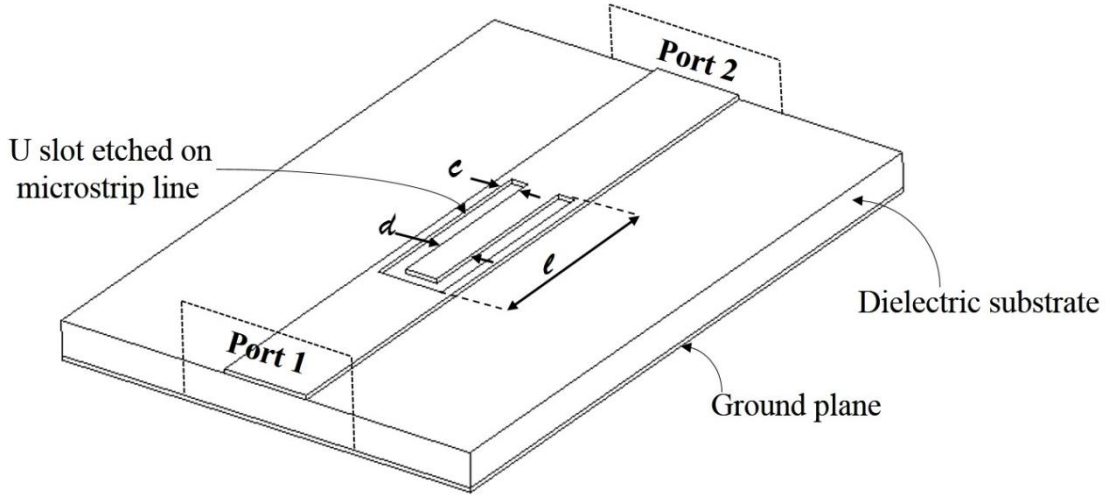


Fig. 3.1 The geometry of the proposed band-stop filter using a U-shaped slot etched on a microstrip line.

The U-shaped slot is formed of three rectangular sections of width e connected together with a length of l and inner separation d . According to the dimensions shown in Fig. 3.1, the length of the slot is given by:

$$LS = 2 \times (\ell - e/2) + d + 2(e/2) = 2\ell + d \quad (3.2)$$

The slot resonates when its length is equal to half the effective wavelength. Using Eq. 3.1.b and to obtain resonance at the 2.45GHz frequency, the value of ε_{eff} is equal to 3.33, and the designed slot dimensions are; $\ell = 18.2\text{mm}$, $e = 0.5\text{mm}$, $d = 1.0\text{mm}$, thus the overall length of the U-slot is 37.4mm. The 50Ω value of impedance is used for all simulations that are performed by using the CST microwave studio suite. The boundary conditions are set to open in all sides except the ground plane, which was set as PEC surface. The calculated scattering parameters S_{11} and S_{21} of the proposed filter

are plotted as a function of signal frequency in Fig. 3.2. The designed U-slot provides the band-rejection property of 15.4 dB insertion loss at 2.449GHz. At this frequency, the length of the slot (37.4mm) is equal to $0.56 \lambda_e$, where $\lambda_e = \lambda_0 / \sqrt{\epsilon_{eff}}$. It can also be seen that the band reject feature is repeated at a higher frequency of 7.34GHz, which is about 3 times the first frequency of 2.449GHz. This is a case in which the slot length is 1.5 of the effective wavelength at the 7.34GHz frequency.

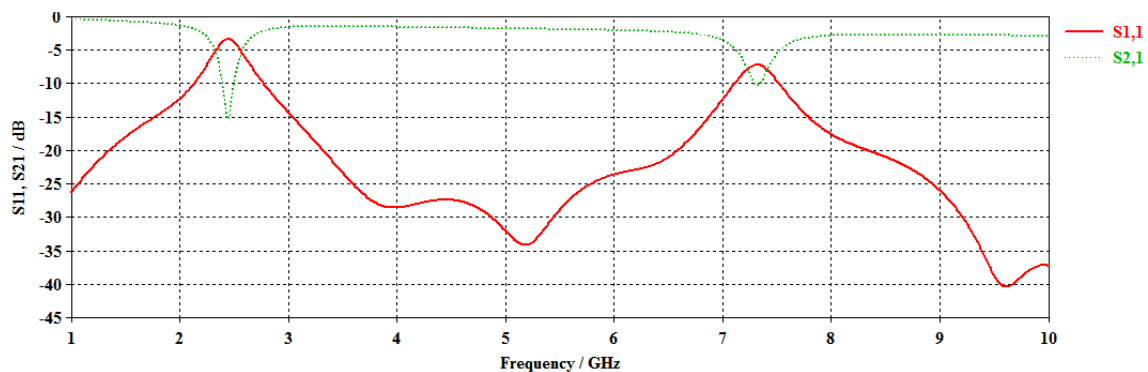


Fig. 3.2 Transfer characteristics of the U-slot filter; ($\ell = 18.2\text{mm}$, $\epsilon = 0.5\text{mm}$, and $d = 1.0\text{mm}$).

The characteristics of the U-slot filter, such as the resonance frequency and band rejection, depend on the structural parameters of the U-slot. The slot length, slot width, and distance between the two legs of the slot are the parameters that control the transfer characteristics. In Fig. 3.3, the simulated transfer characteristics for the U-slot filter are plotted for various slot lengths while keeping $\epsilon = 0.5\text{mm}$ and $d = 1.0\text{mm}$ constants. The figure shows that as the slot length increases, whereas the resonance frequency decreases.

The simulated transfer characteristics for various slot widths are shown in Fig. 3.4, when $\ell = 18.2\text{mm}$, and $d = 1.0\text{mm}$. The width of the slot influences the width of the reject band, as can be seen, that a larger width results in wider bandwidth, with slightly higher values of S_{11} , and lower values of S_{21} . The position of the band is very slightly affected.

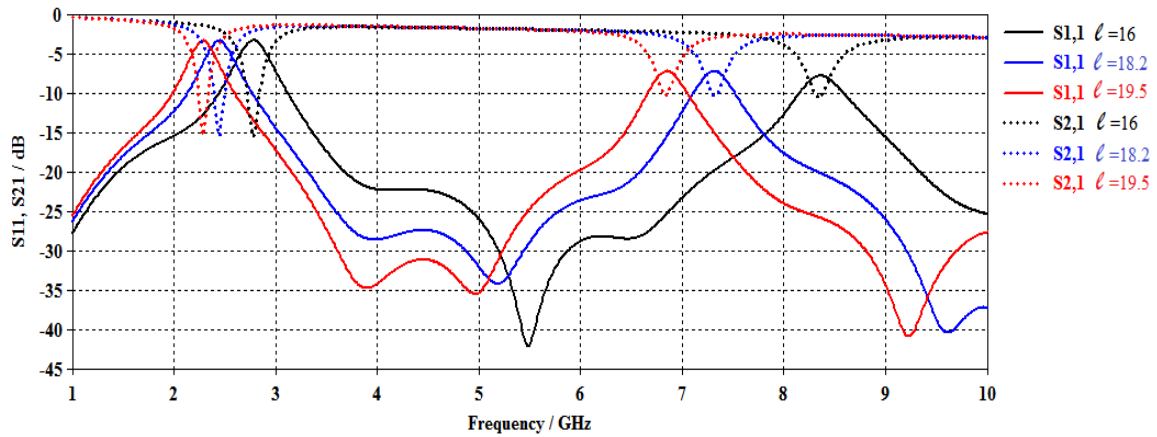


Fig. 3.3 Transfer characteristics of the U-slot filter for various slot lengths (ℓ), ($e=0.5\text{mm}$, $d=1.0\text{mm}$).

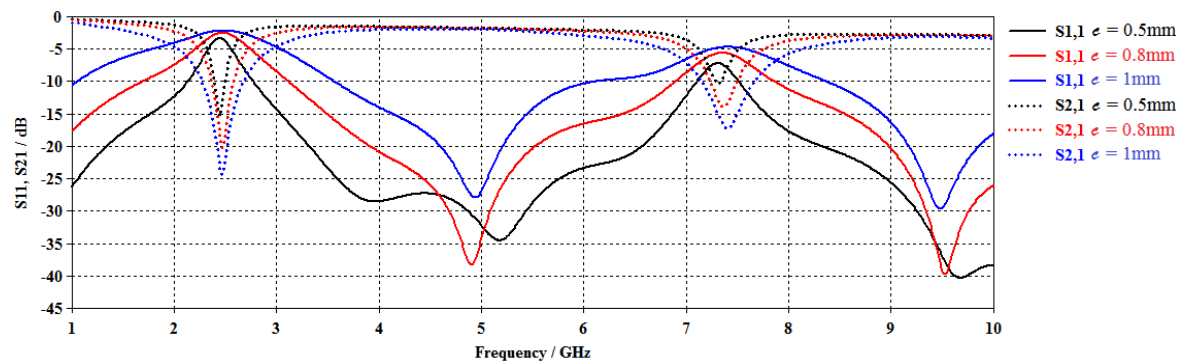


Fig. 3.4 Transfer characteristics of the U-slot filter for various slot widths (e); ($\ell=18.2\text{mm}$, $d=1.0\text{mm}$).

Figure 3.5 shows the U-slot positioned at a distance (a) from the microstrip line end. The simulated transfer characteristics for various slot positions (a) are shown in Fig. 3.6, as the dimensions of the U-slot are kept constant at $\ell=18.2\text{mm}$, $d=1\text{mm}$, $e=0.5\text{mm}$. The performance has very little sensitivity to the slot position.

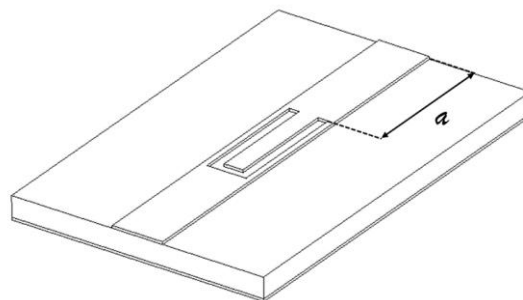


Fig. 3.5 Geometry of the filter with the U-slot positioned at a distance (a) from the end of the microstrip line.

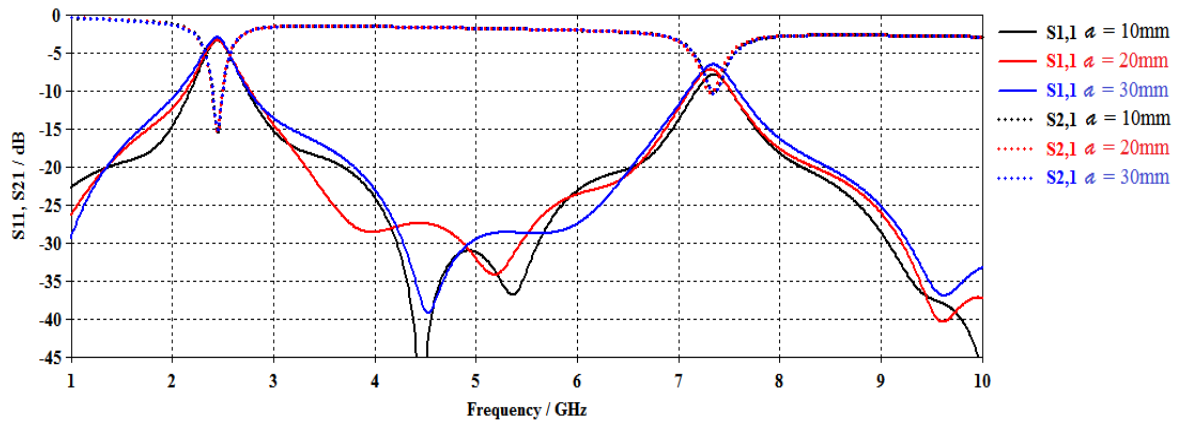


Fig. 3.6 Transfer characteristics of the U-slot filter for various locations of the slot (a) ($\ell=18.2\text{mm}$, $d=1.0\text{mm}$, $e=0.5\text{mm}$).

3.3 Improving the Band Rejection Properties by Using Two Slots

In the following, the effect of using two cascaded slots is investigated in an attempt to improve the performance of the filter. Figure 3.7 shows the two slots placed in facing position, with a separation distance (τ). The calculated performance is shown in Fig. 3.8, where larger rejection has been obtained by using the two slots. The separation slightly affects the position of the stopband. Figure 3.9 shows the simulated transfer characteristics for various slot widths, where it can be noted that the band-reject width increases and the minimum value of the transfer coefficient S_{21} decrease with increasing slot width. Figure 3.10 shows the same effect when the distance (d) between the two legs of the slots increases.

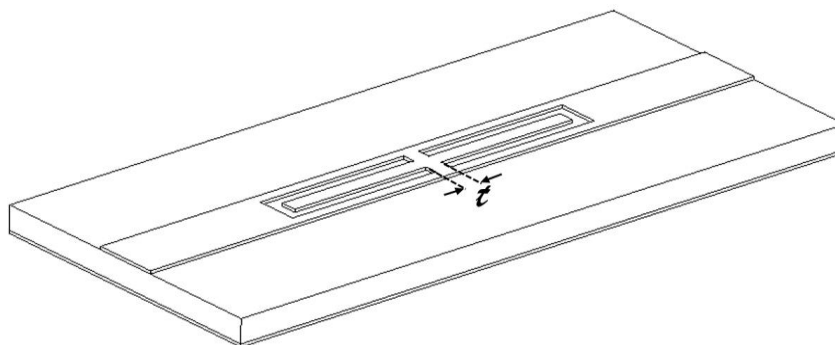


Fig. 3.7 Geometry of the filter with two vis-a-vis U-slot's spaced by τ , $\ell=18.2$ mm, $d=1.0$ mm, and $e=0.5\text{mm}$.

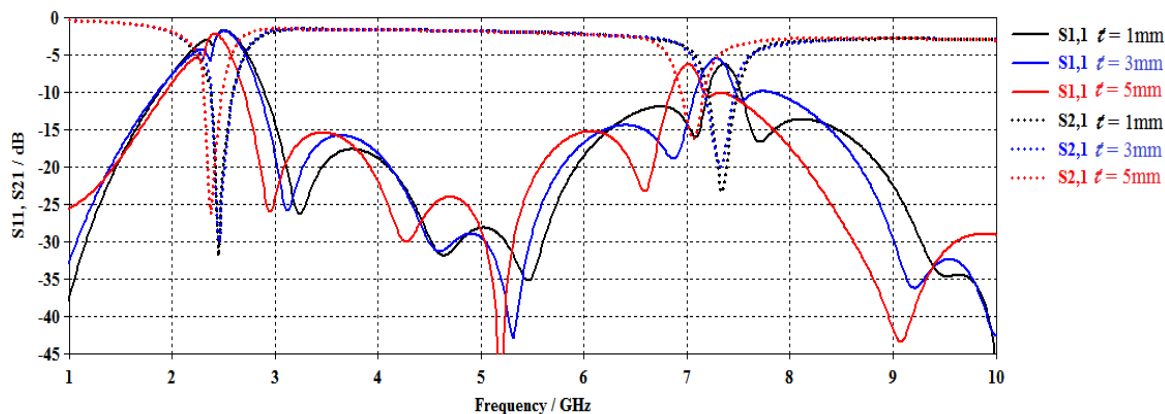


Fig. 3.8 Transfer characteristics of the filter with two vis-à-vis U-slot's for ($\ell = 18.2\text{mm}$, $d = 1.0\text{mm}$, $e = 0.5\text{mm}$).

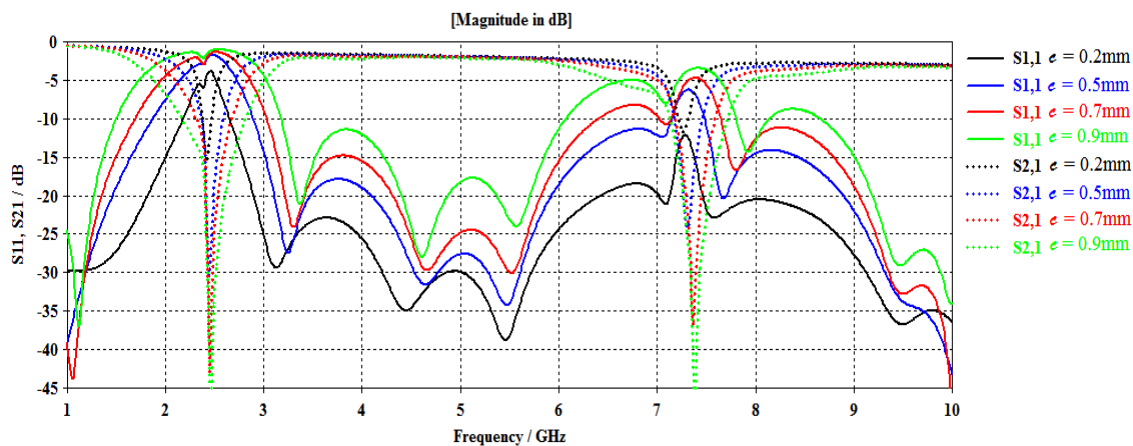


Fig. 3.9 Transfer characteristics of the filter for various slot width e of two vis-à-vis U-slot's for ($\ell = 18.2\text{mm}$, $d = 1\text{mm}$, $t = 1\text{mm}$).

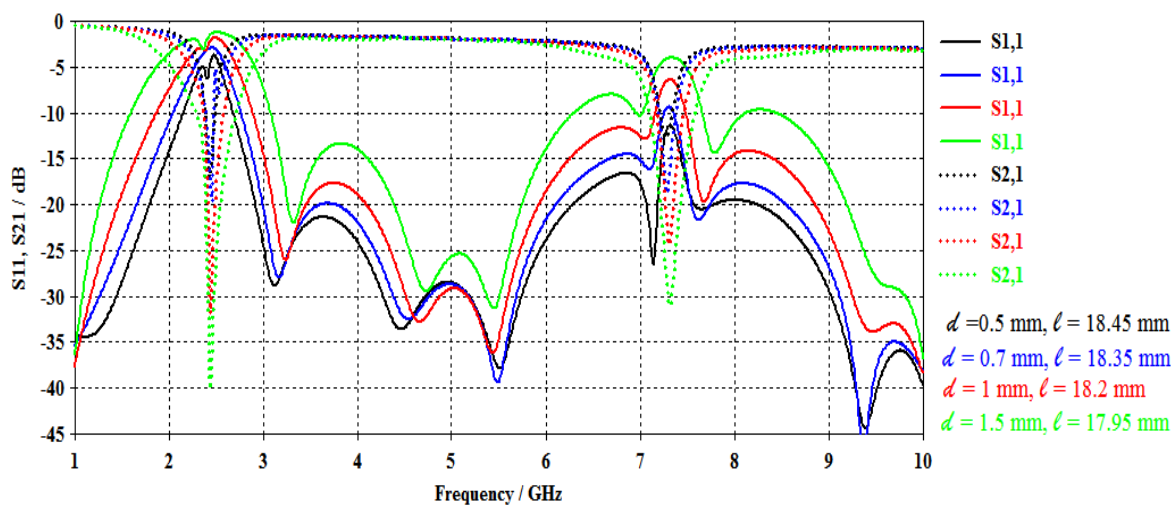


Fig. 3.10 Transfer characteristics of the filter two vis-à-vis U-slot with various separation d : ($e = 0.5\text{mm}$, $t = 1\text{mm}$).

The two U-slots can also be placed in back-to-back arrangement with separation (w), as shown in Fig. 3.11. The calculated performance is shown in Fig. 3.12, where it can be seen that lower rejection is obtained as compared to the design of the face-to-face position. As the separation between the two slots is varied, the position and width of the reject band slightly change.

The simulated transfer characteristics for various slot widths are shown in Fig. 3.13. Wider bandwidth, slightly higher values of S_{11} , and lower values of S_{21} are obtained with increasing the slot width. Figure 3.14 shows the same behavior when the separation between the legs of the slot is increased with decreasing the slot lengths.

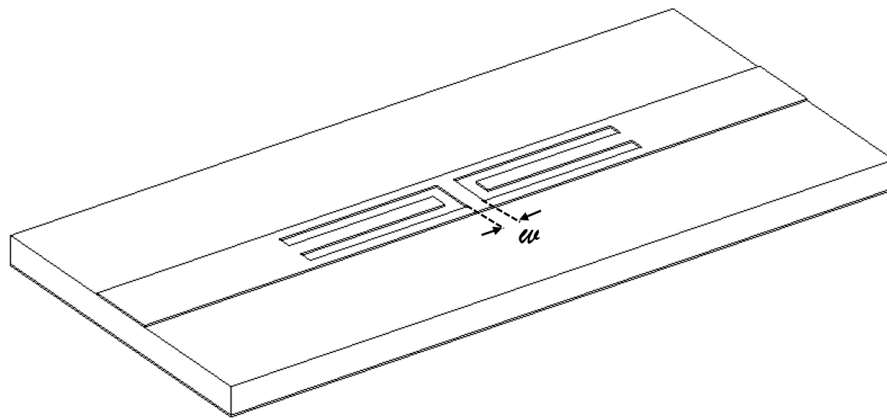


Fig. 3.11 Geometry of the filter with two back-to-back U-slot's with separation of w ; ($\ell = 18.2\text{mm}$, $d = 1.0\text{mm}$, $e = 0.5\text{mm}$.)

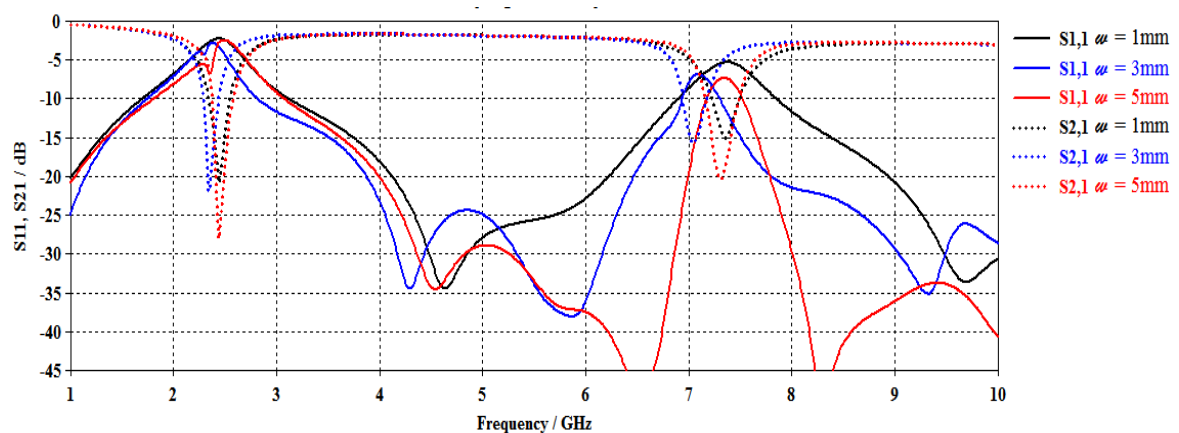


Fig. 3.12 Transfer characteristics of the filter with two back-to-back U-slot's for various separation w at ($\ell = 18.2\text{mm}$, $d = 1.0\text{mm}$, $e = 0.5\text{mm}$).

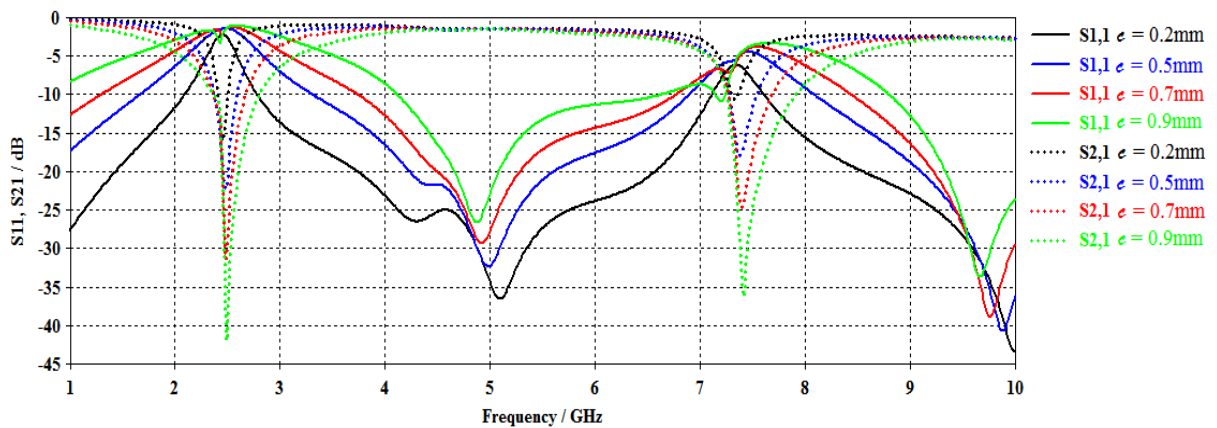


Fig. 3.13 Transfer characteristics of the filter for various slot width ϵ of two back-to-back U-slot for ($\ell = 18.2\text{mm}$, $d = 1\text{mm}$, $w = 1\text{mm}$).

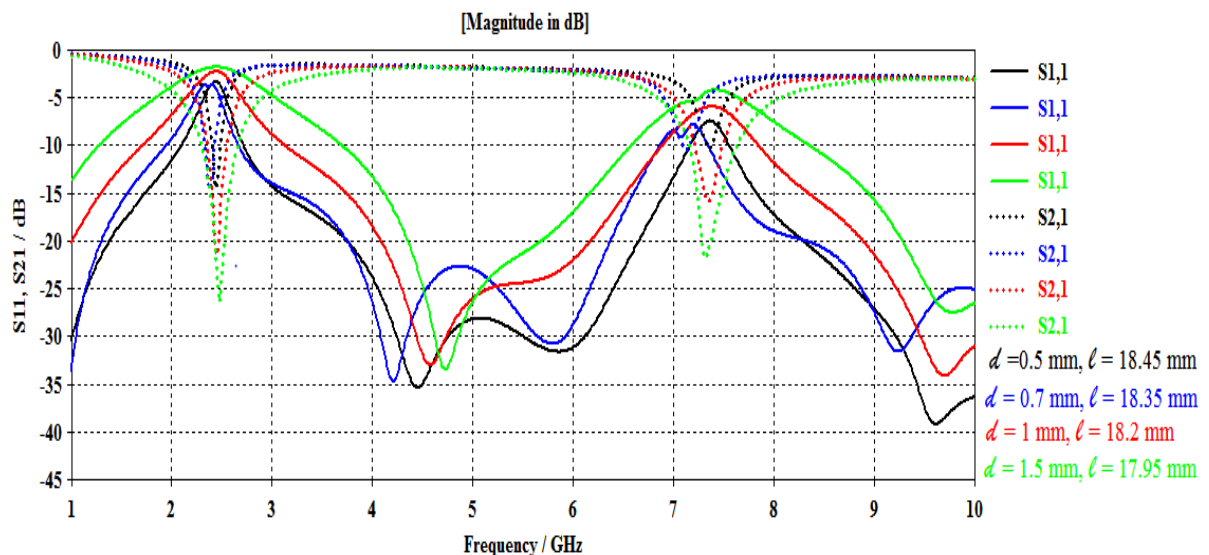


Fig. 3.14 Transfer characteristics of the filter for various distances between two slots d and slot lengths ℓ of two back-to-back U-slot for ($\epsilon = 0.5\text{mm}$, $w = 1\text{mm}$).

In the next step, the two U-slots are interlaced keeping a separation (d) between them, as shown in Fig. 3.15. This arrangement provides larger coupling and smaller overall length as compared to the two former arrangements. The performance of this arrangement is shown in Figs. 3.16, 3.17, and 3.18 for a wide range of separation (d). It can be seen that the width of the reject band has increased as compared with that of the two former

arrangements of the two U-slots. The increased width can be attributed to the fact that there are two responses due to the two slots. The effect of mutual coupling between the two slots is now larger as the four legs of the two slots are now very close to each other, and thus having larger mutual coupling. The two responses add together leading to a broader reject band. Figures 3.16 to 3.18 show that there is good flexibility in designing the reject band by varying the separation between the two slots while the center frequency remains almost the same as the dimensions of each slot are kept constant.

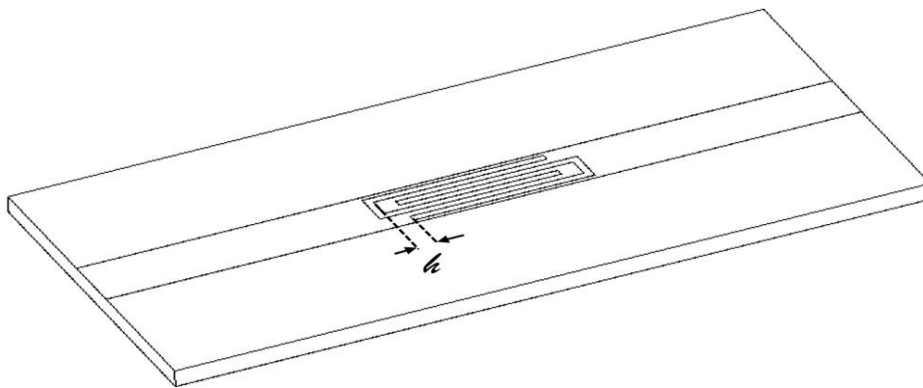


Fig. 3.15 Geometry of the filter with two interlaced U-slots with separation l ; ($l=18.3\text{mm}$, $d=1.2\text{mm}$, $e=0.4\text{mm}$).

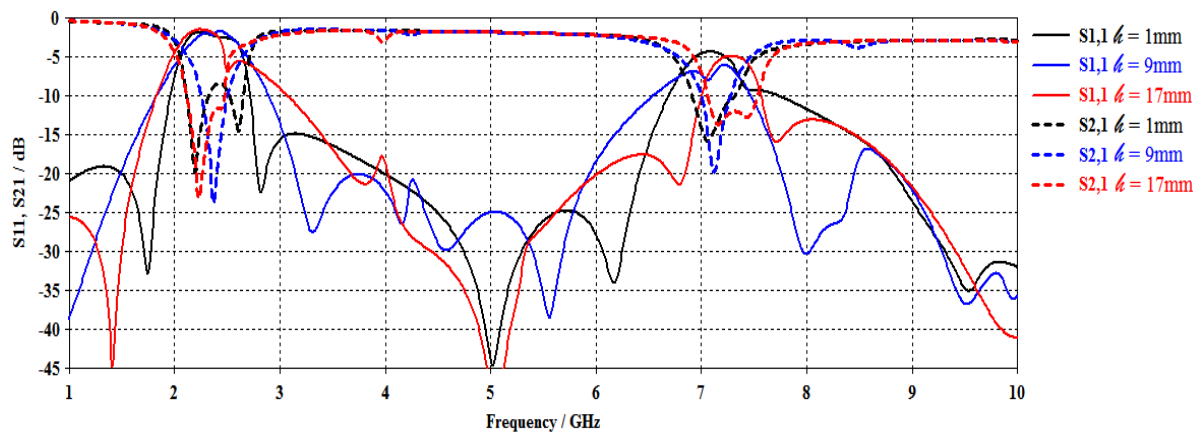


Fig. 3.16 Transfer characteristics of the filter with two interlaced U-slots for various separation l ($l=18.3\text{ mm}$, $d=1.2\text{mm}$, $e=0.4\text{mm}$).

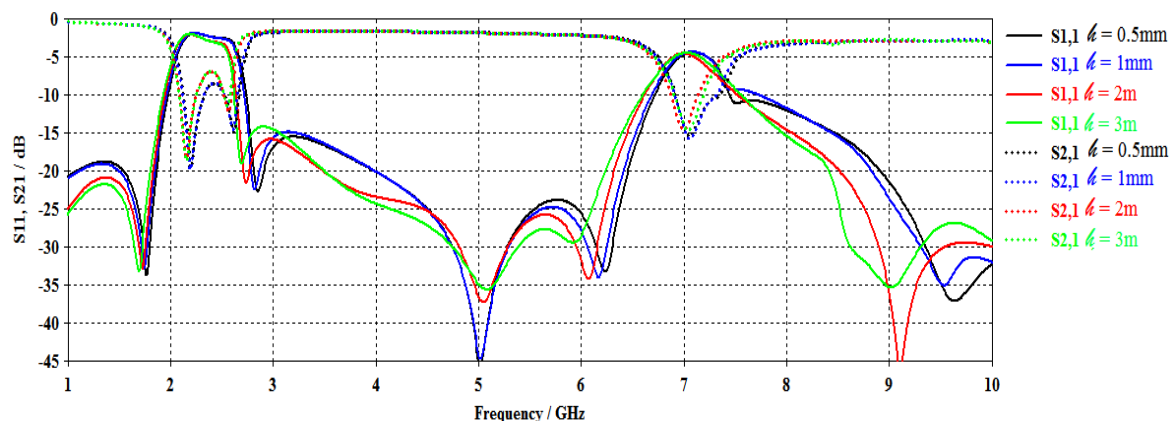


Fig. 3.17 Transfer characteristics of the filter with two interlaced U-slots with various separations ℓ ($\ell = 18.3\text{mm}$, $d = 1.2\text{mm}$, $e = 0.4\text{mm}$).

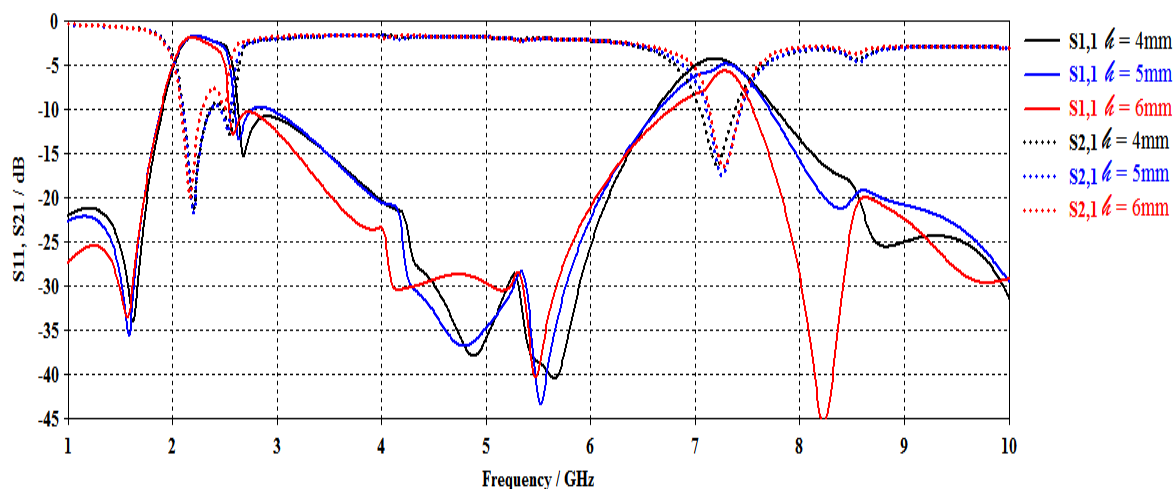


Fig. 3.18 Transfer characteristics of the filter with two interlaced U-slots for various separation ℓ ($\ell = 18.3\text{mm}$, $d = 1.2\text{mm}$, $e = 0.4\text{mm}$).

The effect of using different slot widths e for the two interlaced U-slots was also investigated. Figure 3.19 shows the calculated performance for the two interlaced U-slots of various slot widths e , where it is shown that by increasing the slot width, the width of the band-reject is increased. Figure 3.20 shows the simulated transfer characteristics for various separations between the two slots d where it can be noted that the width of the reject-band, as well as the minimum value of S_{21} , decrease with an increase in the width d .

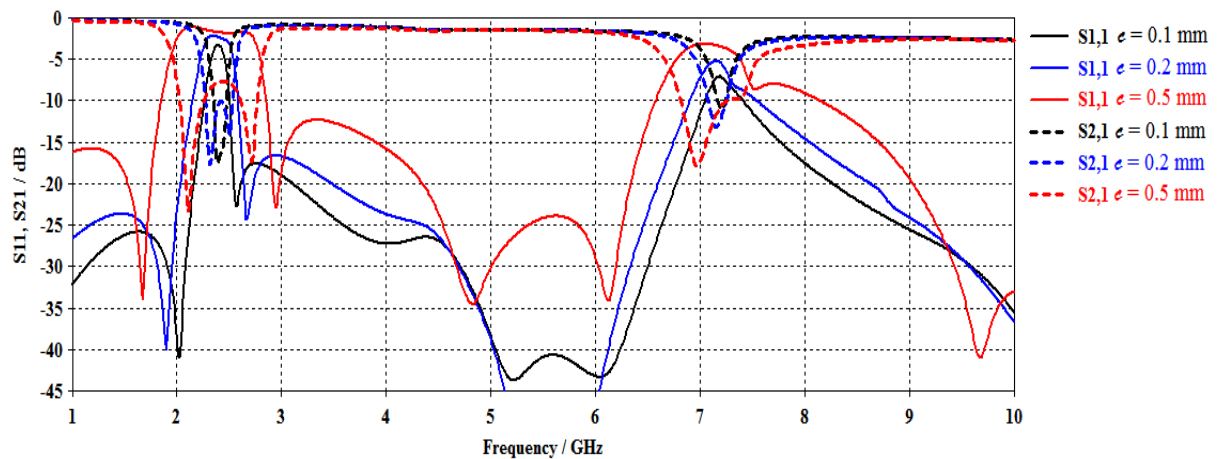


Fig. 3.19 Transfer characteristics of the filter with two interlaced U-slot's for various slot widths ϵ for ($\ell = 18.3\text{mm}$, $d = 1.2\text{mm}$).

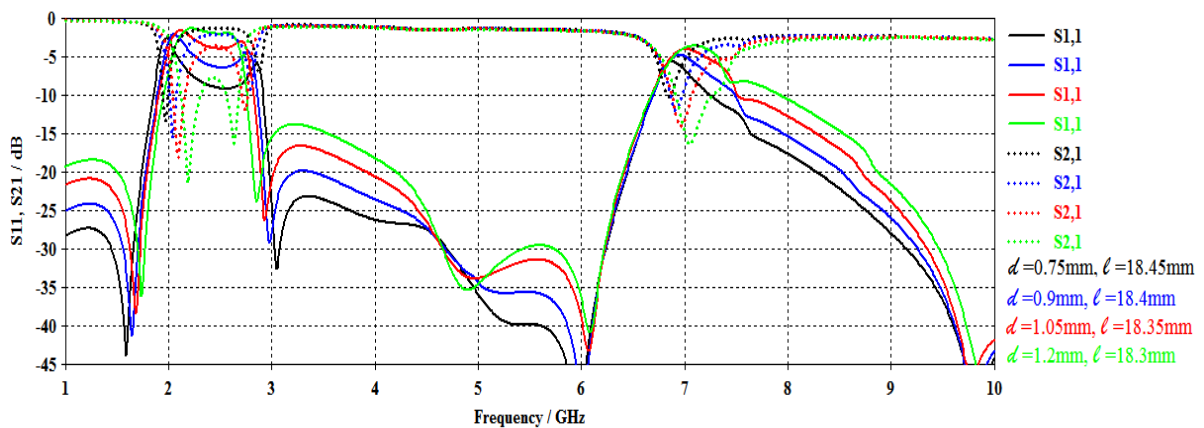


Fig. 3.20 Transfer characteristics of the filter with two interlaced U-slot's for various distances between two slots d ($\epsilon = 0.4\text{mm}$).

Figures 3.21 and 3.22 compare the obtained performance of the three filters using two slots with that for the single slot design for fixed values of $\ell = 18.2\text{mm}$, $\epsilon = 0.4\text{mm}$ and $d = 1\text{mm}$. Details of the compared parameters are listed in Table 3.1. The use of the two interlaced slots has offered sharper and wider reject-band. Moreover, better insertion loss and better matching can be achieved by using the interlaced slots.

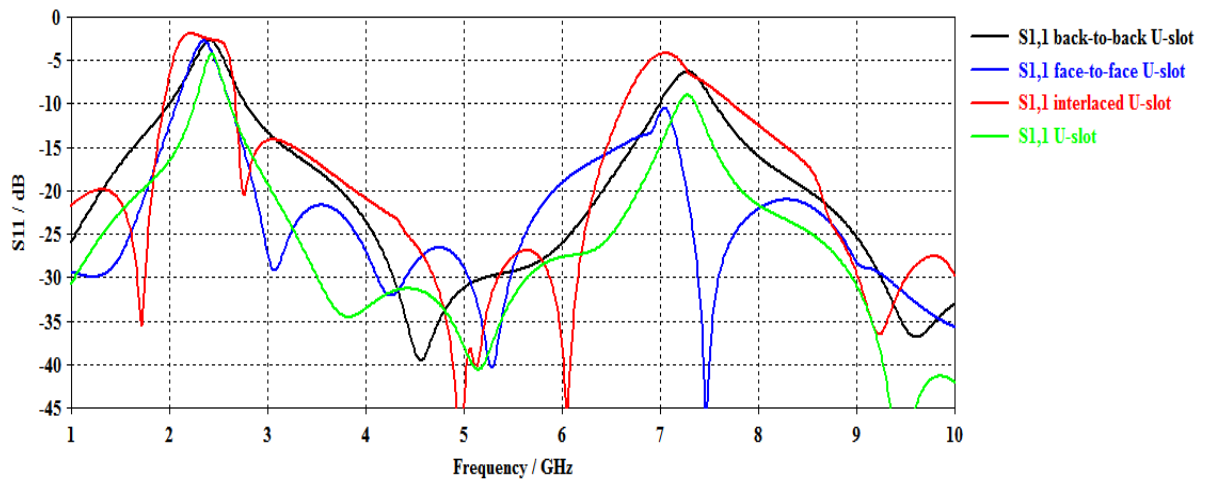


Fig. 3.21 Comparison of the filter reflection coefficient S_{11} for a single slot, 2-slots face-face, 2-slots back-back, and interlaced slots.

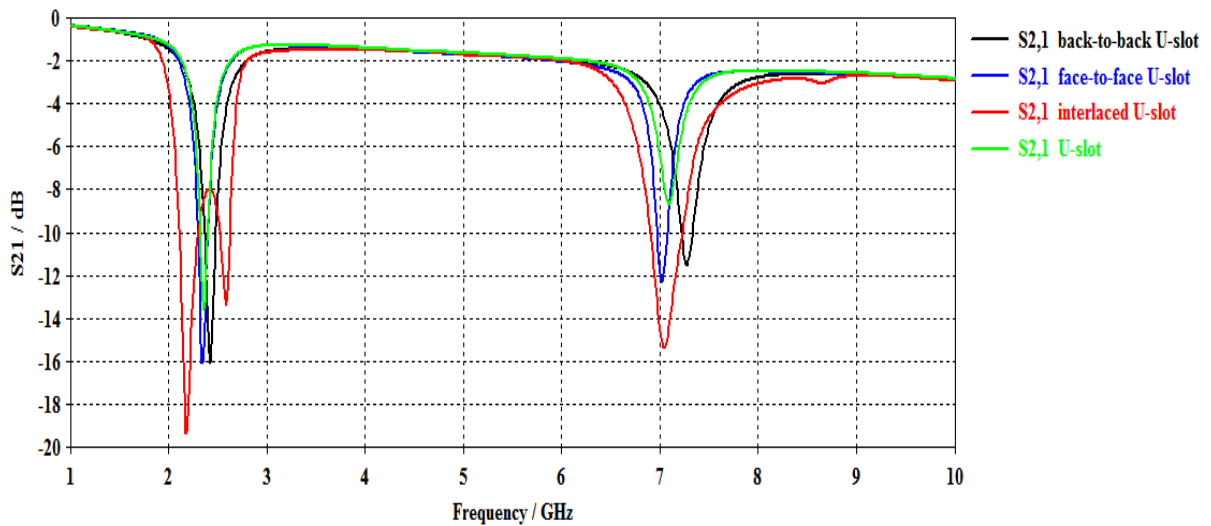


Fig. 3.22 Comparison of the filter transmission coefficient S_{21} plots for a single slot, 2-slots face-face, 2-slots back-back, and interlaced slots.

Table 3.1 Frequency response characteristics of different designs of the filter with various configurations of the U-shaped slot.

Slot type	First resonance				Second resonance			
	S_{11}	BW% 3dB/10dB	S_{21}	BW% 3dB/10dB B	S_{11}	BW% 3dB/10dB B	S_{21}	BW% 3dB/10dB B
single slot	-4.34	9.2/29.3	-13.53	3.3/17.6	-9	5/12.8	-8.64	4.1/--
2-slots face-face	-2.78	12.8/29.7	-16.07	2.7/9.5	-10.4	3.1/19.6	-12.23	1.7/--
2-slots back-back	-2.75	17.6/48.5	-16.04	3/9.2	-6.31	7.8/19.7	-11.48	2.8/--
interlaced slots	-1.7	24.5/33.4	-8.04	2.5/22.4	-4.2	7.8/22.2	-15.32	3.3/9.5

3.4 Explanation of the Bandstop Behavior of the Filters

The presented effects of the band mismatch and band reject can be both explained as the result of resonance in the U-slot. This resonance is exhibited as a parallel LC circuit that is connected in series to the microstrip line. At resonance, the high impedance of the LC circuit forms a mismatch that is seen as an increase in the reflection coefficient S_{11} and reduction in the transmission coefficient S_{21} . An alternative look is that the piece of the microstrip line with the U-slot/substrate combination forms a metamaterial which produces a transmission line section having an impedance far from the 50 Ohm. Such impedance appears at certain frequencies and causes the high mismatch seen as an increase in the reflection coefficient S_{11} and reduction in the transfer coefficient S_{21} .

In each of the above two approaches, the reflection coefficient is given by:

$$\Gamma = S_{11} = (Z_L - Z_0) / (Z_L + Z_0) \quad (3.3)$$

Where Z_0 is the characteristic impedance of the microstrip line without the slot, which is designed to be 50Ω , and Z_L is the characteristic impedance of the microstrip line with the slot. The microstrip line width is chosen according to Eq. 3.1-a to obtain an impedance of 50Ω . However, the impedance Z_L varies widely around the resonance frequency resulting in the filter properties.

The equivalent circuit of the single U-slot filter can be represented by the circuit shown in Fig. 3.23. The LC elements account for the resonance of the slot, while the resistance R accounts for the losses in the substrate and copper. The impedance of the microstrip line section containing the slot is thus given by:

$$Z_L = j\omega L / (1 - \omega^2 LC + j\omega L/R) \quad (3.4)$$

The resonance frequency is then $\omega_p = 1/\sqrt{LC}$ and then:

$$Z_L(\omega_0) = R$$

Thus at resonance (stopband frequency), the reflection coefficient will be:

$$\Gamma(\omega_0) = S_{11}(\omega_0) = (R - Z_0) / (Z_L + Z_0) = (R - 50) / (R + 50) \quad (3.5)$$

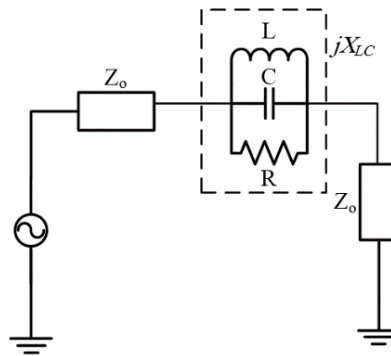


Fig. 3.23 An equivalent circuit representation of the U-slot filter.

3.5 The Effective Permittivity and Permeability of the U-slot

The obtained values of the S parameters from the simulation are used to find the effective permittivity and permeability of the section of the line incorporating the slot following the procedure given in [58]. The obtained results for the single and two slot filters are shown in Figs. 3.24 to 3.27. The changes in the effective permittivity and permeability occur near the resonance frequency of 2.45 GHz. The negative values of the permittivity and the permeability indicate that the slot exhibits a metamaterial behavior. The interlaced slots have the highest changes. It can be noted here that the size of the folded (U-shaped) slot is slightly smaller than $1/4$ the effective wavelength, and the separation between the slot legs is about 1-3% of the effective wavelength. At such dimensions in terms of the wavelength and the existence of abrupt changes (from conductor to vacuum), metamaterial effects appear.

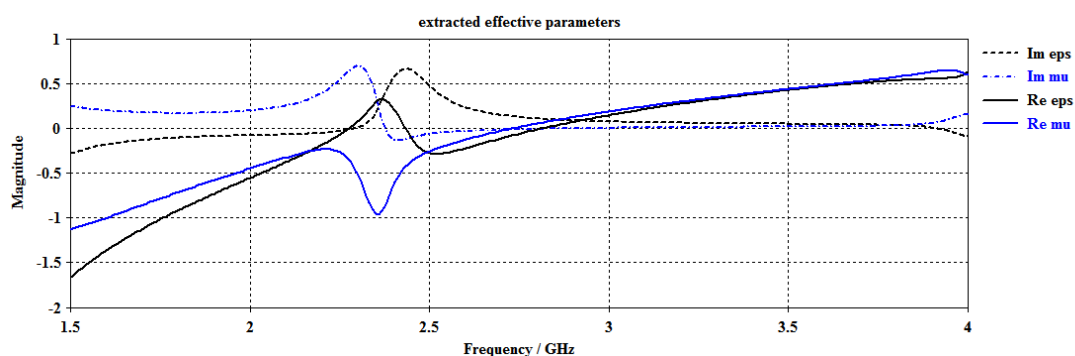


Fig. 3.24 Extracted real and imaginary parts of the effective parameter of the single U slot ($\ell = 18.2$ mm, $d = 1.0$ mm, $e = 0.5$ mm). The solid line represents the real part, while the dashed line represents the imaginary part.

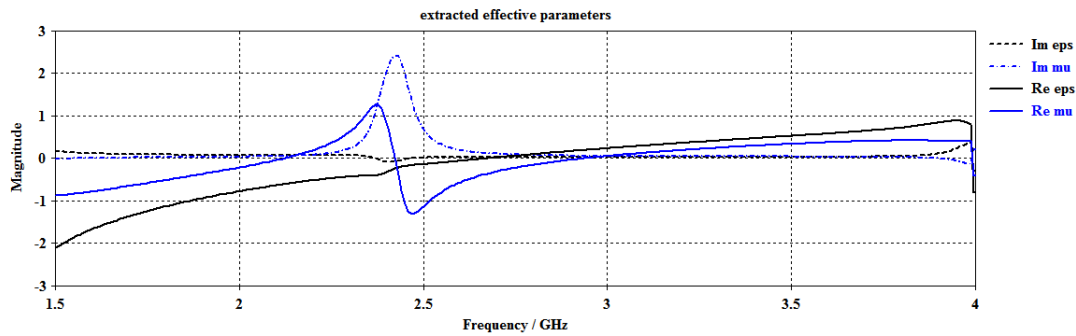


Fig. 3.25 Extracted effective electric permittivity and magnetic permeability of two back-to-back U-slots ($\ell = 18.2$ mm, $d = 1.0$ mm, $e = 0.5$ mm, $w = 1$ mm). The solid line represents the real part, while the dashed line represents the imaginary part.

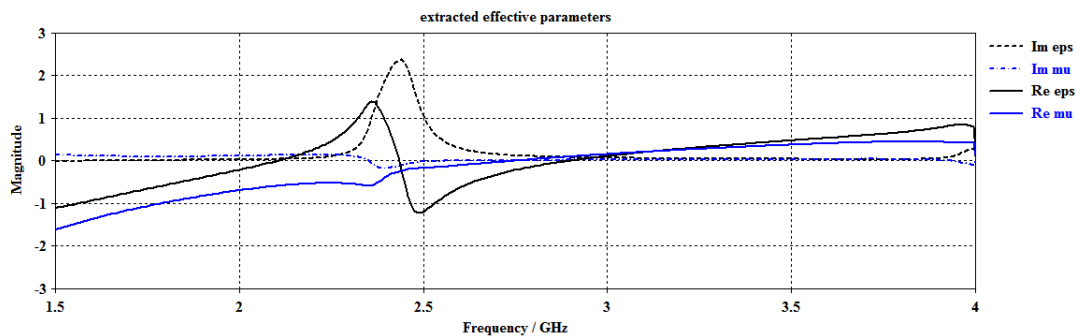


Fig. 3.26 Extracted effective electric permittivity and magnetic permeability of two face-face U-slots ($\ell = 18.2$ mm, $d = 1.0$ mm, $e = 0.5$ mm, $t = 1$ mm). The solid line represents the real part, while the dashed line represents the imaginary part.

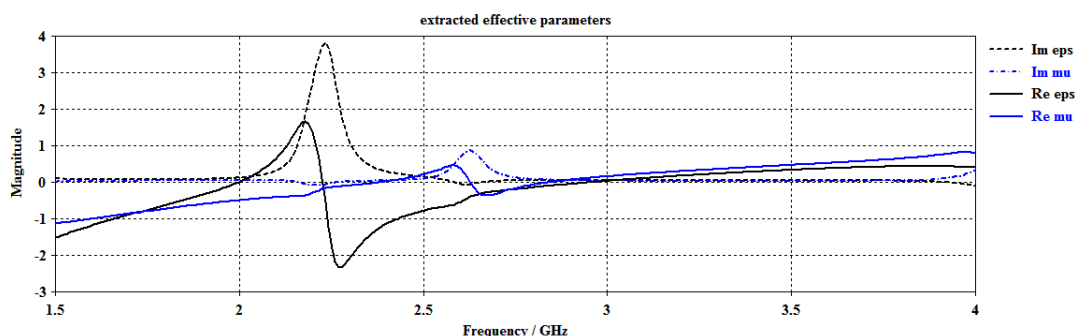


Fig. 3.27 Extracted real and imaginary parts of the effective parameter of interlaced U slots ($\ell = 18.3$ mm, $d = 1.2$ mm, $e = 0.4$ mm, $t = 1$ mm). The solid line represents the real part, while the dashed line represents the imaginary part.

3.6 The Design with Thicker Substrate

Another design is made using a thicker FR4 substrate of 3.2mm in an attempt to achieve easier fabrication for the interlaced slots as well as better insertion loss. The width of the microstrip line is changed to 6.13mm to achieve 50Ω impedance in accordance with Eqs. 3.1. This larger width of the microstrip line, there is more freedom to vary the slot width and the separation between its legs. The obtained performance of the U-shaped slot for the previous configurations is shown in Figs. 3.28 to 3.31. The improvement in the insertion loss is marginal. The improvement in the reflection coefficient at the reject-band is minimal, and it is more significant for the interlaced slots.

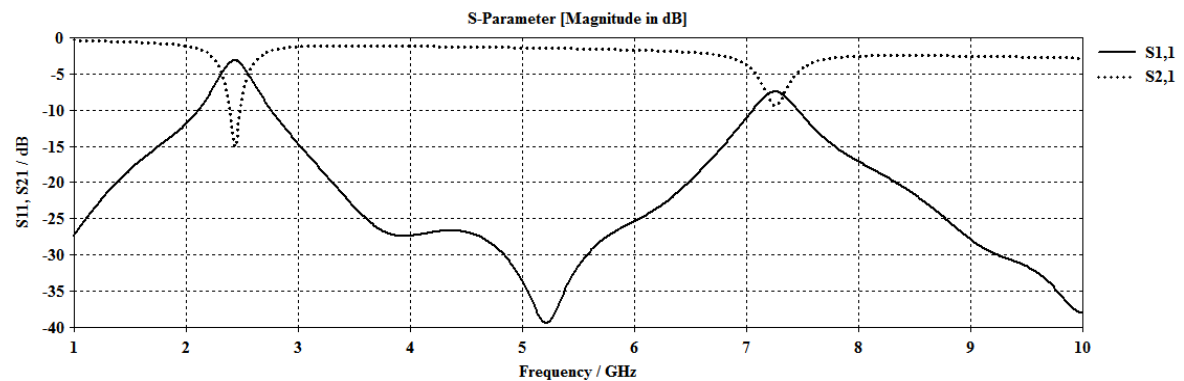


Fig. 3.28 Transfer characteristics of resized U-slot filter ($\ell=17.45\text{mm}$, $d=2.5$, mm, $\epsilon=0.7\text{mm}$).

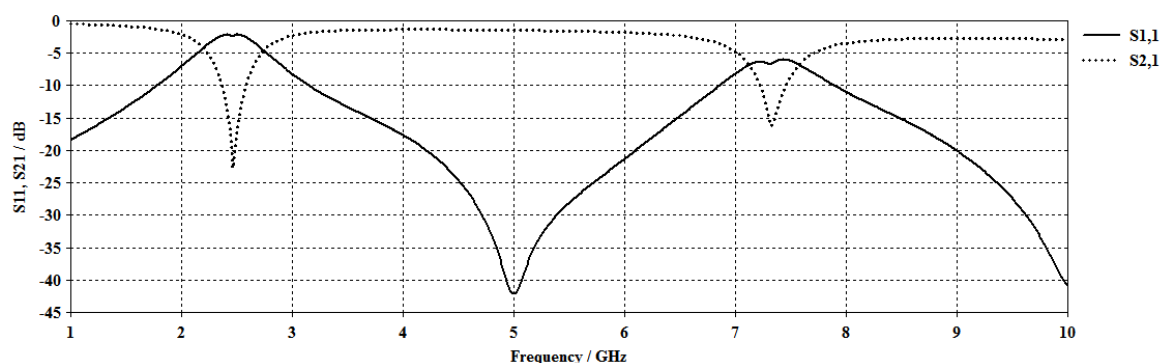


Fig. 3.29 Transfer characteristics of the resized filter with two back-to-back U-slot's ($\ell=17.45\text{mm}$, $\epsilon=0.7\text{mm}$, $d=2.5$ mm and separation between two slots 1mm).

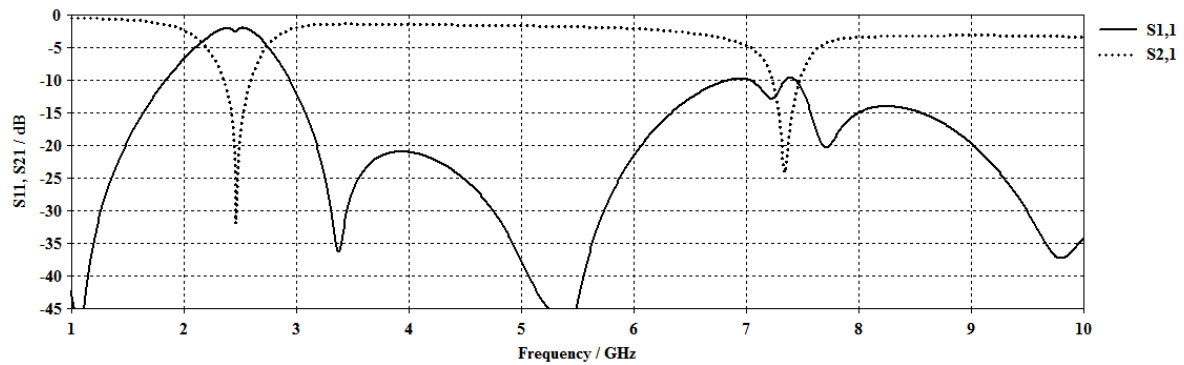


Fig. 3.30 Transfer characteristics of the resized filter with two vis-à-vis U-slot's ($\ell = 17.45\text{mm}$, $e = 0.7\text{mm}$, $d = 2.5\text{ mm}$ and separation between two slot's 1mm).

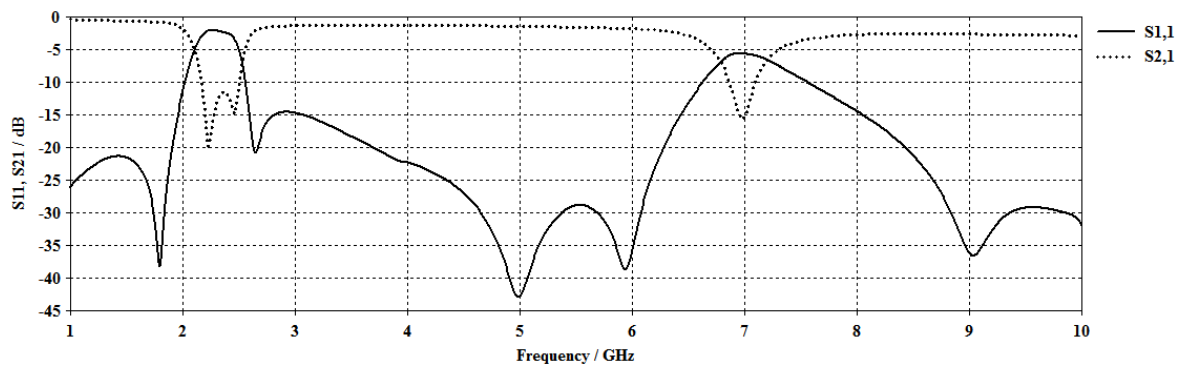


Fig. 3.31 Transfer characteristics of the resized filter with two interlaced U-slot's ($\ell = 17.85\text{mm}$, $e = 0.6\text{mm}$, $d = 2.55\text{mm}$ and separation between two slot's 2mm).

3.7 The Effect of the Loss Tangent of the Substrate

The effects of the loss tangent of the substrate on the insertion loss are demonstrated in the Figs. 3.32 to 3.35. The used value of the loss tangent for the FR4 is 0.025. In the results shown the Figs. 3.32 to 3.35, the loss tangent is assumed as 0.0025 to represent a low-loss substrate. The figures show noticeable improvement in the reflection coefficient across the reject-band. Better enhancement in the insertion loss across the pass-band is evident from the figures. Referring to Eq.3.4, it is obvious that a substrate with a lower loss factor means a higher value of the parallel resistor R leads to reflection coefficient values closer to unity or closer to zero dB. Consequently, a higher

reflection coefficient results in a lower transmission coefficient, which means a larger insertion loss at the stopband. Table 3.2 lists the values of the reflection coefficient and insertion loss for the four proposed filters for the two substrates.

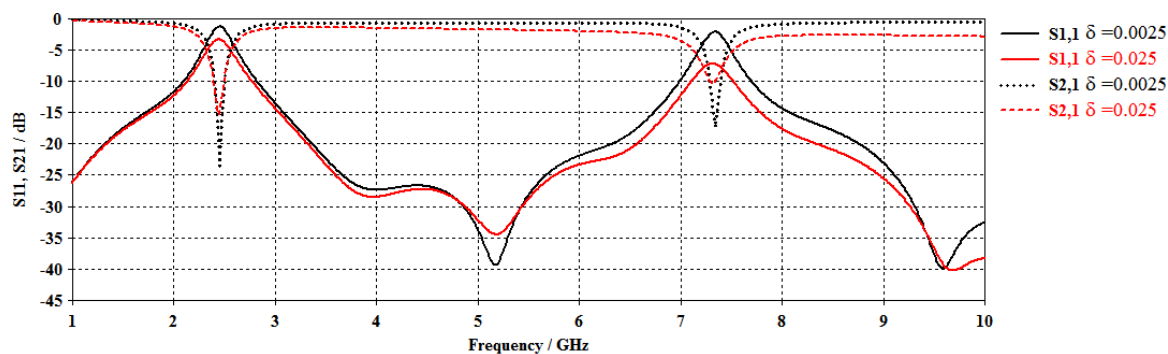


Fig. 3.32 Transfer characteristics of the U-slot filter for tangent loss equal to 0.0025; ($\ell=18.2\text{mm}$, $e=0.5\text{mm}$, $d=1.0\text{mm}$).

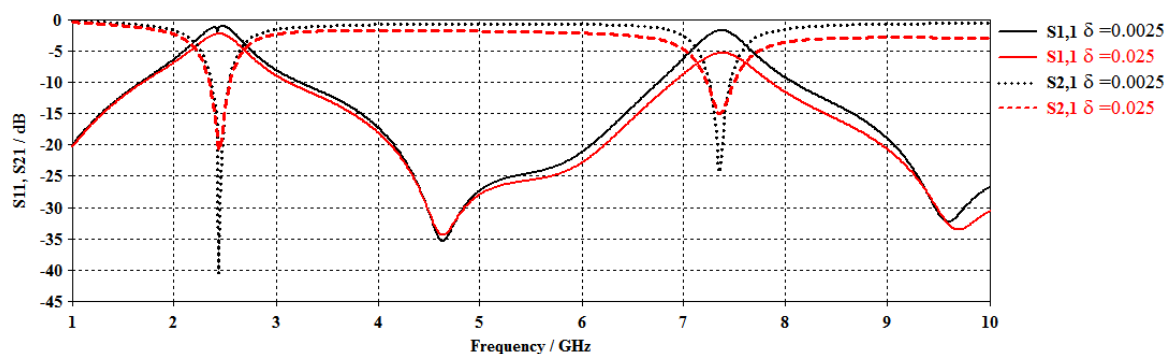


Fig. 3.33 Transfer characteristics of filter with two back to back U-slot's for tangent loss equal to 0.0025; ($\ell=18.2\text{mm}$, $d=1.0\text{mm}$, $e=0.5\text{mm}$, $w=1\text{mm}$).

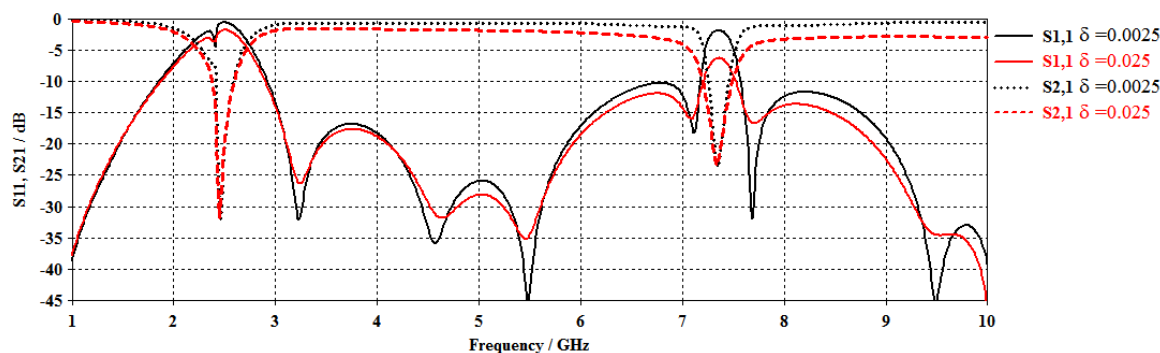


Fig. 3.34 Transfer characteristics of filter with two vis-à-vis U-slot's for tangent loss equal to 0.0025; ($\ell=18.2\text{mm}$, $d=1.0\text{mm}$, $e=0.5\text{mm}$, $t=1\text{mm}$).

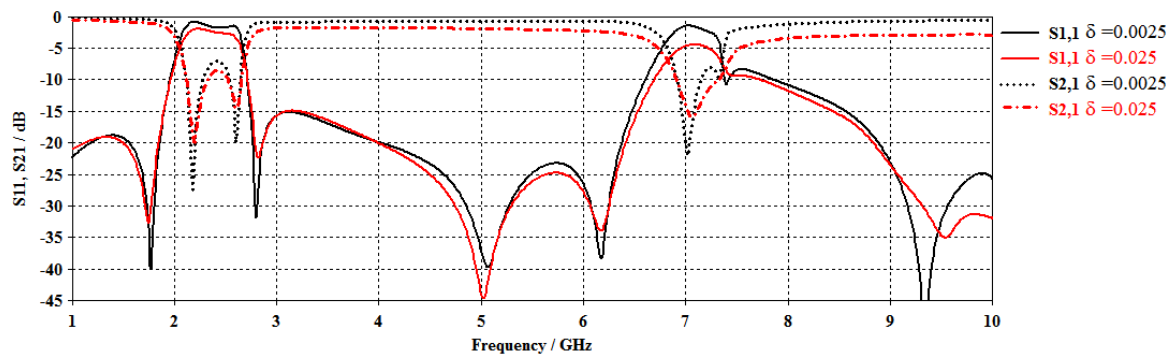


Fig. 3.35. Transfer characteristics of filter with two interlaced U-slots for tangent loss equal to 0.0025 ($\ell = 18.3$ mm, $d = 1.2$ mm, $e = 0.4$ mm, $w = 1$ mm).

Table 3.2 Comparison of the S_{11} and S_{21} parameters for the two substrates

	1 st resonance		2 nd resonance		
U-slot	S_{11}	S_{21}	S_{11}	S_{21}	$S_{21}@4\text{GHz}$
$\tan\delta=0.025$	-1.19	-15.53	-1.90	-10.27	-1.55
$\tan\delta=0.0025$	-1.31	-23.39	-2.09	-17.37	-0.67
face-face	S_{11}	S_{21}	S_{11}	S_{21}	$S_{21}@4\text{GHz}$
$\tan\delta=0.025$	-2.06	-30.81	-6.34	-23.26	-1.69
$\tan\delta=0.0025$	-0.68	-32.12	-1.92	-17.37	-0.74
back-back	S_{11}	S_{21}	S_{11}	S_{21}	$S_{21}@4\text{GHz}$
$\tan\delta=0.025$	-2.30	-20.74	-5.34	-14.98	-1.71
$\tan\delta=0.0025$	-1.31	-40.50	-1.71	-24.48	-0.81
interlaced	S_{11}	S_{21}	S_{11}	S_{21}	$S_{21}@4\text{GHz}$
$\tan\delta=0.025$	-2.56	-8.51	-4.42	-15.78	-1.70
$\tan\delta=0.0025$	-1.80	-7.02	-1.43	-21.87	-0.76

3.8 The Electric Field Distribution on the Slot

For a better insight into the effect of the U-slot on the propagation properties of the microstrip line that has been utilized in this chapter for the design of four bandstop filters, the electric field distribution along the slot is studied. Figure 3.36 shows the electric field distribution in the single U-slot at the frequencies of the reject band 2.45GHz and the pass band 4GHz. The E-field vectors inside the two legs of the slot are in opposite directions, and the field is maximum at the center of the slot and tends to zero at both ends. This represents a $\frac{1}{2}$ effective wavelength, and the field opposition comes from the folding of the slot. At the 4GHz frequency, the E-field extends towards the edges of the microstrip line, and it is still in opposite directions on both legs of the slot. These results show that the slot will have a small effect on any radiation from the line since the E-field effects are canceled because they are in opposite directions.

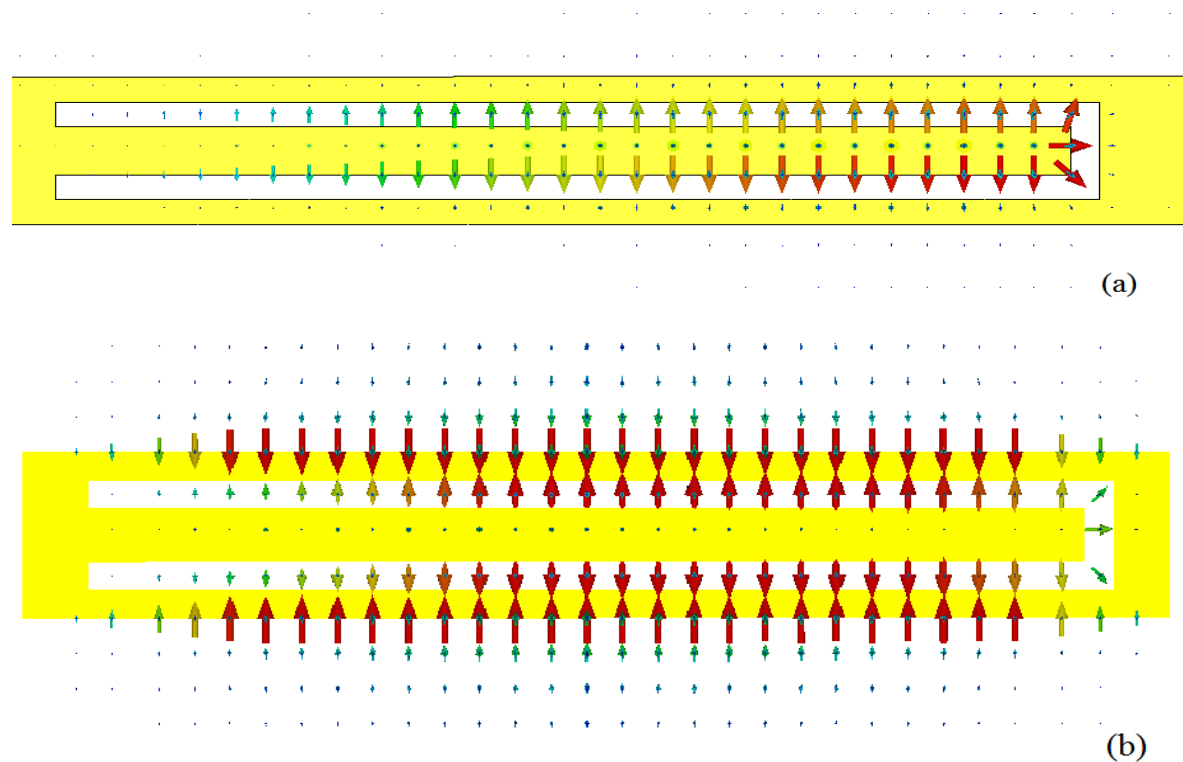


Fig. 3.36 Simulated E-field distribution inside the single slot. (a) at 2.5GHz. (b) at 4GHz.

Figure 3.37 shows the electric field distribution in the two adjacent slots of the face to face configuration at the frequencies of 2.45GHz and 4GHz. As the magnitude of the field tends to zero at the tips of the slots, then the mutual coupling between the two slots in this configuration is minimal. At 2.45GHz where the slots are in resonance, the field density at the right slot is higher since the slot is fed from the right side of the microstrip line, and thus a large fraction of the wave is reflected to the right side leading to less power incident at the left slot. At 4GHz pass band, the two slots are not in resonance, and there is a small reflection at the slot. Therefore, the E-field density at the two slots is almost equal.

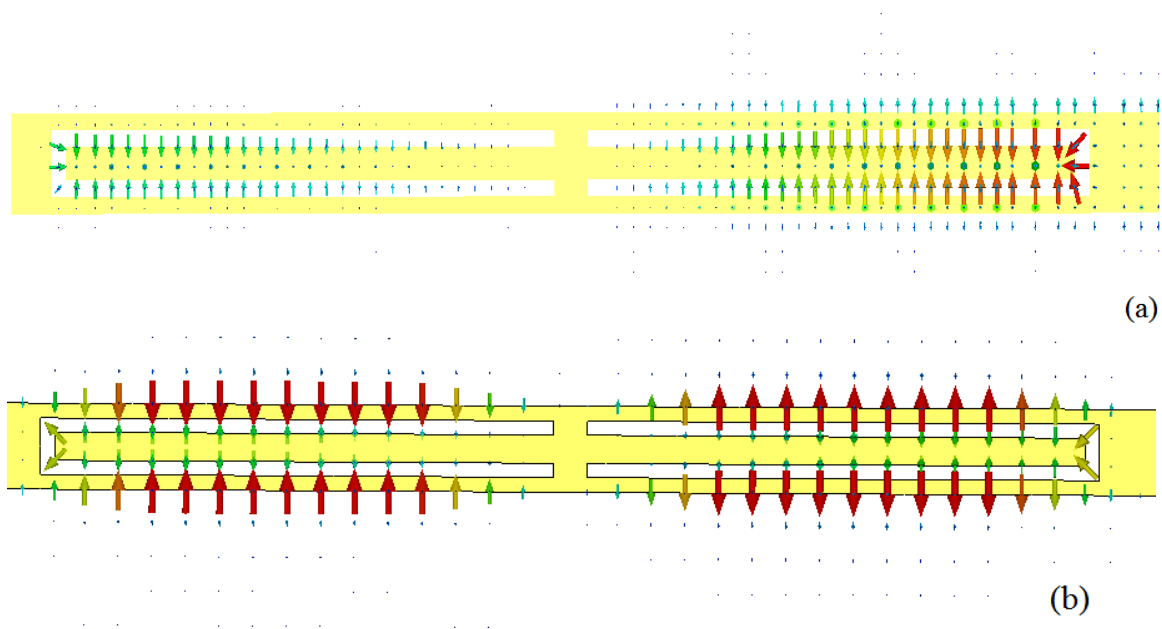


Fig. 3.37 Simulated E-field distribution inside the two slots facing each-other. (a) at 2.5GHz. (b) at 4GHz.

Figure 3.38 shows the electric field distribution in the back-back slot configuration. It can be noted that the field magnitude is maximum at the region between the two slots and thus the coupling, in this case, is larger than that for the face-face arrangement. It is also noted that the field is in opposite directions along the two legs of each slot.

Figure 3.39 shows the electric field distribution in the two interlaced slots. The effect of interlacing the two slots means a very close proximity of

the four legs of the two slots, which leads to a higher mutual coupling between the two U-slots. At the frequency of 2.45GHz, a higher density of the E-field is noticed at the right slot as the incident wave is applied at the right side of the microstrip line. However, at a 4GHz frequency, the E-field density is more uniform along with the slots as the slots are not resonating, and there is a minimal reflection.

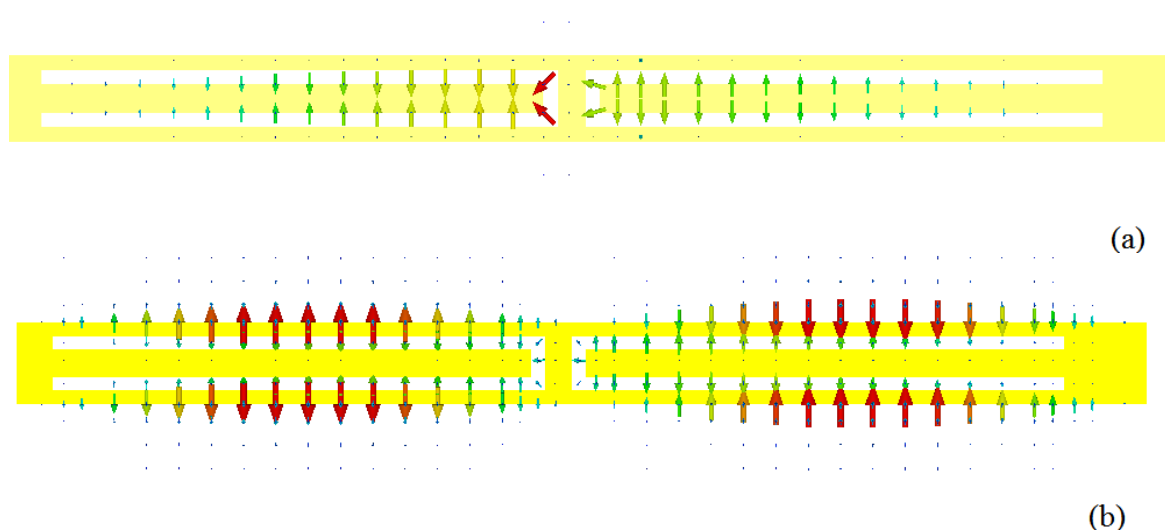


Fig. 3.38 Simulated E-field distribution in the back-to-back U-slots. (a) at 2.5GHz. (b) at 4GHz.

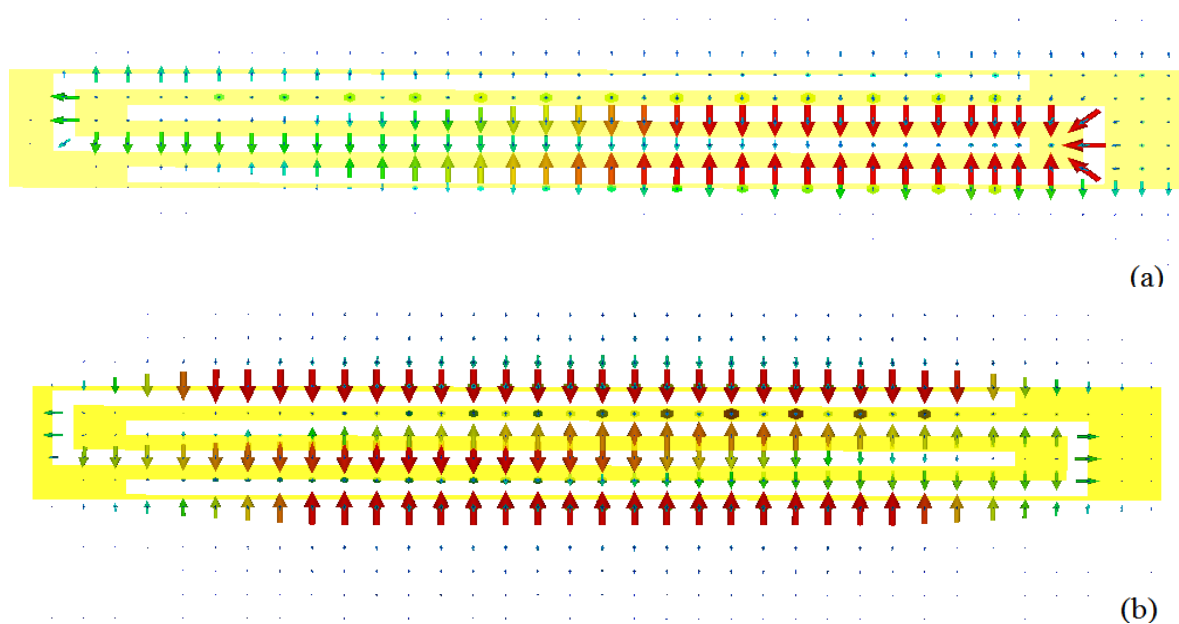


Fig. 3.39 Simulated E-field distribution inside the two interlaced U-slots. (a) at 2.5GHz. (b) at 4GHz.

3.9 The Radiated Field from the Slots

The radiation from the microstrip line before and after the insertion of the slots is investigated to explore if the slots cause any radiation and to obtain deeper insight regarding their operation. Figure 3.40 shows a 3-D display of the simulated gain of the microstrip line (with no slots) at 2.45GHz and 4GHz, which represents the reject and pass bands respectively. In this and the following simulations, a source is applied to one port of the line while the other port is connected to a matched load. The figure shows that there is radiation in the normal direction to the substrate. The line length is 60 mm, which is about 0.49 the wavelength in the air at the 2.45GHz frequency, while it is about 0.89 the wavelength in the air at the frequency of 4GHz. The radiation shape of a mainbeam, two nulls, and two side lobes can be attributed to a line radiator of less than one wavelength extension. However, this radiation is very small as the gain is -15.66 dB, and the total efficiency is -24.32 dB (0.37%) at 2.45GHz frequency. The corresponding values at the 4 GHz frequency are -11.34 dB and -20.95 dB (0.8%) respectively. The increase in the very small gain and total efficiency at 4 GHz can be related to the increased length of the line in terms of the wavelength. The small values of the gain are due to the small values of the total efficiency. This proves that the radiation from the microstrip line is minimal. These are known facts, but they are noted here for the sake of comparison with the cases when the slots are used in the filter design.

The radiated field, when there is a single slot in the microstrip line, is demonstrated in Fig. 3.41 for both frequencies of 2.45GHz and 4 GHz. The patterns are similar in shape to the corresponding ones without the slot (see Fig. 3.40). At the 2.45GHz frequency, the maximum gain value has increased from -15.7 to -8.73 dB, indicating the effect of introducing the slot on the already small values of the gain and total efficiency. However, the gain at 4GHz frequency has only increased by 0.48 dB. This can be attributed to the fact that at the reject band, the E-field is concentrated while at other frequencies, it is not, as can be seen from Fig. 3.36. Since the E-field vectors

along the two legs of the slot are in opposite directions, their contributions to the radiation cancel out. The values of the total efficiency are still very small at (0.59%) and (0.84%) at the frequency of 2.45GHz and 4GHz, respectively.

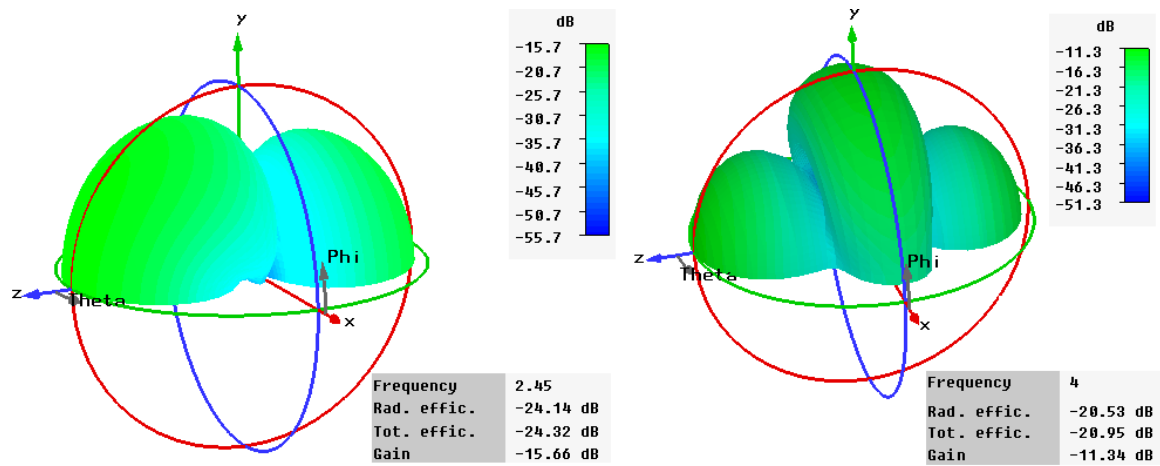


Fig. 3.40 Radiation pattern of the microstrip line without any slot at; (a) 2.45 GHz, and (b) at 4 GHz frequency.

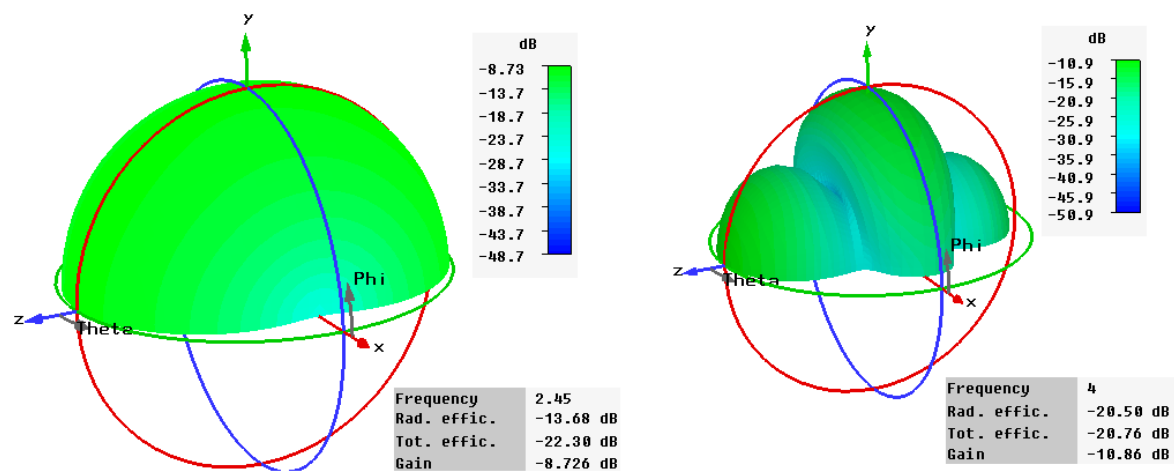


Fig. 3.41 Radiation pattern of the filter with the U-slot at; (a) 2.45 GHz, and (b) at 4 GHz frequency. ; ($\ell = 18.2\text{mm}$, $d = 1.0\text{mm}$, $e = 0.5\text{mm}$).

Figure 3.42 shows the radiated field when there are two back-back slots in the microstrip line at both frequencies of 2.45GHz and 4 GHz. The patterns are similar in the general shape to those shown in Fig. 3.41. At 4 GHz, the maximum gain values are slightly higher (by about 0.82 dB) than those of the case without the slots indicating that the effect of introducing the slots is very little on the already small values of the gain and total efficiency. This can be attributed to the fact that the E-field along the two legs of the slot are in

opposite directions and thus their small contributions to the radiation cancel out. However, at the reject-band frequency of 2.45GHz, the maximum gain is at -5.83dB, which is slightly higher than that of the case before introducing the slots. This can be attributed to the fact that at the reject band, the E-field at the fold of each of the back-back slots is in the same direction as it is clear in Fig. 3.38-a. Thus, this part of the field at the center of the microstrip line has caused some radiation that leads to an increase in the maximum gain as compared with the case without the slot. The values of the total efficiency are still very small at (1.6%) and (0.76%) at the frequency of 2.45GHz and 4GHz respectively.

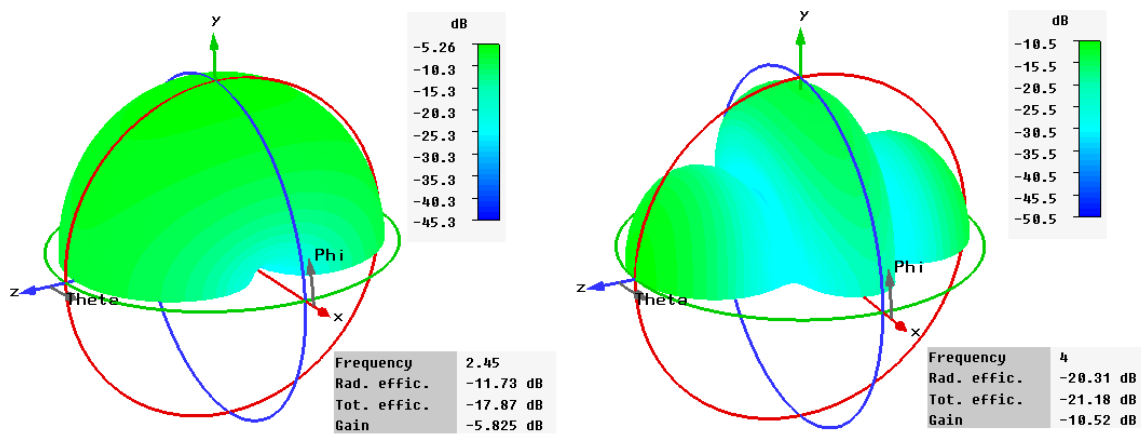


Fig. 3.42 Radiation pattern of the filter with the two back-back slots at; (a) 2.45 GHz, and (b) at 4 GHz frequency. ($\ell=18.2\text{mm}$, $d=1.0\text{mm}$, $e=0.5\text{mm}$, $w=1\text{mm}$).

Figure 3.43 shows the radiated field when the two slots are placed in a face-face configuration at both frequencies of 2.45GHz and 4 GHz. The gain at 2.45 GHz is -10.9 dB (4.8 dB above the case with no slots), while at the 4GHz frequency the gain is almost the same as that without slots. The reason for that is, at the reject band, the E-field inside the fold of the two slots is in opposite directions (note both sides of Fig. 3.37-a), and thus their contributions to the radiation cancel out. The values of the total efficiency are still very small at (0.26%) and (0.83%) at the frequency of 2.45GHz and 4GHz, respectively.

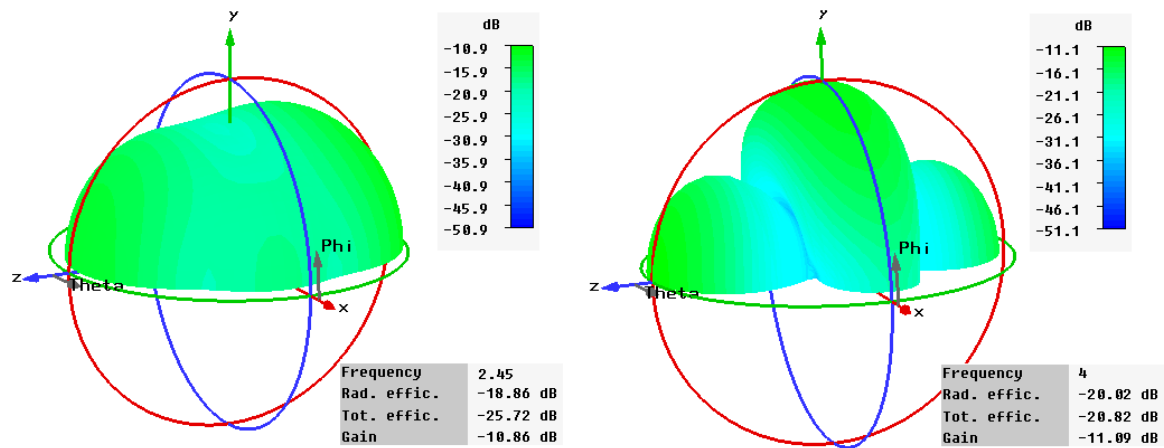


Fig. 3.43 Radiation pattern of the microstrip line with the two face-face slots at (a) 2.45 GHz, and (b) at 4 GHz frequency. ;($\ell = 18.2\text{mm}$, $d = 1.0\text{mm}$, $e = 0.5\text{mm}$, $t = 1\text{mm}$).

The results for the last configuration of the interlaced slots are shown in Fig. 3.44. The maximum radiation is generally normal to the substrate, where the field is concentrated on the two interlaced slots (see Fig. 3.39). At the reject-band of 2.45GHz, the maximum gain is at -7.8dB, which is although small but higher than that without the slots. The E-field in the two legs of each slot is in the opposite direction then the radiated wave is small. This fact is more pronounced at the passband of 4GHz, where the gain has a small value of -10.65dB, and the total efficiency is also very small (-20.79dB, or 0.83%). It is noted here that the maximum gain is -10.65dB which is slightly larger (by about 0.7 dB) than that for the case without a slot. Moreover, it is slightly higher than that for the cases where the two slots are not interlaced. This can be attributed to the very close proximity of the four legs of the two interlaced slots and the resulting mutual coupling between them. As an overall evaluation, it can be concluded from the results shown in Figs 3.40 to 3.44 that the introduction of the slots in the microstrip line has a slight increase in the maximum gain. This can be attributed to the folded shape of the slots, which makes the E-field in the two legs in the opposite direction leading to cancellation in the far-field. The increase in the gain (larger radiation) occurs at the reject-band, which is of little significance as this signal is undesirable.

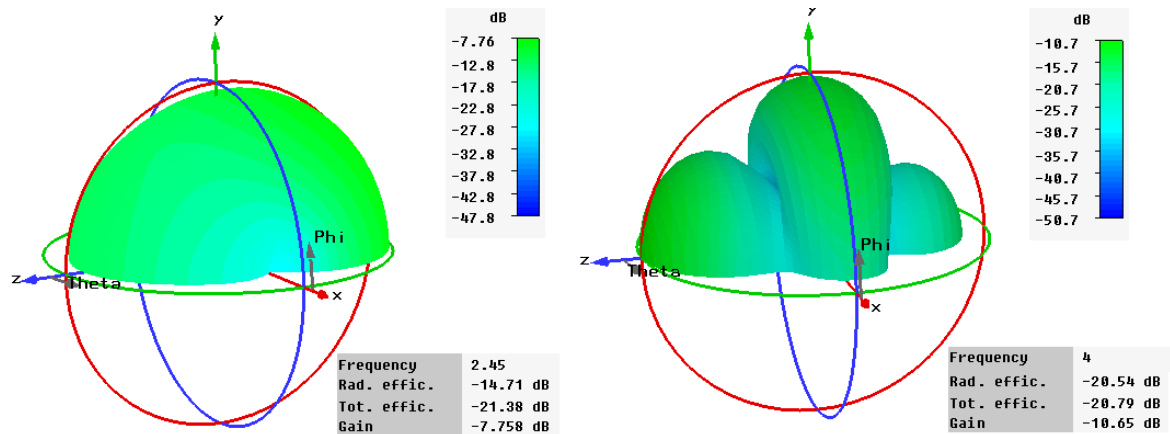


Fig. 3.44 Radiation pattern of the filter with the two interlaced slots at (a) 2.45 GHz, and (b) at 4 GHz frequency. ($\ell=18.3$ mm, $d=1.2$ mm, $e=0.4$ mm, $h=1$ mm).

At the pass-band, the increase in the gain is within 1dB. Table 3.3 compares the performance of the investigated cases.

Table 3.3 Radiation pattern characteristics for the four filter designs compared to that of the microstrip line.

Case	Line	Single slot	Face-face	Back-back	interlaced
gain					
2.45 GHz	-15.66	-8.726	-10.86	-5.825	-7.758
4 GHz	-11.34	-10.86	-11.09	-10.52	-10.65
Rad. effic.					
2.45 GHz	-24.14	-13.68	-18.86	-11.73	-14.71
4 GHz	-20.53	-20.50	-20.02	-20.31	-20.54
Tot. effic.					
2.45 GHz	-24.32	-22.30	-25.72	-17.87	-21.38
4 GHz	-20.95	-20.76	-20.82	-21.18	-20.65

3.10 Experimental Assessment of the Proposed Filters

For the verification of the proposed filters, three microstrip circuits are fabricated as shown in Fig.3.45. The prototypes are a 50 Ω microstrip transmission line, a single U-slot filter, and a filter with two interlaced U-slots. The used substrate is FR4 of thickness 1.6mm and loss tangent of 0.025 as that used in the simulations. A vector network analyzer model Rode, and Schwarz ZVL13 are used for the measurement of the scattering parameters of the three fabricated prototypes. In the measurements, the two ports of the tested prototype are connected to the two ports of the network analyzer.



Fig. 3.45 Photographs of the fabricated prototypes; (a) the filter with the interlaced U-slots, (b) the transmission line, and (c) the filter with a single U-slot.

Figure 3.46 shows the comparative results between the simulated and measured scattering parameters (S_{11} and S_{12}) of the microstrip line. The figure shows that the measurements agree well with the simulation results for the reflection and transmission coefficients. The reflection at the input is much below -10dB indicating good matching, and in spite of the increasing frequency, it remains below -10dB up to the 8 GHz frequency. The transmission coefficient is just below 0dB and slowly decreasing as the

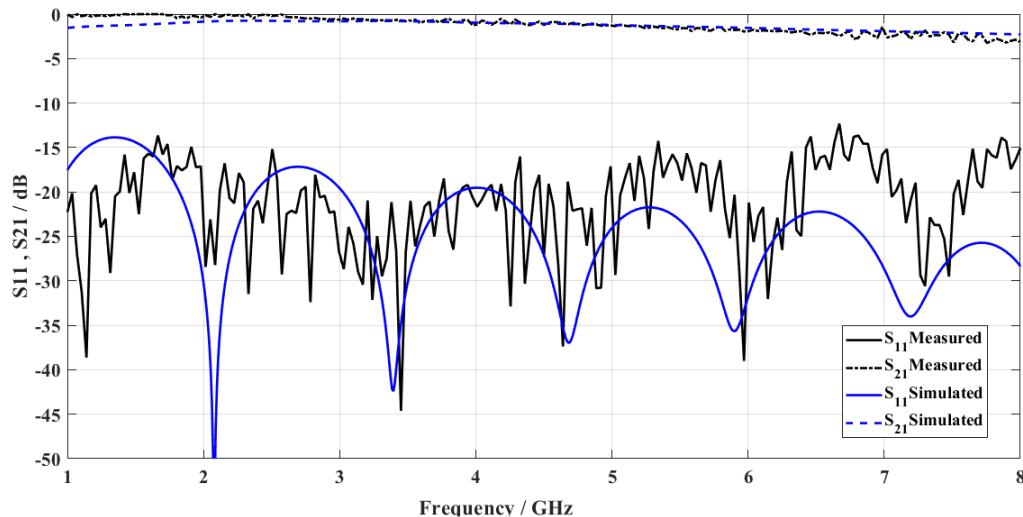


Fig. 3.46 Comparative results between simulation and measurement S-parameters of the fabricated microstrip line with no slot.

frequency increases. This is attributed to the increased losses in the substrate with frequency.

Figure 3.47 shows the comparative results between the simulation and measurement of the fabricated single U-slot microstrip line filter. It is shown that the fabricated filter rejects the signals at the frequency of 2.45GHz and 7.5 GHz with more than 10dB suppression, as it is found in the simulations with small deviation in the bandwidth of the measured result due to the inaccuracy of the U slot in fabrication. The two bands are indicated by a small transmission coefficient of less than -18dB and less than -15dB at the lower and upper stopbands respectively. The reflection coefficients at the two bands are -3dB and -6dB.

The simulated and measured responses of the filter with the two interlaced slots are shown in Fig. 3.48. The figure clearly shows that the stopbands are wider than those obtained from the filter with the single U-slot. The transmission coefficient at the two stopbands are better than -10dB and lower than -15dB, respectively. The reflection coefficients are at -3dB and -5dB. The measured value exhibits a slight shift in the resonances compared

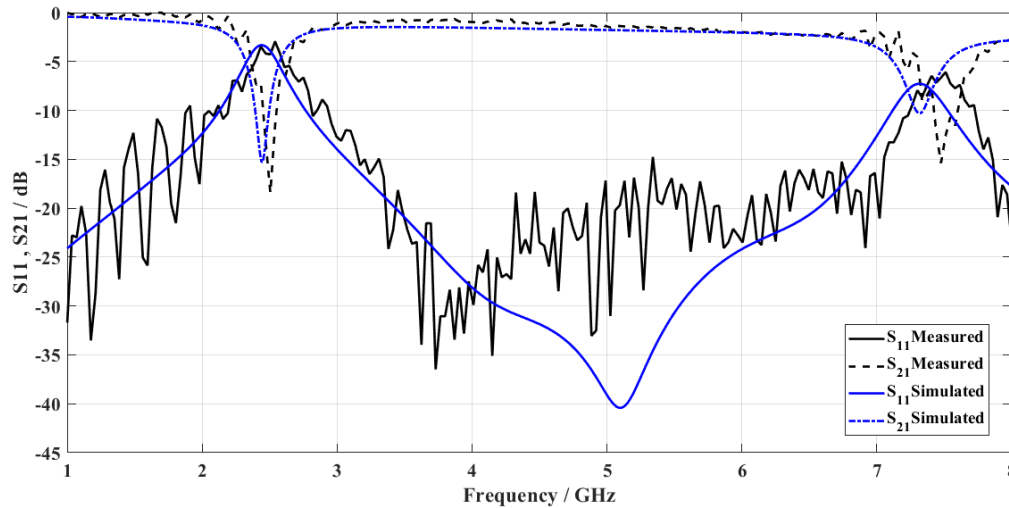


Fig. 3.47 Comparative results between simulation and measurement S-parameters of the fabricated U-slot filter; ($\ell = 18.2\text{mm}$, $e = 0.5\text{mm}$, $d = 1.0\text{mm}$).

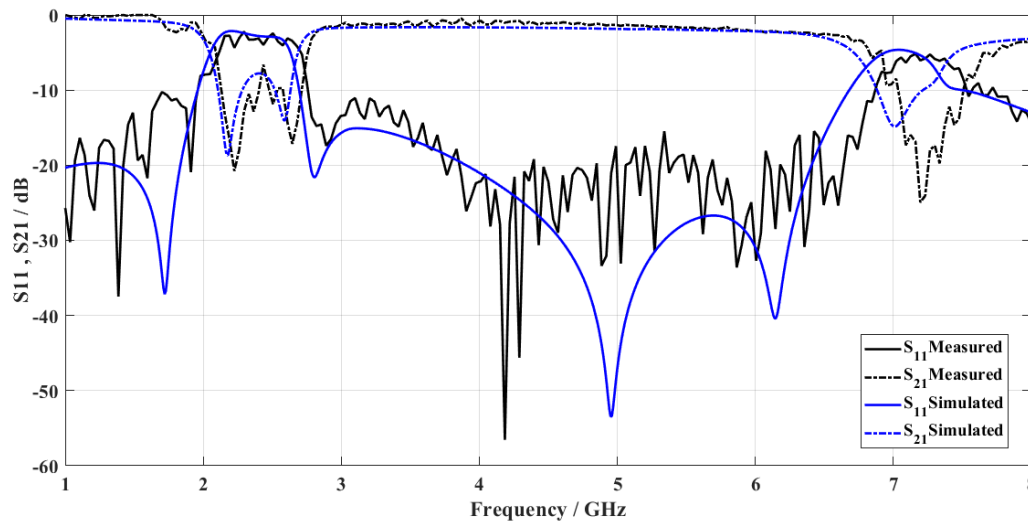


Fig. 48. Comparative results between simulation and measurement S-parameters of the fabricated filter with interlaced U-slot; ($\ell = 1\text{mm}$, $\ell = 18.3\text{mm}$, $d = 1.2\text{mm}$, $e = 0.4\text{mm}$).

with the simulation. This shift can most likely be attributed to fabrication error and connector issues.

Figure 3.49 shows a comparison between the measured reflection coefficients of the transmission line, the U-slot filter, and the filter with the interlaced slots. It can be seen that the use of the two slots has led to a slightly higher reflection in the stopbands. However, across the passband, the reflection coefficients of the three prototypes are basically the same.

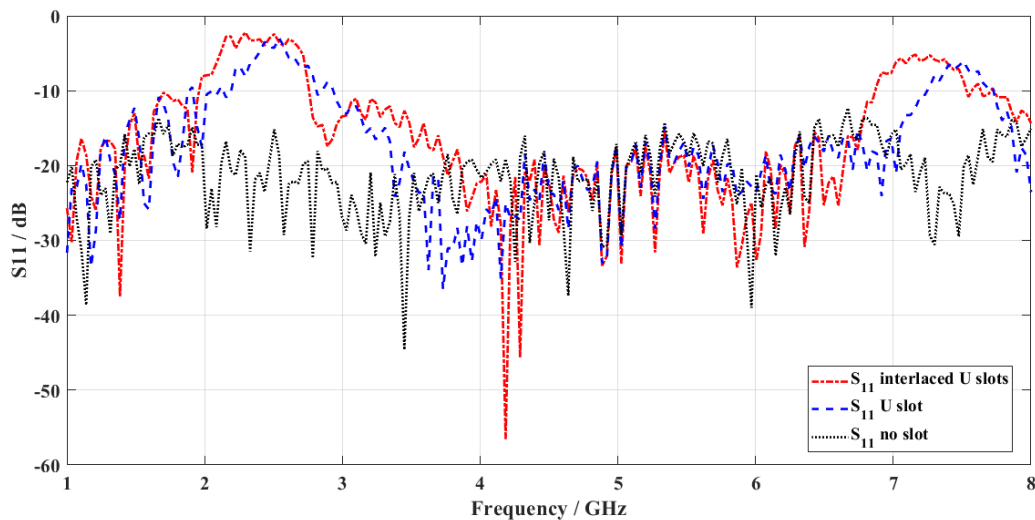


Fig. 3.49 Comparison of measured S_{11} plots for no slot, single slot, and interlaced slots filters.

Figure 3.50 shows a comparison between the measured transmission coefficients of the transmission line, the U-slot filter, and the filter with the interlaced slots. It can be seen that the use of the two slots has resulted in wider and deeper stopbands.

The measured results are in good agreement with those obtained from the simulations, thus verifying the feasibility of the proposed designs.

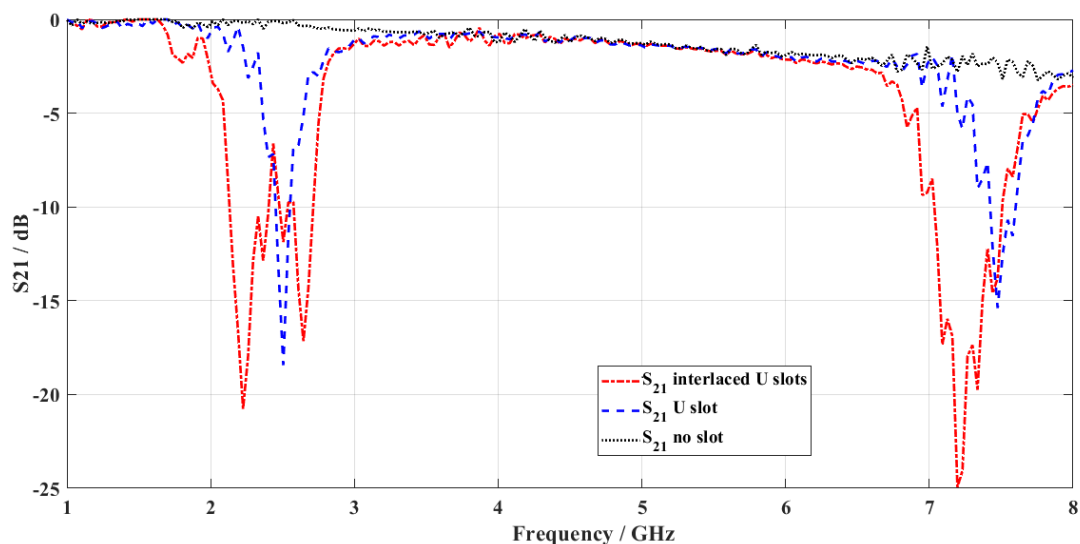


Fig. 3.50 Comparison of measured S_{21} plots for no slot, single slot, and interlaced slots filters.

3.11 Comparison with Other Designs

There are various designs for the microstrip filters which differ vastly in their characteristics and sizes in terms of the wavelength at the operating frequency. The proposed filters in this chapter have a compact size due to the folding of the slot into the U-shape. The resonance of the slot occurs when its overall length is equal to half the guided wavelength at the center of the stopband ($\lambda_g/2$). Due to the folding of the slot into a slim U-shape, the length of the folded slot is about ($\lambda_g/4$). The width of the proposed filter can be five times the width of the slot. At a stopband of the 2.45GHz frequency, the filter dimensions are slightly larger than $18.2 \times 3 \text{ mm}^2$. As for the interlaced two-slots filter, the width of the filter can be ten times the width of the slot, while the length of this filter are slightly longer than that of the single slot filter. The characteristics of the proposed four filters are compared in Table 3.4 with those of other filter designs that are published in the literature. It can be seen that the proposed filters have competitive performance as regards to the size and insertion loss at the stopbands. The relatively lossy FR4 substrate has resulted in slightly higher insertion loss at the passbands.

Table 3.4 Comparison of the characteristics of the proposed filters with other published designs.

Ref.	Band Freq. (GHz)	Dimensions (mm ²)	$\epsilon_r / \tan\delta$	Size ($\lambda_g \times \lambda_g$)	S ₁₁ (dB)	S ₂₁ (dB)	Resonant element
[79]	2/3	40×44	9.9/0.002	0.85×0.92	-0.2	-25	stub
[29]	2.7	55×40	2.2/--	0.73×0.53	-0.2	-23	3 cells
[80]	2.04/6	100×50	2.65/--	1.10×0.55	-0.1	-22	Stub
[81]	7.5	14×14	4.4/0.002	0.73×0.73	0.1	-38.5	1 cell
[82]	3.47	42×20	10.2/0.0023	1.55×0.73	-5	-30	3 U cells
	3.9	42×10	10.2/0.0023	1.75×0.41	-0.1	-23	3 V cells
[83]	2.4/5.27	22×10	4.4/0.02	0.37×0.17	-0.9	-19.05	6 cells
[84]	7.1	35×15	2.65/--	1.34×0.58	-10	-1.4	interdigital
[30]	2.52/7.9	45×30	3.55/0.0027	0.71×0.48	-0.1	-44	2 cells
[85]	1.75	31×35	3.2/0.0012	0.32×0.36	-0.2	-23	1 cell
[26]	7	31×16	2.2/0.0009	1.07×0.55	-0.1	-30	1 cell
	7	50×16	2.2/0.0009	1.73×0.55	-0.1	-59	2 cell
[86]	5.6	18×20	3.38/ 0.0027	0.61×0.69	-0.1	-31	1 cell
	6	27×20	3.38/ 0.0027	0.99×0.74	-0.1	-55	2 cells
	3/5.5/8	35×20	3.38/ 0.0027	0.64×0.38	-0.1	-50	3 cells
U-slot	2.45/7.5	60×20	4.4/0.025	1.02×0.34	-4.34	-13.53	1 cell
Interlaced	2.45/7.5	60×20	4.4/0.025	1.02×0.34	-1.7	-8	2 cells
face-face	2.45/7.5	60×20	4.4/0.025	1.02×0.34	-2.7	-16	2 cells
back-back	2.45/7.5	60×20	4.4/0.025	1.02×0.34	-2.7	-16	2 cells

CHAPTER FOUR

APPLICATION OF THE U- SHAPED GEOMETRY INTO FREQUENCY SELECTIVE SURFACES FSS

CHAPTER FOUR

APPLICATION OF THE U-SHAPED GEOMETRY INTO FREQUENCY SELECTIVE SURFACES FSS

4.1 Introduction

The performance of the U-slot studied in chapter 3 motivates the application of this geometry into Frequency Selective Surfaces (FSS). The U-shaped geometry can be utilized in two forms. The first one is an array of U-shaped conducting strips printed on a dielectric sheet. The other case is that of an array of slots etched in a conducting screen. Each of the two cases has a certain frequency response to the incident electromagnetic wave as will be shown in the following sections.

4.2 U-Shaped Conducting Strips on A Dielectric Sheet

The first case to be considered in this chapter is an array of U-shaped strips printed on a dielectric substrate. The case is studied using the unit cell approach geometry shown in Fig. 4.1. A square cell of 34mm side length is assumed, which is 0.397 of the wavelength at the operating frequency of 3.5GHz. This frequency is chosen as a study case representing the WiMax systems. The U-shaped copper strip is placed on FR4 substrate of 0.8 mm thickness, dielectric of constant 4.4, and loss tangent of 0.025. The copper plane thickness is 0.035mm, and the U-shaped strip has a width of $w = 1\text{mm}$, the total length of 71mm $\ell = 30.5\text{mm}$ and center part length ℓ_c is 10mm.

A uniform plane wave is assumed to be normally incident on the dielectric sheet with copper U-shaped strips. The interaction of the incident wave with the copper can be studied into two cases. The first is when the electric field of the E-field is parallel to the legs of the U-shaped strips. The other case is that when

the incident wave is perpendicular to the legs of the U-shaped strips. The two cases are investigated in the following two sub-sections.

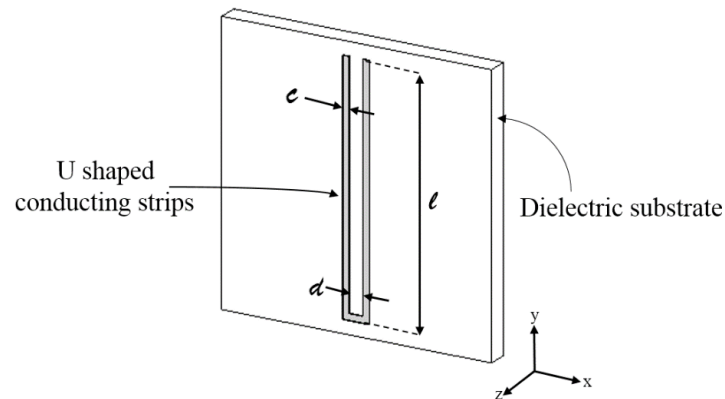


Fig. 4.1. The geometry of the proposed FSS structure with the U-shaped strips.

4.2.1 E-field is Parallel to the U-strip ($E \parallel U$)

As shown in Fig. 4.1, the incident wave on the FSS screen is assumed linearly polarized propagating along the Z-axis with E-field oriented along the Y-axis, i.e., parallel to the legs of the U-strip. The unit cell approach is used to represent the case of a 2-dimensional array of the U-shaped strips. The proper boundary conditions for this case are PEC perpendicular to the Y-axis and PMC perpendicular to the X-axis. The input and output ports are placed along the Z-axis shown in Fig. 4.2. The frequency-domain solver is used in the simulation and the frequency range of 1 to 6 GHz is used.

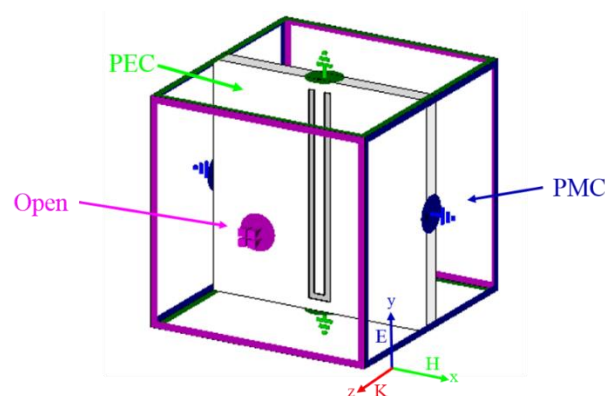


Fig. 4.2. Simulation setup for the unit cell in CST. The E-field of the incident wave is along the Y-axis ($E \parallel$ to the strip legs).

The obtained results of the S-parameters are shown in Fig. 4.3. The results show a band-reject property at 3.5GHz with a reflection coefficient of -0.1dB, and transmission coefficient of -36dB.

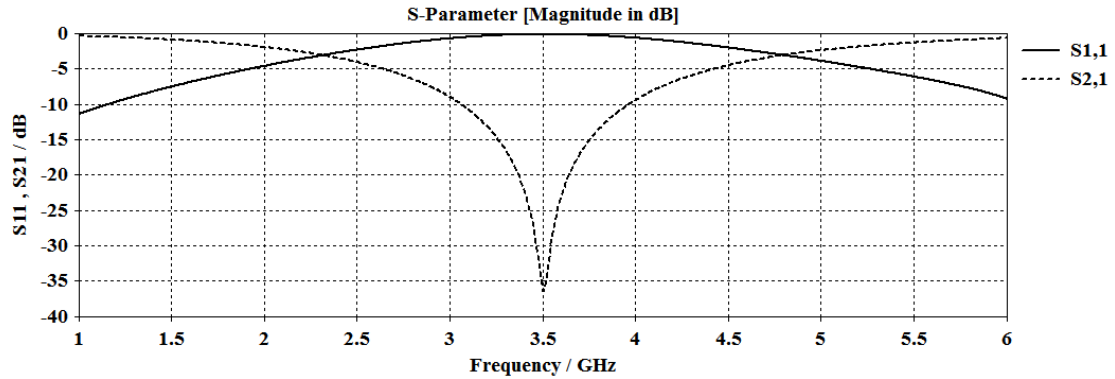


Fig. 4.3 Transfer characteristics of the U-shaped strip when the E-field is Y-directed ($\epsilon = 1\text{mm}$, $\ell = 30.5\text{mm}$, and d is 10mm).

The characteristics of the U-shaped strip FSS structure, such as the resonance frequency and stopband depend on the structural parameters of the U-shape. The strip length, strip width, and distance between the two legs of the strips are the parameters that control the transfer characteristics. In Fig. 4.4, the simulated transfer characteristics for the U-shaped FSS filter are plotted for various slot lengths while keeping $d = 10\text{mm}$, $\epsilon = 1\text{mm}$ constants. The figure shows that as the strip length is increased, the resonance frequency decreases. A length change of $\pm 1\text{mm}$ or 3.3% has resulted in a frequency change of about $\pm 7\%$.

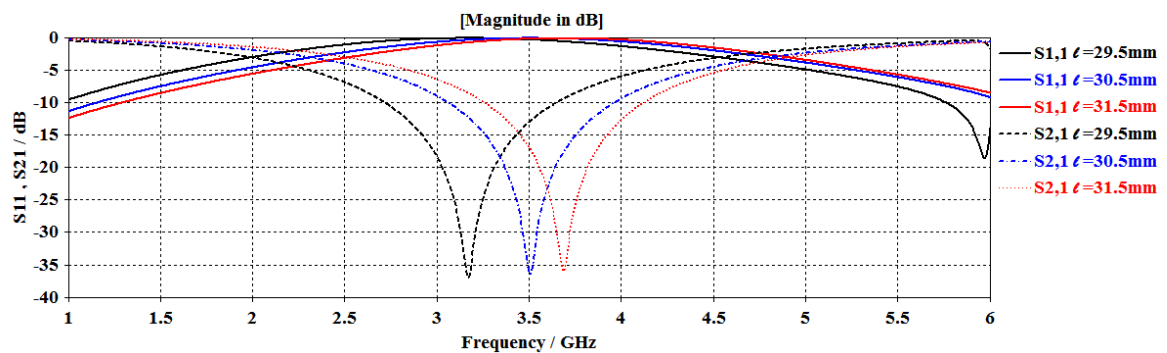


Fig. 4.4. Transfer characteristics of the U-shaped FSS structure for various total length ($d = 10\text{mm}$, $\epsilon = 1\text{mm}$).

The transfer characteristics for various strip width are also simulated, and the computed results are shown in Fig. 4.5, when $\ell = 30.5\text{mm}$, and $d = 10\text{mm}$. The line width of the U-shaped strip influences the resonance frequency and the width of the reject band. The figure shows that a larger strip width results in the wider passband, and slightly higher center frequency. When the strip width was changed by four folds (from 0.5mm to 2mm), the center frequency changes by only 11.4%. The influence of the strip width on the resonance frequency can be attributed to the mutual coupling between the two legs of the strip.

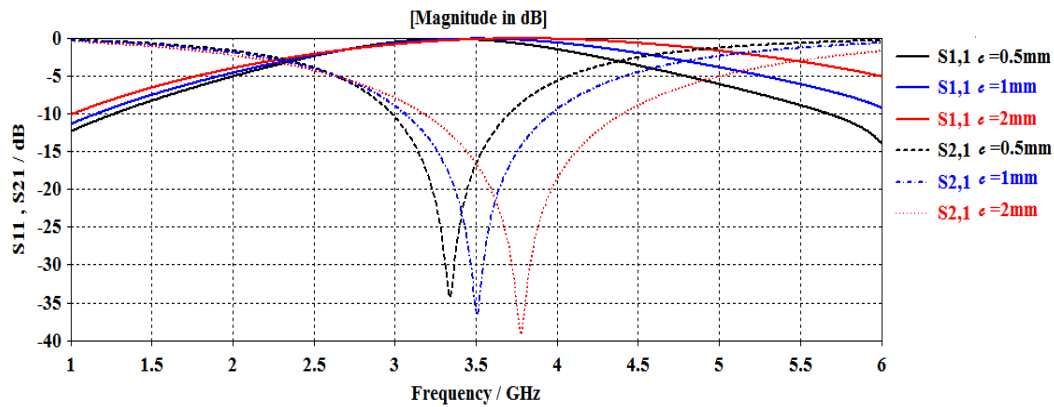


Fig. 4.5 Transfer characteristics of U-shaped FSS structure for various line width e ($\ell = 30.5\text{mm}$ and $d = 10\text{mm}$).

Figure 4.6 shows the effect of modifying the separation distance between the two legs of the U-shaped strip while keeping the total U-shaped length unchanged. It can be noted that the resonance frequency slightly decreases (by about 12.2%) when the separation distance is reduced from 13 mm to 7mm. Such an effect can be attributed to the mutual coupling between the two legs of the strip, where larger separation distance d means lower mutual coupling.

The effective permittivity and permeability of the FSS strip structure are calculated using the procedure described in section 2.4, and the obtained results are shown in Fig. 4.7. It can be seen that the effective permittivity and

permeability acquire negative real values around and above the resonance frequency.

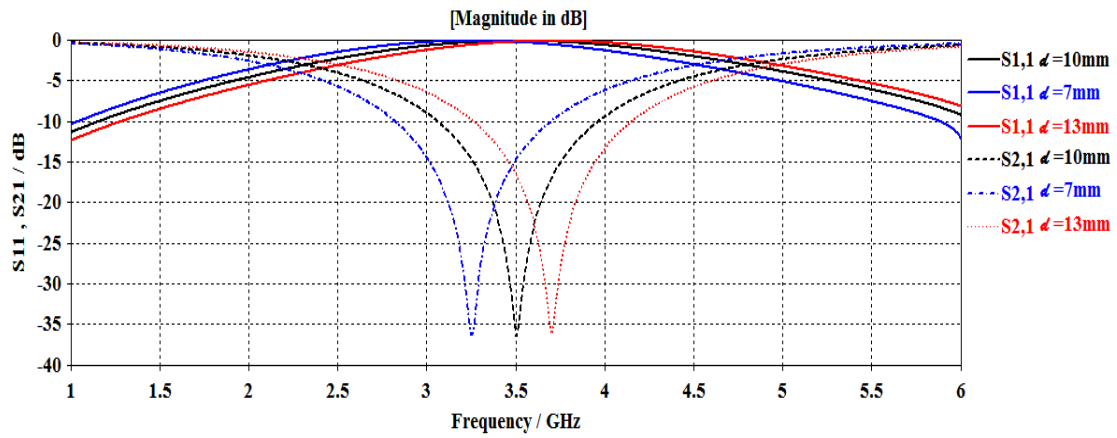


Fig. 4.6 Transfer characteristics of U-shaped FSS structure for various center part lengths d ($\ell = 30.5\text{mm}$ and $\epsilon = 10\text{mm}$).

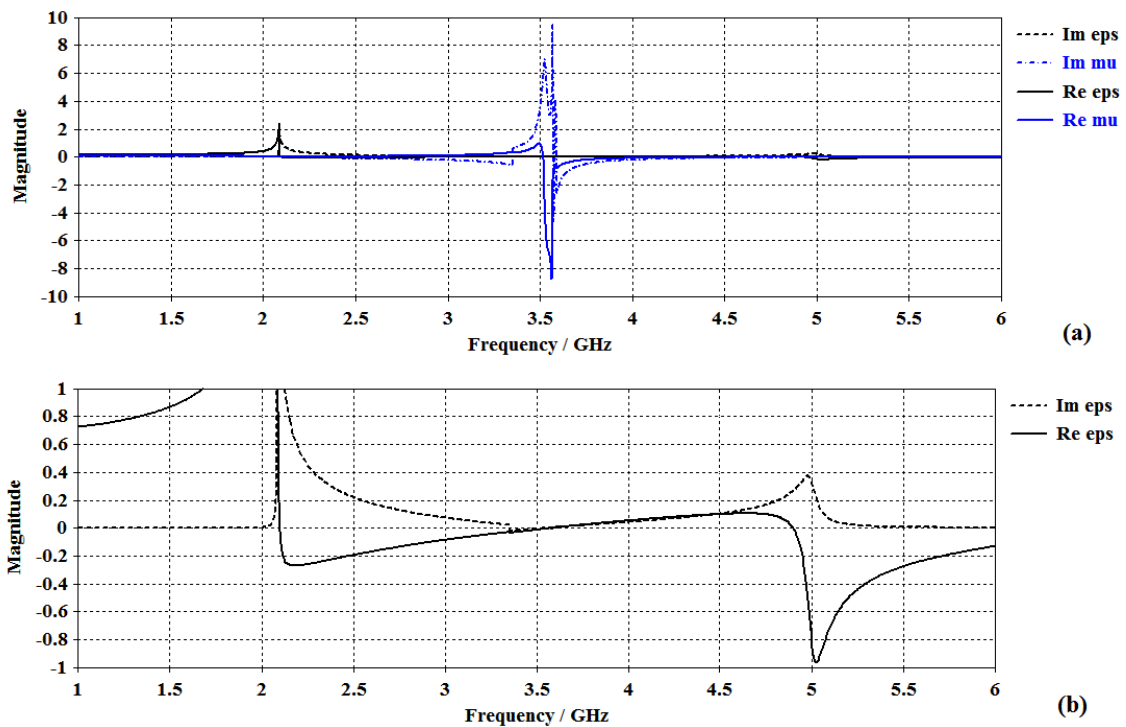


Fig. 4.7 (a) Extracted effective permittivity and permeability of the U-shaped ($\ell = 30.5\text{mm}$, $\epsilon = 1\text{mm}$, and $d = 10\text{mm}$). (b) Zoom figure of the extracted effective permittivity. The solid line represents the real part, while the dashed line represents the imaginary part.

For a better insight into the effect of the U-shaped strip on the propagation properties of the FSS structure for the above case, the electric field distribution along the U-shaped strip as well as the surface current density on the strip is studied. Figure 4.8 shows the electric field distribution around the U-shaped strip at the frequency of the reject band of 3.5GHz and another frequency in the passband such as 5GHz. Figure. 4.9, on the other hand, displays the surface current density for the corresponding cases. For the frequency of 3.5GHz, the E-field is concentrated along the two legs and the center of the U-shaped strip, while the current density has peaks on the two legs. The distribution of the E-field and current density represents one guided-wavelength variation, as shown in Figs. 4.8 and 4.9. At the 5GHz frequency, the E-field around the strip has an approximately uniform value of 8690 V/m, which is much lower than that (21350V/m) for the 3.5GHz case. The current density has small values along the strip, as indicated by Fig. 4.9-b. Thus, the U-shaped strip is not resonating at the 5 GHz frequency, and the incident wave penetrates the FSS structure with a low loss of about -3.9 dB.

The average length of the U-shaped strip can be found from the geometry of Fig. 4.1 as:

$$LS = 2 \times (\ell - c / 2) + d + 2 \times (c / 2) = 2 \ell + d \quad (4.1)$$

For the dimensions of investigated U-shaped strip, the length of the strip according to Eq. 4.1, and the wavelength at the frequency of 3.5 GHz are:

the wavelength in air $\lambda_0=85.714\text{mm}$, and the strip length $LS=71\text{mm}$. As Figs. 4.8 and 4.9 show, the E-field and current density exhibit one wavelength variation along the strip. Accordingly, one may conclude that:

$$LS = \lambda_g = 71 \text{ mm},$$

Since λ_g and λ_0 are related by the effective permittivity ϵ_e as

$$\lambda_g = \frac{\lambda_0}{\sqrt{\epsilon_{re}}} \quad (4.2)$$

Then substituting into Eq. 4.2 for the above values of λ_g and λ_o yields

$$\epsilon_{re} = (85.714/71)^2 = 1.46$$

This value is some way between the relative permittivity for air ($\epsilon_{ro} = 1$) and that for the FR4 substrate ($\epsilon_{rs} = 4.4$). It should be noted that the U-shaped strip is printed as a 2-dimensional array on the FR4 substrate, rather than there is a single strip as the case with printed antennas. For the printed antenna a rough estimate for the effective relative permittivity has been given by:

$$\epsilon_{re} = (1 + \epsilon_{rs}) / 2$$

which for the above substrate yield $\epsilon_{re} = 2.7$.

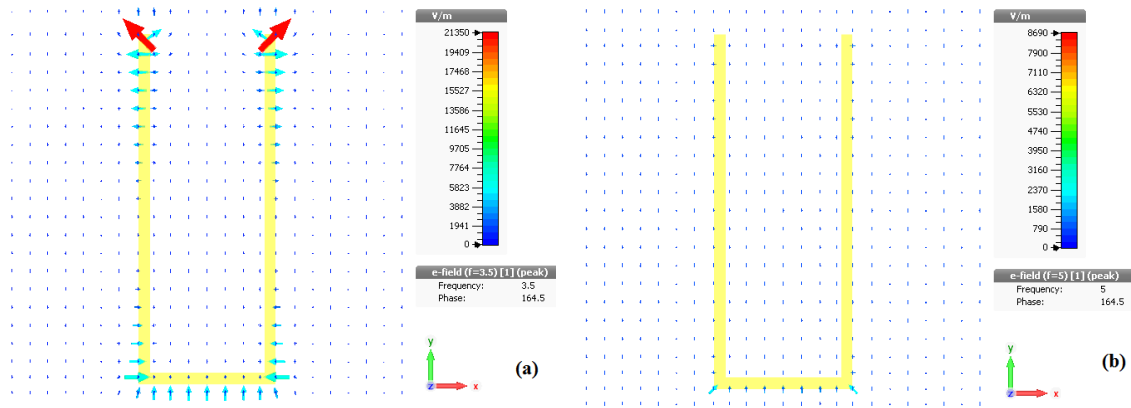


Fig. 4.8 Simulated E-field distribution around the U-shaped strip. The E-field of the incident wave is along the Y-axis ($E \parallel$ to the strip legs).

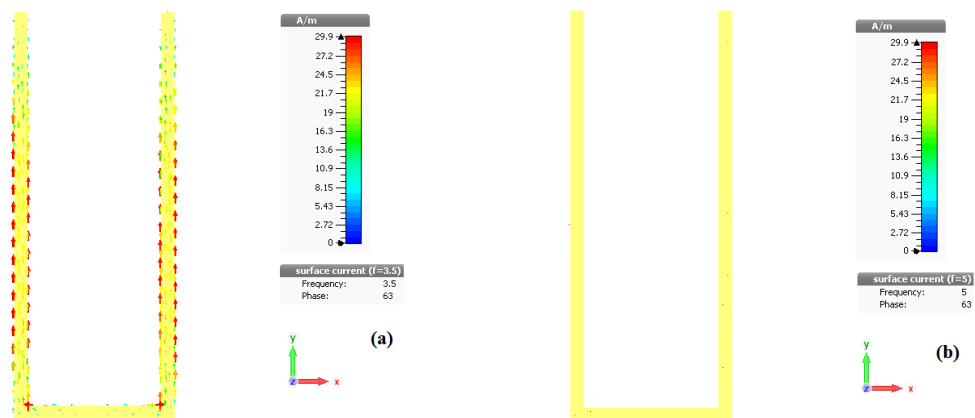


Fig. 4.9 Simulated current distribution on the U-shaped strip. The E-field of the incident wave is along the Y-axis ($E \parallel$ to the strip legs).

The radiation from the U-shaped strip of the FSS structure is investigated to explore if the U-shaped strip blocks the radiation at resonance. Figure 4.10 shows a 3-D display of the simulated gain of the U-shaped strip at frequencies of 3.5GHz and 5GHz, which represent the reject and passbands respectively. In this simulations, a source is applied to one port at one side of the plane containing the strip while the other port was set to open-add-space. The figure shows that the radiation at 3.5GHz is extremely low (gain = -9.4dB) as the strip resonates, and the incident wave is almost totally reflected. At the 5GHz frequency, the incident wave passes through the U-shaped FSS (gain=5.9dB). These results confirm those shown in Fig. 4.3.

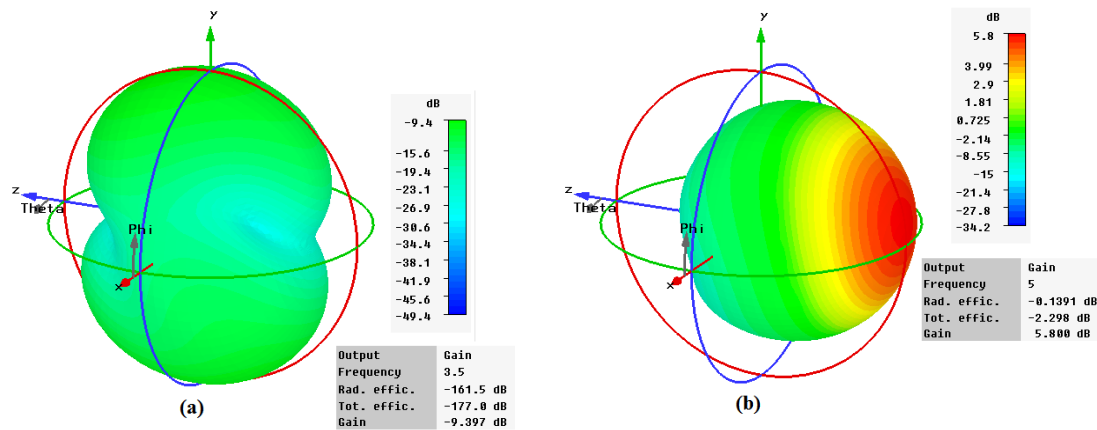


Fig. 4.10 Radiation pattern of the U-shaped strip (a) 3.5Ghz, and (b)5GHz. The E-field of the incident wave is along the Y-axis ($E \parallel$ to the strip legs).

4.2.2 E-field is Perpendicular to the U-strip ($E \perp U$)

In this case, the incident wave on the FSS screen is assumed linearly polarized, propagating along the Z-axis, and its the E-field vector is along the X-axis, i.e., perpendicular to the strip legs. To simulate this case, the boundary conditions of the unit cell should be; PEC surfaces perpendicular to the X-axis and PMC surfaces perpendicular to the Y-axis. The input and output ports are placed along the Z-axis, as shown in Fig. 4.11. The frequency-domain solver was used for the simulation, which is performed for the frequency range of 1 to 6 GHz.

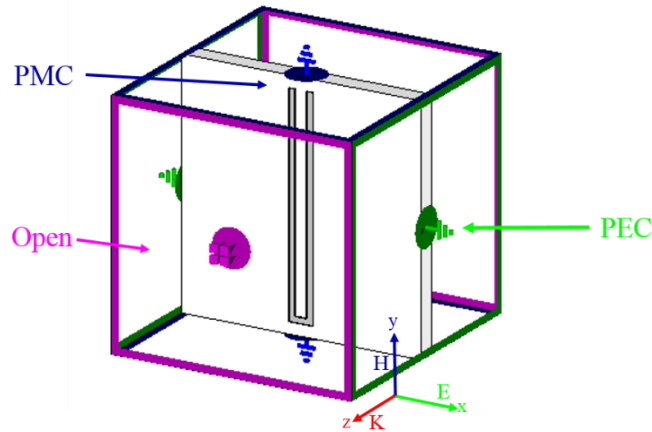


Fig. 4.11. Simulation setup for the unit cell in CST. The E-field of the incident wave is along the X-axis, ($E \perp$ to the strip legs).

The obtained results from the simulation using the same dimensions of the strip studied in the former section ($\ell = 30.5\text{mm}$, $e = 1\text{mm}$, and d is 10mm) are shown in Fig. 4.12. The result also indicates a band reject property as with the former case but at 1.65GHz with a reflection coefficient less than -1dB , and transmission coefficient -18dB . The reject band feature is repeated at a higher frequency of 5.2GHz , which is about 3.15 of the first frequency of 1.65GHz . In this case, the E-field is perpendicular to the log parts (legs) of the U-shaped strip, and it is parallel to the short part (central part) of the strip. This is an opposite orientation to that studied in the former section; thus, it is expected to yield different behavior.

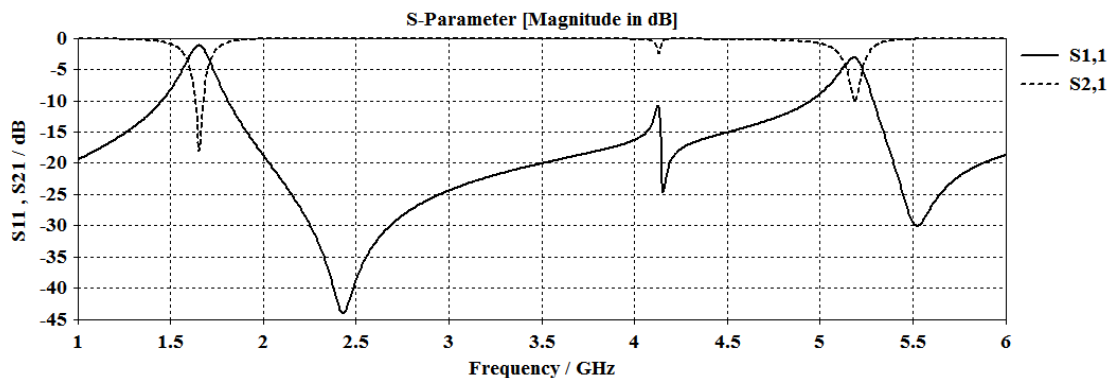


Fig. 4.12. Transfer characteristics of U-shaped strip when the E-field is X-directed ($\ell = 30.5\text{mm}$, $e = 1\text{mm}$, and $d = 10\text{mm}$).

By keeping the same properties of the boundary conditions that are shown in Fig. 4.11, and decreasing the total length of the strip to 32mm where $\ell = 13\text{mm}$, $d = 6\text{mm}$, and $e = 1\text{mm}$, the resonance frequency was shifted to 3.5GHz, and the performance of the FSS structure is enhanced (higher reflection coefficient S_{11} and lower transmission coefficient S_{21}) at the center frequency as shown in Fig. 4.13.

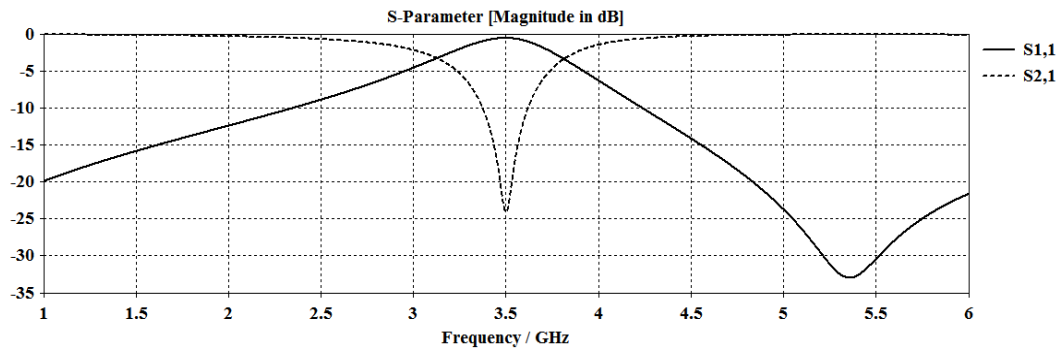


Fig. 4.13. Transfer characteristics of the U-shaped strip when the E-field is X-directed ($\ell = 13\text{mm}$, $e = 1\text{mm}$, and $d = 6\text{mm}$).

The effective permittivity and permeability of the FSS strip structure are calculated using the procedure described in section 2.4, and the obtained results are shown in Fig. 4.14. It can be seen that the effective permeability acquires negative real values around and above the resonance frequency while the effective permittivity changes in positive value around the resonance frequency.

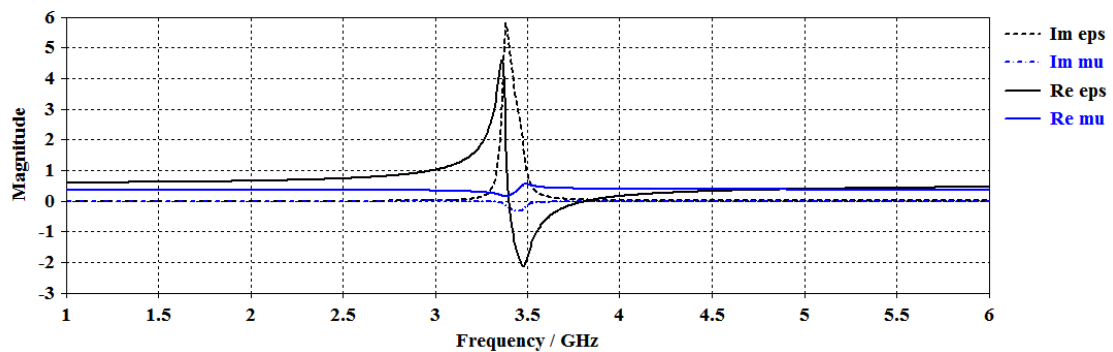


Fig. 4.14 Extracted effective electric permittivity and magnetic permeability of U-shaped ($e = 1\text{mm}$, $\ell = 13\text{mm}$, and $d = 6\text{mm}$).

The electric field distribution and the surface current density around the U-shaped strip were studied, and the obtained results are shown in Figs. 4.15 and 4.16. Figure 4.15 shows the electric field distribution in the U-shaped strip at the frequencies of the reject band 3.5GHz and the pass-band 5GHz. For the 3.5GHz frequency, the E-field near the two legs of the U-shaped strip are in maximum and tends to zero at the center of the legs. Such variation shows half wavelength, and thus the strip is resonating. On the same time, Fig.4.16 shows that the surface current density achieves maximum value at the center of the strip, and confirms the half wavelength variation along the strip. At the 5GHz frequency E-field intensity near the strip and the surface, current density has a much lower value compared to that for the 3.5GHz case. Thus, the U shaped strip shows no resonance.

It should be mentioned that Figs. 4.15 and 4.16 show the results for the case of ($\epsilon = 1\text{mm}$, $\ell = 13\text{mm}$, and d is 6mm), i.e. the total length of the strip is 32 mm .

Recalling the analysis of the former section,

$$LS = 0.5 \lambda_g = 32 \text{ mm},$$

Thus, $\lambda_g = 64 \text{ mm}$, and using Eq. 4.2 the effective relative permittivity will be:

$$\epsilon_{re} = (85.714/64)^2 = 1.79.$$

The difference from that obtained for the case when the E-field is parallel to the legs of the U-shaped strip can be attributed to the fact that the relation between the conducting strip and the E-field are different for the two cases. The permittivity is a relation between the electric displacement and E-field intensity, which are influenced by the special relation of their vectors.

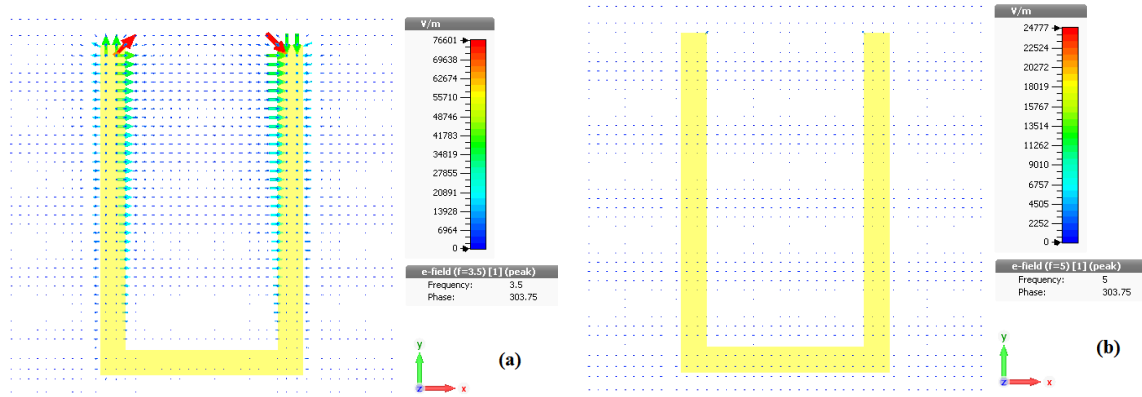


Fig. 4.15 Simulated E-field distribution inside the U-shaped strip. (a) at 3.5GHz. (b) At 5GHz. The E-field of the incident wave is along the X-axis, ($E \perp$ to the slot legs).

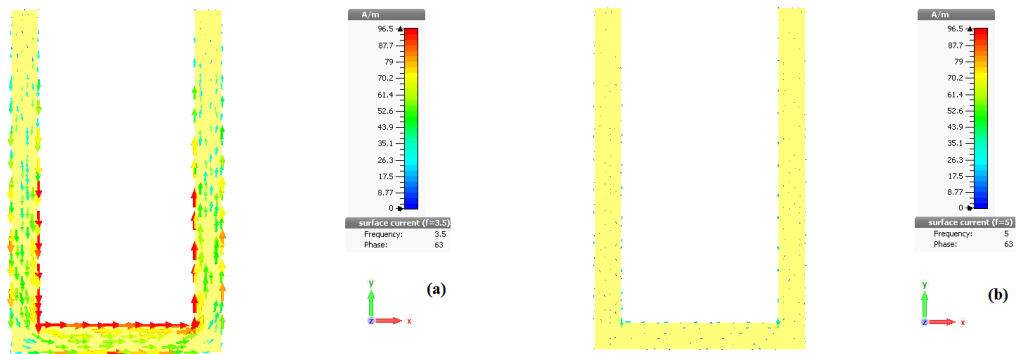


Fig. 4.16 Simulated surface-current distribution around the U-shaped strip. (a) at 3.5GHz. (b) At 5GHz. The E-field of the incident wave is along the X-axis, ($E \perp$ to the slot legs).

4.3 U-slots in a Conducting Sheet

The second case to be considered in this chapter is an array of U-shaped slots in a conducting plane screen. The case is studied using the unit cell approach geometry shown in Fig. 4.17. A square cell of 34mm side length is assumed, which is 0.85 of the wavelength at the operating frequency of 3.5GHz. The U-shaped element is etched on the copper coated FR4 substrate of 0.8 mm thickness, dielectric of constant 4.4, and loss tangent of 0.025. The copper plane thickness is 0.035mm, and the U-shaped slot has a width of ϵ

$=1\text{mm}$, $\ell = 29\text{mm}$ and center separation d of 10mm ; thus the total length is 68mm . A uniform plane wave is assumed to be normally incident on the copper plane with the etched slots. The interaction of the incident wave with the copper can be studied as two cases. The first is when the electric field of the incident wave is perpendicular to the legs of the U-slot. The other case is that when the E-field is parallel to the legs of the U-slot. The two cases are investigated in the following two sections.

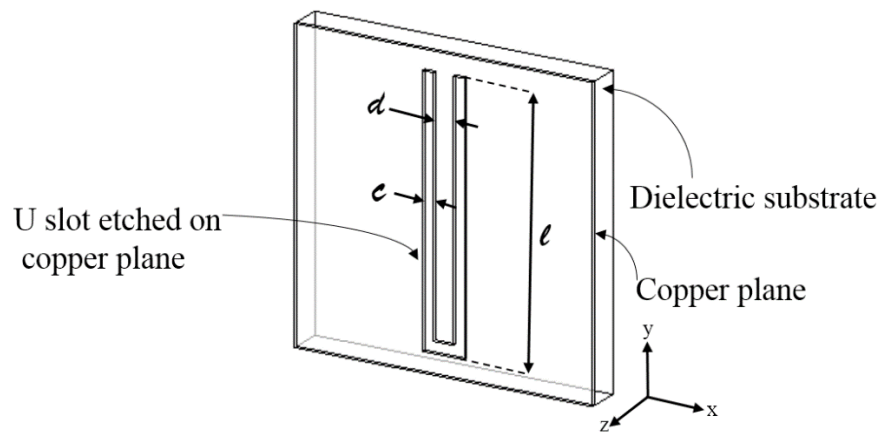


Fig. 4.17. The geometry of the proposed U-slots FSS structure.

4.3.1-E-field is Perpendicular to the U-Slot ($E \perp U$)

As shown in Fig. 4.17, the incident wave on the FSS screen is assumed linearly polarized and propagating along the Z-axis with the E-field vector along the X-axis. To simulate this case, the used boundary conditions of the unit cell are; PEC surfaces perpendicular to the X-axis and PMC surfaces perpendicular to the Y-axis. The input and output ports are placed along the Z-axis shown in Fig. 4.18. The frequency-domain solver is used for the simulations which were performed for the frequency range of 1 to 6 GHz.

The obtained results of the S-parameters are shown in Fig. 4.19. The results show a bandpass property at 3.5 GHz with a reflection coefficient of -26dB , and transmission coefficient of -0.3dB .

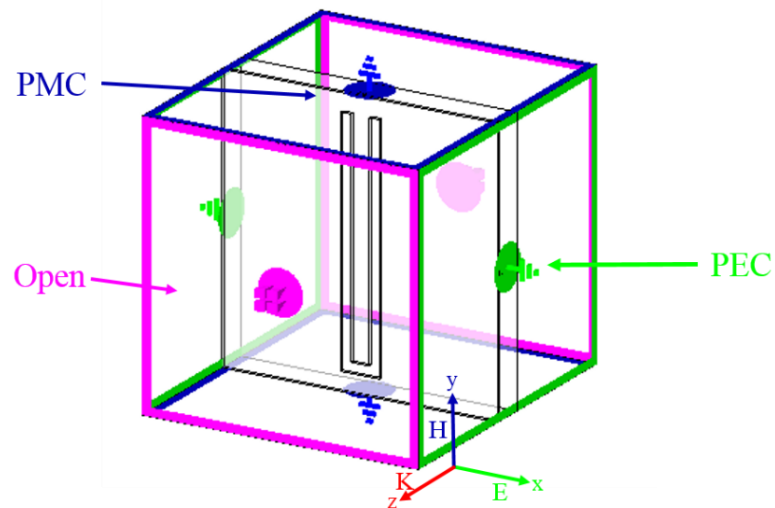


Fig. 4.18. Simulation setup for the unit cell in CST. The E-field of the incident wave is along the X-axis, ($E \perp$ to the slot legs).

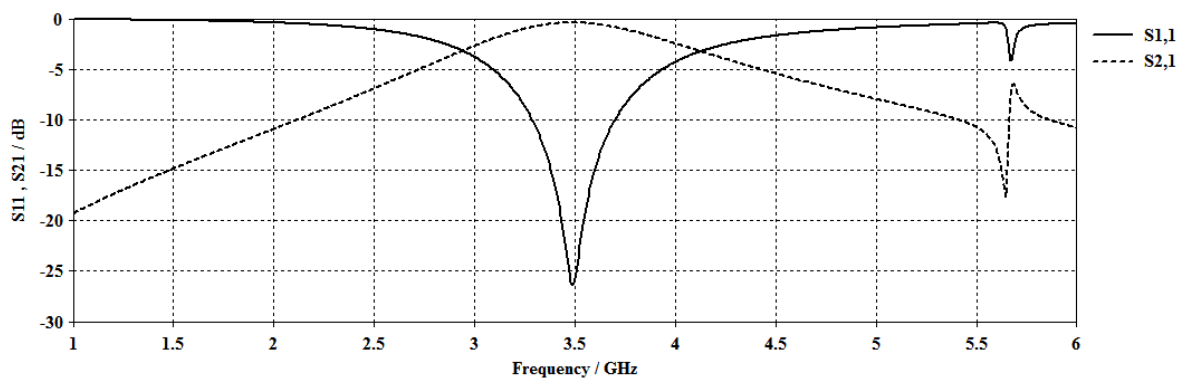


Fig. 4.19. Transfer characteristics of the U-slot when the E-field is X-directed ($\epsilon = 1\text{mm}$, $\ell = 29\text{mm}$, and $d = 10\text{mm}$).

The characteristics of the U-slot FSS structure, such as the resonance frequency and passband depend on the structural parameters of the U-slot. The slot length, slot width, and distance between the two legs of the slot are the parameters that control the transfer characteristics. In Fig. 4.20, the simulated transfer characteristics for the U-slot filter are plotted for various slot lengths while keeping $d = 10\text{mm}$, $\epsilon = 1\text{mm}$ constants. The figure shows that as the slot length is increased from 28mm to 30mm (7% change), the resonance frequency decreases by about 7%.

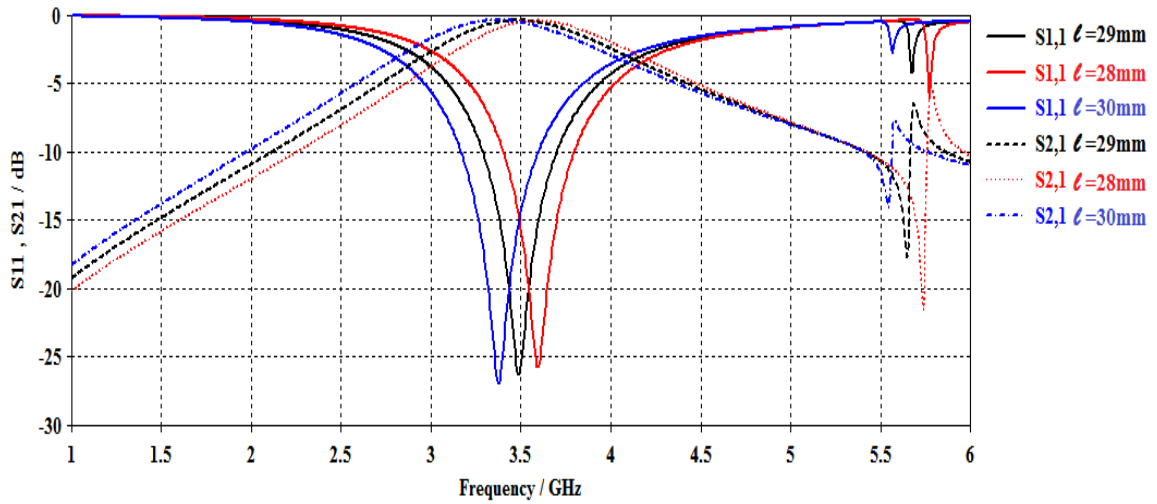


Fig. 4.20 Transfer characteristics of the U-slot FSS structure for various total length ($d=10\text{mm}$, $e=1\text{mm}$).

The transfer characteristics for various slot widths are also simulated, and the obtained results are shown in Fig. 4.20, when $l=29\text{mm}$, and $d=10\text{mm}$. The width of the slot influences the resonance frequency and the width of the passband. The figure shows that a larger slot width results in the wider passband, and slightly higher center frequency. Figure 4.22 shows the effect when modifying the distance d between the two legs of the slots while keeping the total U-slot length unchanged. It can be noted that the resonance frequency slightly decreases (by about 7.6%) when the separation distance is reduced from 15 mm to 5mm (i.e., down to 1/3 of the initial value). Such an effect can be attributed to the mutual coupling between the two legs of the slot, where larger separation distance d means lower mutual coupling.

The effective permittivity and permeability of the FSS slot structure are calculated using the procedure described in section 2.4, and the obtained results are shown in Fig. 4.23. It can be seen that both of the effective permittivity and permeability acquire negative real values around and above the resonance frequency.

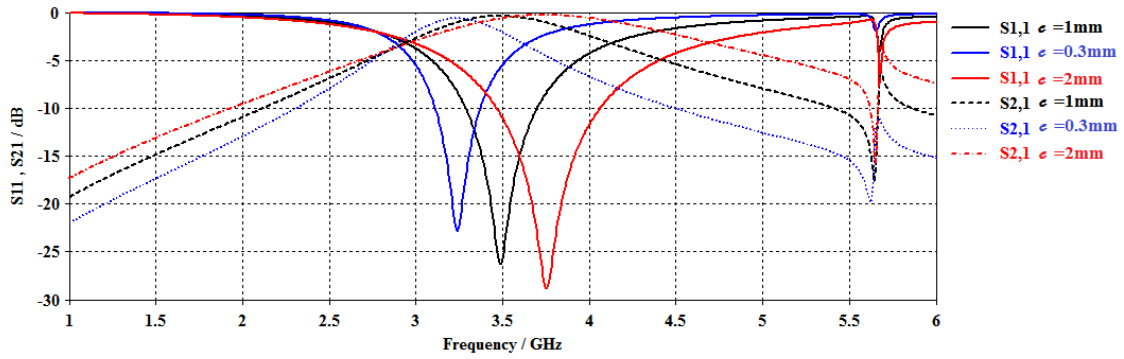


Fig. 4.21 Transfer characteristics of the U-slot FSS structure for various slot widths e ($\ell=29\text{mm}$ and $d=10\text{mm}$).

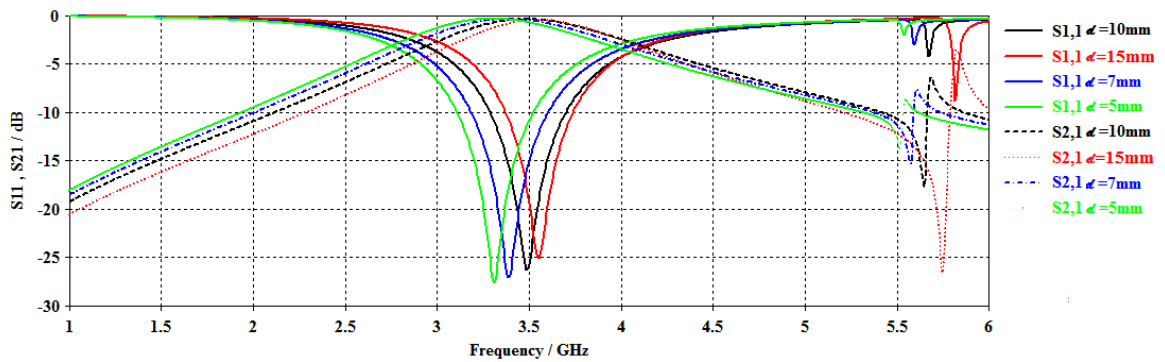


Fig. 4.22 Transfer characteristics of the U-slot FSS structure for various center part lengths d ($\ell=29\text{mm}$ and $e=1\text{mm}$).

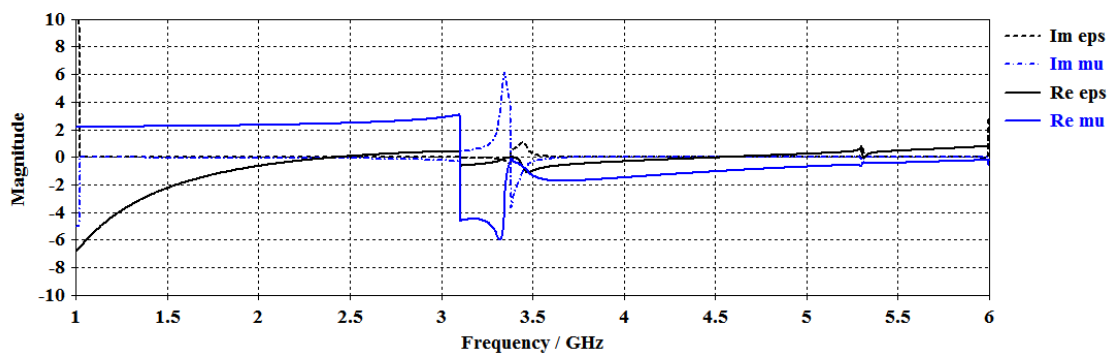


Fig. 4.23 Extracted effective permittivity and permeability of the U-Slot ($e=1\text{mm}$, $\ell=29\text{mm}$, and d is 10mm). The solid line represents the real parts, while the dashed line represents the imaginary parts.

The electric field distribution along the U-shaped slot is studied. Figure 4.24 shows the electric field distribution in the U-slot legs at the center frequency (3.5GHz) of the passband, and the other frequency (5GHz)

representing the reject band. For the 3.5GHz frequency, the E-field vectors inside the two legs of the U-shaped are in the same directions as that of the E-field of the incident wave. The total variation of the E-field along the slot shows one guided wavelength; thus the slot is resonating at the 3.5 GHz. The fact that the E-field has the same direction along the two legs explains the passband property of the slot. At the 5GHz frequency, the E-field inside the U-shaped slot is very small, indicating no resonance and small transfer coefficient through the FSS surface.

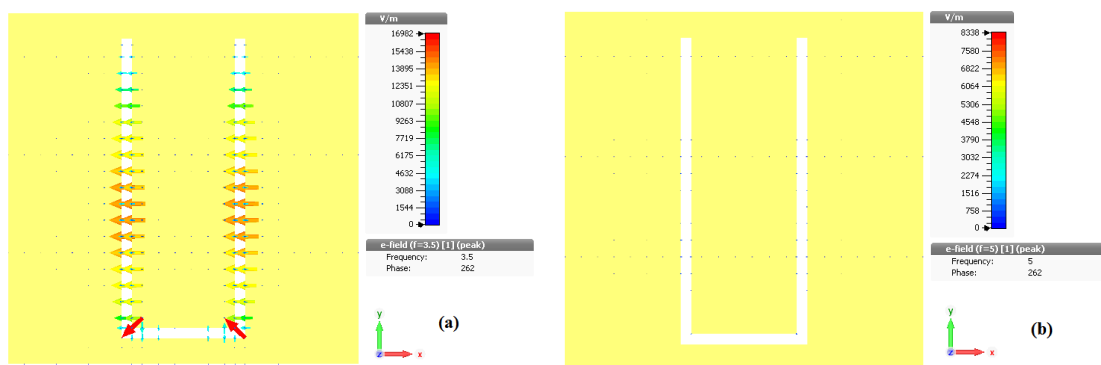


Fig. 4.24 Simulated E-field distribution inside the U-slot. (a) at 3.5GHz. (b) at 5GHz. The E-field of the incident wave is along the X-axis, ($E \perp$ to the slot legs).

The radiation from the U-shaped slot of the FSS structure was investigated to explore if the U-shaped slot passes the incident wave at the resonance frequency. Figure 4.25 shows a 3-D display of the simulated gain of the U-shaped slot at 3.5GHz and 5GHz, which represent the pass and reject bands respectively. In this simulation, a source is applied to one port of the line in the positive Z-axis while the other port was set to open-add-space. The figure shows that there is appreciable radiation at 3.5GHz (gain= 2.62dB) since the slot resonates at this frequency and transmits the wave to the other side of the FSS. However, at the frequency of 5GHz, the radiation is very low (gain= -2.13dB). Since the slot is out of resonance, the penetration of the

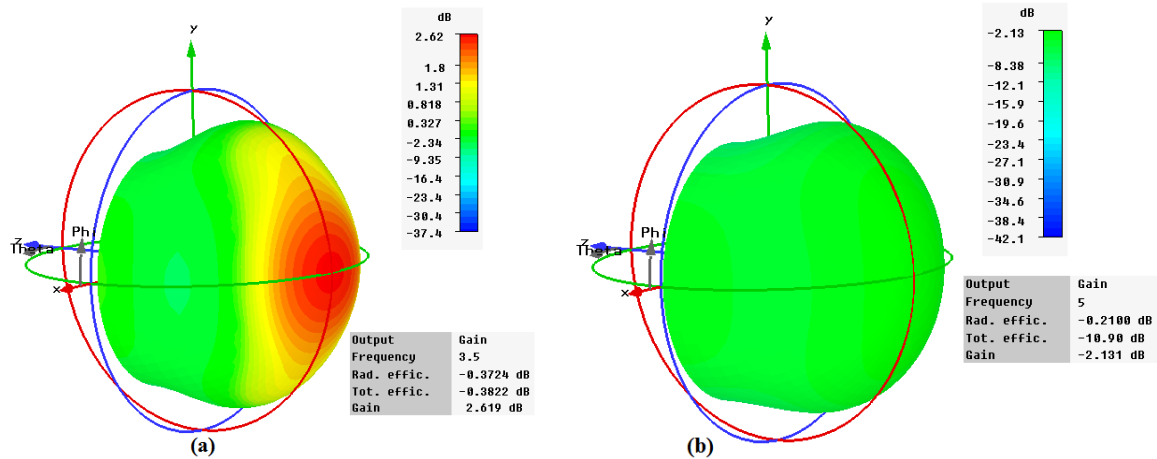


Fig. 4.25 Radiation patterns of the U-slot; (a) at 3.5GHz, (b) at 5GHz. The E-field of the incident wave is along the X-axis, ($E \perp$ to the slot legs).

incident wave through the slot is minimal. These results are in very good agreement with those shown in 4.19.

4.3.2-E-field is Parallel to the U-Slot ($E \parallel U$)

In this case, the incident wave is also propagating along the Z-axis, but its E-field is now oriented along the Y-axis, i.e., is parallel to the legs of the U-slot. The used boundary conditions for this case are PEC surfaces perpendicular to the Y-axis, and PMC surfaces perpendicular to the X-axis. The input and output ports are placed along the Z-axis, which is shown in Fig. 4.26.

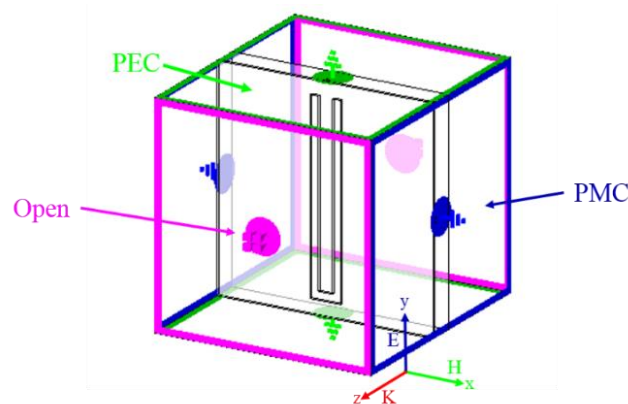


Fig. 4.26. Simulation setup for the unit cell in CST. The E-field of the incident wave is along the Y-axis ($E \parallel$ to the slot legs).

The obtained results of the S-parameters are shown in Fig. 4.27. The results indicate a passband property at 1.67GHz with a reflection coefficient of -12.6dB, and transmission coefficient of -2.3dB. The passband feature is repeated at a higher frequency of 4.8 GHz, which is about three times the first frequency of 1.67GHz.

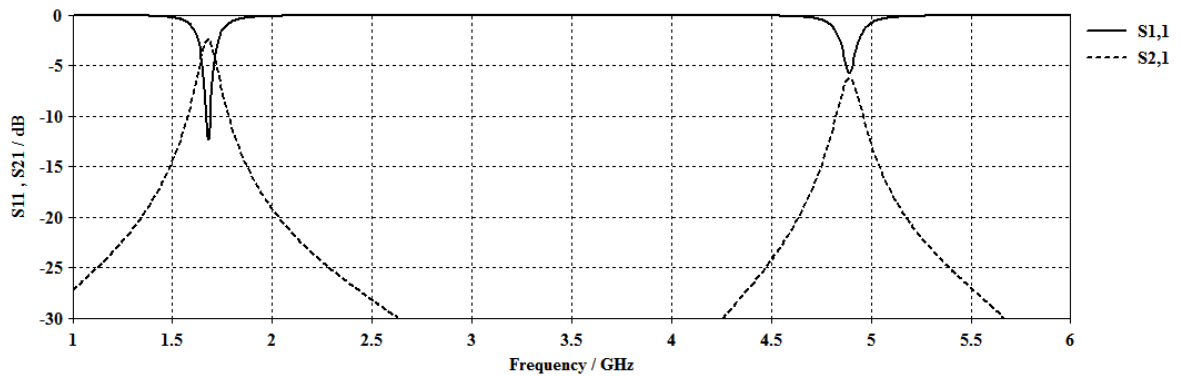


Fig. 4.27. Transfer characteristics of the U-shaped slot when the E-field is Y-directed ($\ell=29\text{mm}$, $\epsilon=1\text{mm}$, and d is 10mm).

By keeping the same properties of the boundary condition which is shown in Fig. 4.26 and decreasing the total slot length to 32mm where $\ell=13\text{mm}$, $d=6\text{mm}$, and $\epsilon=1\text{mm}$, the resonance frequency is shifted to 3.5GHz, and the performance of the FSS structure is enhanced (S_{11} decreases to -17.5 dB and S_{21} increase to -1.2 dB) as shown in Fig. 4.28.

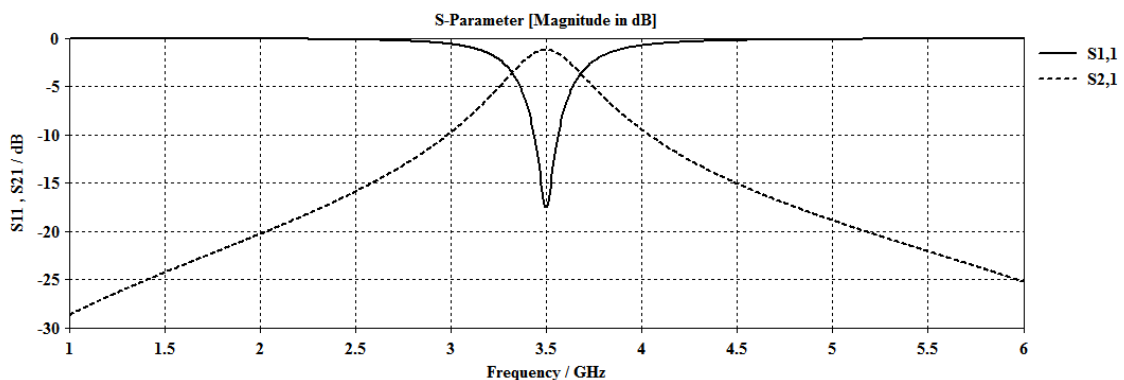


Fig. 4.28. Transfer characteristics of the U-shaped strip when the E-field is Y-directed ($\ell=13\text{mm}$, $\epsilon=1\text{mm}$, and $d=6\text{mm}$).

The effective permittivity and permeability of the FSS slot structure are calculated using the procedure described in section 2.4, and the obtained results are shown in Fig. 4.29. It can be seen that the effective permeability acquires negative real values around and above the resonance frequency while the effective permittivity changes in positive value around the resonance frequency.

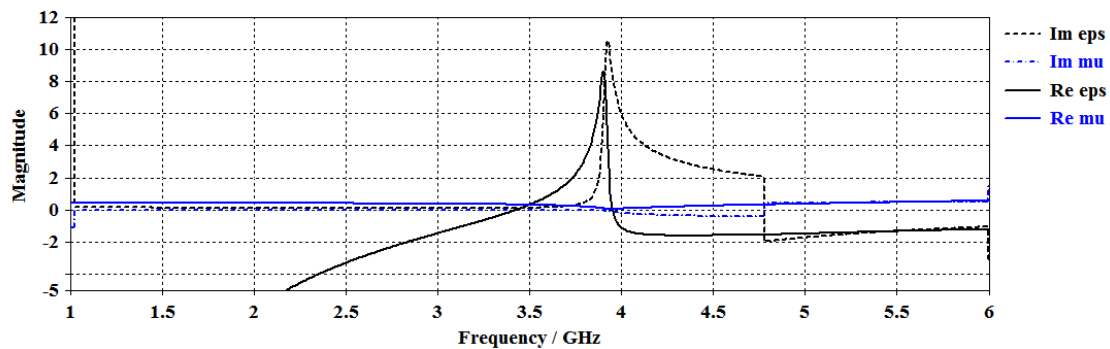


Fig. 4.29 Extracted effective permittivity and permeability of U-Slot ($\ell = 13\text{mm}$, $\epsilon = 1\text{mm}$, and $d = 6\text{mm}$). The solid line represents the real part, whereas the dashed line represents the imaginary part.

The electric field distribution along the U-shaped slot is studied. Figure 4.30 shows the electric field distribution in the U-shaped slot at the frequencies of the passband of 3.5GHz and the reject band of 5GHz. The E-field vectors inside the two legs of the U-shaped are in opposite directions. The E-field across the central part is at maximum and in the same direction of the incident field, which explains the transmission through the slot at the 3.5 GHz frequency. At the 5GHz frequency, the E-field inside the U shaped slot has a very low value indicating no resonance, which explains why there is no transmission through the slot.

As the E-field along the slot has a variation representing a half guided wavelength, the relation between the slot length LS and the guided wavelength λ_g will be:

$$LS=0.5 \lambda_g$$

Which at 3.5 GHz yields

$$LS=32 = 0.5 \lambda_g , \quad \lambda_g = 64$$

Then the effective permittivity will be

$$\epsilon_{re} = (85.714/64)^2 = 1.79.$$

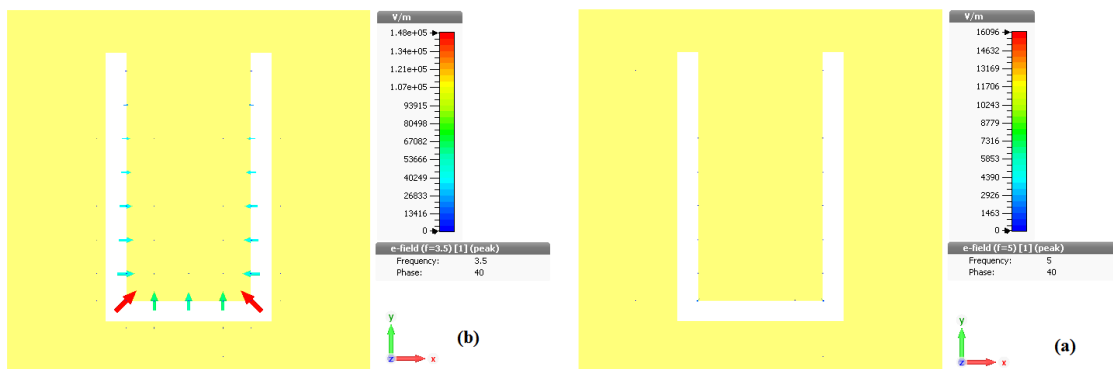


Fig. 4.30 Simulated E-field distribution inside the U-slot. (a) at 3.5GHz. (b) at 5GHz. The E-field of the incident wave is along the Y-axis (E// to the slot legs).

CHAPTER FIVE

CONCLUSIONS AND FUTURE WORK

CHAPTER FIVE

CONCLUSIONS AND FUTURE WORK

5.1 Conclusions

Planar metamaterial structures can have the form of certain metallic patterns printed on a substrate or can be as certain forms of slots in a conducting screen. It has been demonstrated that the frequency selective property of the metamaterial structures can be utilized for the design of a compact band-reject filter. The same idea has been demonstrated as a frequency selective surface.

The contributions of the study can be summarized as follows:

- 1- A slot folded into U-shape can be etched on the microstrip line to achieve a band-reject filter. The filter has a compact size, as its length is quarter of the effective wavelength at the stopband due to the folding of the slot. The characteristics of the U-slot filter, such as the resonance frequency and bandwidth, are influenced by the slot length, slot width, and the distance between the two legs of the slot.
- 2- Two U-slots can be embedded in the microstrip line to improve the performance of the filter. The slots can be deployed in three different configurations. These include face-to-face, back-to-back, and interlaced. In the first two configurations, larger rejection has been obtained by using the two slots. The separation between two slots shows an effect on the performance of the filter as the bandwidth increases and offers slightly higher value transfer characteristic. In the interlaced case, a wider spectrum band is achieved with reasonable values of transfer characteristics. The interlaced U-slots provides a sharper and wider reject-band and improves the insertion loss and port matching.

- 3- The extraction of the effective parameters of the four configurations of the designed filters shows negative values of the permittivity, and the permeability occurring around the resonance frequency that confirms the slot exhibiting a metamaterial behavior.
- 4- Since the U-slots have been embedded into the microstrip line, using a thicker substrate leads to a broader microstrip line. Wider microstrip line offers more flexibility in choosing the slot width, thus the limit on the fabrication resolution is relaxed.
- 5- The loss tangent of the substrate affects the insertion loss at the passband. A low loss substrate is needed to enhance the reflection coefficient across the reject-band and reduce the insertion loss across the pass-band. The conventional FR4 substrate (loss tangent 0.025) achieved an insertion loss of -1.55dB at 4GHz. Meanwhile, if the loss tangent is assumed to be 0.0025, the insertion loss can be decreased to -0.67dB.
- 6- The visualization of the electric field around the U-slots gives a good insight into the operation of the band rejection. The electric field vector in the two legs U-slot at the frequencies of the reject-band is in opposite directions, and the field is maximum at the center of the slot reaching zero at both ends. This represents a $\frac{1}{2}$ effective wavelength, in which the field opposition come from the folding of the slot. In two U-slots, the field magnitude is maximum at the region between the opposite two slots, and thus the coupling is larger than that for the face-face arrangement. The interlaced U-slots, experience higher mutual coupling between the two U-slots due to the very close proximity of the four legs of the two U-slots.
- 7- Due to the opposite E-field direction between the two legs of the folded U-slot, the radiated field from the microstrip line has a minimal value at the resonance frequency. This is an added benefit in comparison with the designs using a defected ground plane, where some radiation is inevitable from the backside.

- 8- The testing of the fabricated prototypes shows a good agreement with the simulation results, thus verifying the proposed idea and the new design structure.
- 9- The folded slot into a U-shape can be applied to Frequency Selective Surfaces (FSS), where two designs are demonstrated. The first design uses an array of U-shaped conducting strips printed on a dielectric sheet that achieves band-reject property. The other one is an array of slots etched in a conducting screen that achieves band-pass property. It is observed that the structural parameters of the U-shaped FSS influence the resonance frequency of the transfer function. The behavior of the two FSS designs depends on the direction of the E-field of the incident wave with respect to the strip or slot.
- 10- The visualization of the electric field around the U-slots and the current density on the conducting strip give a good insight into the frequency selective property. The strip resonates when its length is an integer multiple of half the guided wavelength. The slot shows a similar trend. The two resonances are also influenced by the relative orientation of the E-field.
- 11- The extracted effective parameters confirm the negative values of the permittivity, and the permeability that occur near the required resonance frequency for which the slot exhibits a metamaterial behavior.

5.2 Future Work

The current work can be further extended by considering the following modifications:

- 1- Using two U-slots of different lengths to achieve dual-band-reject filter.
- 2- Investigating the radiated field from the filter when the slot is etched in the ground plane.

- 3- Investigating the two methods (Nicolson-Ross-Weir (NRW) approach and Fresnel relations) for estimating the effective permeability and permittivity and the refractive index and comparing their accuracies.

REFERENCES

References

- [1] J. A. KONG, “Electromagnetic Wave Theory,” *EMW Publishing*, 2008.
- [2] J. B. Pendry, A. J. Holden, W. J. Stewart, and I. Youngs, “Extremely Low Frequency Plasmons In Metallic Mesostructures,” *Physical Review Letters*, Vol. 76, No. 25, PP. 4773–4776, 1996.
- [3] V. G. Veselago, “The Electrodynamics Of Substances With Simultaneously Negative Values Of ϵ And μ ,” *Soviet Physics Uspekhi*, Vol. 10, No. 4, PP. 509–514, 1968.
- [4] R. W. Ziolkowski, “Metamaterial-Based Antennas: Research And Developments,” *IEICE Transactions on Electronics*, Vol. E89-C, No. 9, PP. 1267–1275, 2006.
- [5] S. J. Pendry, “Metamaterials And The Control Of Electromagnetic Fields,” *Conference on coherence and quantum optics. Optical Society of America*, 2007.
- [6] S. Hrabar, J. Bartolic, and Z. Sipus, “Waveguide Miniaturization Using Uniaxial Negative Permeability Metamaterial,” *IEEE Transactions on Antennas and Propagation*, Vol. 53, No. 1, PP. 110–119, 2005.
- [7] J. B. Pendry, A. Holden, D. Robbins, and W. Stewart, “Low Frequency Plasmons In Thin Wire Structures,” *Journal of Physics: Condensed Matter*, Vol. 10, No. 22, PP. 4785–4809, 1998.
- [8] J. B. Pendry, A. J. Holden, D. J. Robbins, and W. J. Stewart, “Magnetism From Conductors And Enhanced Nonlinear Phenomena,” *IEEE Transactions on Microwave Theory and Techniques*, Vol. 47, No. 11, PP. 2075–2084, 1999.
- [9] J. B. Pendry, “Negative Refraction Makes A Perfect Lens,” *Physical Review Letters*, Vol. 85, No. 18, PP. 1–4, 2000.
- [10] D. R. Smith, W. J. Padilla, D. C. Vier, S. C. Nemat-Nasser, and S. Schultz, “Composite Medium With Simultaneously Negative Permeability And Permittivity,” *Physical Review Letters*, Vol. 84, No. 18, PP. 4184–4187, 2000.
- [11] P. M. Library, R. A. Shelby, D. R. Smith, and S. Schultz, “Experimental Verification Of A Negative Index Of Refraction,” *Science*, Vol. 292, No. 5514, PP. 77–79, 2001.
- [12] D. R. Smith and N. Kroll, “Negative Refractive Index In Left-Handed

- Materials,” *Physical Review Letters*, Vol. 85, No. 14, PP. 2933–2936, 2000.
- [13] R. A. Shelby, D. R. Smith, S. C. Nemat-Nasser, and S. Schultz, “Microwave Transmission Through A Two-Dimensional, Isotropic, Left-Handed Metamaterial,” *Applied Physics Letters*, Vol. 78, No. 4, PP. 489–491, 2001.
- [14] F. Falcone *et al.*, “Babinet Principle Applied To The Design Of Metasurfaces And Metamaterials,” *Physical Review Letters*, Vol. 93, No. 19, PP. 1–4, 2004.
- [15] H. Chen *et al.*, “Left-Handed Materials Composed Of Only S-Shaped Resonators,” *Physical Review E*, Vol. 70, No. 5, PP. 1–4, 2004.
- [16] L. Ran, J. Huangfu, H. Chen, X. Zhang, and K. Cheng, “Experimental Study On Several Left-Handed Metamaterials,” *Progress In Electromagnetics Research , PIER*, Vol. 51, PP. 249–279, 2005.
- [17] J. García-García *et al.*, “Comparison Of Electromagnetic Band Gap And Split-Ring Resonator Microstrip Lines As Stop Band Structures,” *Microwave and Optical Technology Letters*, Vol. 44, No. 4, PP. 376–379, 2005.
- [18] J. García-García *et al.*, “Microwave Filters With Improved Stopband Based On Sub-Wavelength Resonators,” *IEEE Transactions on Microwave Theory and Techniques*, Vol. 53, No. 6, PP. 1997–2006, 2005.
- [19] B. Wu, B. Li, T. Su, and C.-H. Liang, “Study On Transmission Characteristic Of Split-Ring Resonator Defected Ground Structure,” *PIERS Online*, Vol. 2, No. 6, PP. 710–714, 2006.
- [20] J. Zhou, T. Koschny, L. Zhang, G. Tuttle, and C. M. Soukoulis, “Experimental Demonstration Of Negative Index Of Refraction,” *Applied Physics Letters*, Vol. 3, No. 6, PP. 791–797, 2006.
- [21] P. Pan, Q. Wu, F. Y. Meng, F. Zhang, and J. Lee, “A Novel Compact Left-Handed Transmission Line With Improved Split-Ring Resonators,” *Asia-Pacific Microwave Conference Proceedings, APMC*, PP. 1–4, 2007.
- [22] M. Gil, J. Bonache, J. Selga, J. Garcia-Garcia, and F. Martin, “High-Pass Filters Implemented By Composite Right/Left Handed (CRLH) Transmission Lines Based On Complementary Split Rings Resonators (CSRRs),” *PIERS Online*, Vol. 3, No. 3, PP. 251–253, 2007.

- [23] E. Ekmekçi and G. Turhan-Sayan, "Investigation Of Effective Permittivity And Permeability For A Novel V-Shaped Metamaterial Using Simulated S-Parameters," *5th International Conference on Electrical and Electronics Engineering*, PP. 251–254, 2007.
- [24] R. S. Kshetrimayum, S. Kallapudi, and S. S. Karthikeyan, "Stop Band Characteristics For Periodic Patterns Of CSRRs In The Ground Plane And Its Applications In Harmonic Suppression Of Band Pass Filters," *International Journal of Microwave and Optical Technology*, Vol. 3, No. 2, PP. 88–95, 2008.
- [25] N. Amiri, K. Forooghi, and Z. Atlasbaf, "Design And Simulation Of A Novel Double Negative Metamaterial," *Asia Pacific Microwave Conference*, PP. 728–730, 2009.
- [26] S. Fallahzadeh and M. Tayarani, "A Compact Microstrip Bandstop Filter," *Progress in Electromagnetics Research Letters*, Vol. 11, PP. 167–172, 2009.
- [27] Hu Qi, Xu Jun, Wang Mao-yan, and Liu Yu, "Novel Cross-Coupled Filters Using Metamaterial Split Ring Resonators," *International Conference on Microwave Technology and Computational Electromagnetics (ICMTCE)*, PP. 155–157, 2009.
- [28] Z. Ya-Nan and D. Ling-Ling, "Metamaterial Transmission Lines Based On Split-Ring Resonators (SRRs) And Complementary Split-Ring Resonators (CSRRs)," *International Conference on Microwave and Millimeter Wave Technology, ICMMT*, PP. 2075–2077, 2010.
- [29] K. Lu, G. M. Wang, and H. X. Xu, "Compact And Sharp-Rejection Bandstop Filter Using Uniplanar Double Spiral Resonant Cells," *Radio engineering*, Vol. 20, No. 2, PP. 468–471, 2011.
- [30] M. Naghshvarian-Jahromi and M. Tayarani, "Defected Ground Structure Band-Stop Filter By Semicomplementary Split Ring Resonators," *IET Microwaves, Antennas & Propagation*, Vol. 5, No. 11, PP. 1386–1391, 2011.
- [31] S. Sahu, R. K. Mishra, and D. R. Poddar, "Compact Metamaterial Microstrip Low-Pass Filter," *Journal of Electromagnetic Analysis and Applications*, Vol. 3, No. 10, PP. 399–405, 2011.
- [32] M. K. Ouda and N. A. Abutahoun, "A Novel Infinity Shaped Split Ring Resonator To Form A New Metamaterial," *IUG Journal of Natural and Engineering Studies*, Vol. 20, No. 2, PP. 117–125, 2012.

- [33] O. Turkmen, E. Ekmekci, and G. Turhan-Sayan, "Nested U-Ring Resonators: A Novel Multi-Band Metamaterial Design In Microwave Region," *IET Microwaves, Antennas & Propagation*, Vol. 6, No. 10, PP. 1102–1108, 2012.
- [34] Haider Raad, H. Al-Rizzo, A. Abbosh, and S. Abushamleh, "A Novel μ -Negative Metamaterial With Enhanced Rejection Bandwidth," *American Journal of Engineering and Applied Sciences*, Vol. 6, No. 2, PP. 137–144, 2013.
- [35] A. Mallik, S. Kundu, and O. Goni, "Design Of A Novel Two-Rectangular U-Shaped Double Negative Metamaterial," *International Conference on Informatics, Electronics and Vision (ICIEV)*, PP. 1–6, 2013.
- [36] S. S. Islam, M. R. I. Faruque, and M. T. Islam, "The Design And Analysis Of A Novel Split-H-Shaped Metamaterial For Multi-Band Microwave Applications," *Materials*, Vol. 7, No. 7, PP. 4994–5011, 2014.
- [37] T. Nesimoglu and C. Sabah, "Characterization Of Metamaterials Using A New Design And Measurement Technique For Microstrip Circuit Applications," *14th Mediterranean proceedings IEEE microwave symposium (MMS)*, PP. 1–4, 2014.
- [38] M. Bhaskar, J. Jasmi, and T. Mathew, "Microstrip Bandstop Filters Based On Hexagonal Complementary Split Ring Resonators," *Proceedings-5th International Conference on Advances in Computing and Communications (ICACC)*, PP. 311–313, 2015.
- [39] M. I. Hossain, M. R. I. Faruque, M. T. Islam, and M. H. Ullah, "A New Wide-Band Double-Negative Metamaterial For C- And S-Band Applications," *Materials*, Vol. 8, No. 1, PP. 57–71, 2015.
- [40] M. M. Hasan, M. R. I. Faruque, S. S. Islam, and M. T. Islam, "A New Compact Double-Negative Miniaturized Metamaterial For Wideband Operation," *Materials*, Vol. 9, No. 10, PP. 1–12, 2016.
- [41] V. S. A. Krishna, S. Sadasivam, P. R. Sreeram, and S. K. Menon, "Analysis And Design Of Direct Coupled Metamaterial Filters For Wireless Communication," *International Conference on Control Instrumentation Communication and Computational Technologies, (ICCICCT)*, PP. 663–665, 2016.
- [42] T. Ali, M. Saadh, A. Reva Itm, and R. C. Biradar, "A Novel

- Metamaterial Rectangular CSRR With Pass Band Characteristics At 2.95 And 5.23 GHz,” *2nd IEEE International Conference On Recent Trends in Electronics Information & Communication Technology (RTEICT)*, PP. 256–260, 2017.
- [43] B. George, N. S. Bhuvana, and S. K. Menon, “Design Of Edge Coupled Open Loop Metamaterial Filters,” *Progress in Electromagnetics Research Symposium -Spring (PIERS)*, PP. 2483–2488, 2017.
- [44] K. L. Smith and R. S. Adams, “Spherical Spiral Metamaterial Unit Cell For Negative Permeability And Negative Permittivity,” *IEEE Transactions on Antennas and Propagation*, Vol. 66, No. 11, PP. 6425–6428, 2018.
- [45] D. K. Choudhary and R. K. Chaudhary, “A Compact CPW-Based Dual-Band Filter Using Modified Complementary Split Ring Resonator,” *International Journal of Electronics and Communications*, Vol. 89, PP. 110–115, 2018.
- [46] M. J. Alam, M. R. I. Faruque, M. J. Hossain, M. T. Isla, and S. Abdullah, “Depiction Of A Combined Split P-Shaped Compact Metamaterial For Dual-Band Microwave Application,” *Proceedings of the Second International Conference on the Future of ASEAN (ICoFA)*, Vol. 2, PP. 235–244, 2018.
- [47] D. Marathe and K. Kulat, “A Compact Dual, Triple Band Resonators For Negative Permittivity Metamaterial,” *AEU - International Journal of Electronics and Communications*, Vol. 88, No. February, PP. 157–165, 2018.
- [48] M. Danaeian, K. Afrooz, and A. Hakimi, “Miniaturization Of Substrate Integrated Waveguide Filters Using Novel Compact Metamaterial Unit-Cells Based On SIR Technique,” *AEU - International Journal of Electronics and Communications*, Vol. 84, PP. 62–73, 2018.
- [49] A. Lai, C. Caloz, and T. Itoh, “Composite Right/Left-Handed Transmission Line Metamaterials,” *IEEE Microwave Magazine*, Vol. 5, No. 3, PP. 34–50, 2004.
- [50] F. J. H. Martínez, “Metamaterial-Loaded Printed Antennas: Design And Applications,” *PhD. Thesis, Universidad Carlos III De Madrid*, 2010.
- [51] S. Takeda and T. Yoshinaga, “Left-Handed Metamaterial Technologies Significant For Information And Communication Devices,” *Science and Technology Trends*, 2009.

- [52] N. Engheta and R. W. Ziolkowski, "A Positive Future For Double-Negative Metamaterials," *IEEE Transactions on Microwave Theory and Techniques*, Vol. 53, No. 4, PP. 1535–1555, 2005.
- [53] I. A. I. Al-naib, C. Jansen, and M. Koch, "Compact CPW Metamaterial Resonators For High Performance Filters," *In tech Open*, PP. 429–451, 2008.
- [54] J. D. Baena *et al.*, "Equivalent-Circuit Models For Split-Ring Resonators And Complementary Split-Ring Resonators Coupled To Planar Transmission Lines," *IEEE Transactions on Microwave Theory and Techniques*, Vol. 53, No. 4, PP. 1451–1460, 2005.
- [55] R. Marques, F. Mesa, J. Martel, and F. Medina, "Comparative Analysis Of Edge- And Broadside- Coupled Split Ring Resonators For Metamaterial Design - Theory And Experiments," *IEEE Transactions on Antennas and Propagation*, Vol. 51, No. 10, PP. 2572–2581, 2003.
- [56] J. Martel *et al.*, "A New LC Series Element For Compact Bandpass Filter Design," *IEEE Microwave and Wireless Components Letters*, Vol. 14, No. 5, PP. 210–212, 2004.
- [57] X. Chen, T. M. Grzegorzczak, B. I. Wu, J. Pacheco, and J. A. Kong, "Robust Method To Retrieve The Constitutive Effective Parameters Of Metamaterials," *Physical Review E*, Vol. 70, No. 1, PP. 1–7, 2004.
- [58] Z. Szabó, G. Park, R. Hedge, and E. Li, "A Unique Extraction Of Metamaterial Parameters Based On Kramers – Kronig Relationship," *IEEE Transactions on Microwave Theory and Techniques*, Vol. 58, No. 10, PP. 2646–2653, 2010.
- [59] M. Hasan, M. Faruque, and M. Islam, "Compact Left-Handed Meta-Atom For S-, C- And Ku-Band Application," *Applied Sciences*, Vol. 7, No. 10, P. 1071, 2017.
- [60] M. Z. Mahmud, M. T. Islam, N. Misran, M. J. Singh, and K. Mat, "A Negative Index Metamaterial To Enhance The Performance Of Miniaturized UWB Antenna For Microwave Imaging Applications," *Applied Sciences (Switzerland)*, Vol. 7, No. 11, 2017.
- [61] M. G. Barba, "Resonant-Type Metamaterial Transmission Lines And Their Application To Microwave Device Design," *PhD.Thesis, Universitat Autònoma de Barcelona*, PP. 1–176, 2009.
- [62] C. Liu and K. Huang, "Metamaterial Transmission Line And Its Applications," *Advanced Microwave and Millimeter Wave Technologies*

- Semiconductor Devices Circuits and Systems*, PP. 249–274, 2010.
- [63] R. S. Kshetrimayum, “A Brief Intro To Metamaterials,” *IEEE Potentials*, Vol. 23, No. 5, PP. 44–46, 2004.
- [64] D. Schurig *et al.*, “Metamaterial Electromagnetic Cloak At Microwave Frequencies,” *Science*, Vol. 314, No. 5801, PP. 977–980, 2006.
- [65] J. B. Pendry, D. Schurig, and D. R. Smith, “Controlling Electromagnetic Fields. Supporting Info,” *Science*, Vol. 312, No. 5781, PP. 1780–1782, 2006.
- [66] K. M. K. H. Leong, C. J. Lee, and T. Itoh, “Compact Metamaterial Based Antennas For MIMO Applications,” *International workshop on Antenna Technology: Small and Smart Antennas Metamaterials and Applications. IEEE*, No. 1, PP. 87–90, 2007.
- [67] J. Bonache, I. Gil, J. García-García, and F. Martín, “Novel Microstrip Bandpass Filters Based On Complementary Split-Ring Resonators,” *IEEE Transactions on Microwave Theory and Techniques*, Vol. 54, No. 1, PP. 265–271, 2006.
- [68] M. Gil, J. Bonache, I. Gil, J. García-garcía, and F. Martín, “Artificial Left-Handed Transmission Lines For Small Size Microwave Components : Application To Power Dividers,” *European Microwave Conference*, PP. 1135–1138, 2006.
- [69] I. Gil, J. Bonache, J. García-García, F. Falcone, and F. Martín, “Metamaterials In Microstrip Technology For Filter Applications,” *IEEE Antennas and Propagation Society International Symposium*, Vol. 1 A, PP. 668–671, 2005.
- [70] L. Jiusheng and D. Tieying, “Application Of Metamaterial Unit Cell In Bandpass Filter,” *Microwave and Optical Technology Letters*, Vol. 49, No. 9, PP. 2109–2111, 2007.
- [71] R. N. Baral and P. K. Singhal, “Miniaturized Microstrip Bandpass Filter Using Coupled Metamaterial Resonators,” *International Journal Of Microwave and Optical Technology*, Vol. 4, No. 2, PP. 115–118, 2009.
- [72] F. Falcone, T. Lopetegi, J. D. Baena, R. Marqués, F. Martín, and M. Sorolla, “Effective Negative- ϵ Stopband Microstrip Lines Based On Complementary Split Ring Resonators,” *IEEE Microwave and Wireless Components Letters*, Vol. 14, No. 6, PP. 280–282, 2004.
- [73] Z. M. Thomas, T. M. Grzegorzcyk, B.-I. Wu, and J. A. Kong, “Enhanced

- Microstrip Stopband Filter Using A Metamaterial Substrate,” *Microwave and Optical Technology Letters*, Vol. 48, No. 8, PP. 1522–1525, 2006.
- [74] A. Abid and H. Zhirun, “Sharp Cut-Off, Miniaturized Metamaterial Binomial Microstrip Low-Pass Filter,” *Microwave and Optical Technology Letters*, Vol. 49, No. 10, PP. 2406–2409, 2007.
- [75] K. Annaram and S. Nithya, “Investigation Of Compact Low Pass Filter With Sharp Cut – Off Using Metamaterial,” *Radio engineering*, Vol. 22, No. 3, PP. 729–733, 2013.
- [76] S. Suganthi, S. Raghavan, and D. Kumar, “Study Of Performance Improvement On The Design Of Compact SRR Embedded Microstrip Low Pass Filter,” *Progress In Electromagnetics Research Symposium Proceedings*, PP. 783–788, 2012.
- [77] A. Duvey, S. Sharma, and G. Sharma, “Design Of Metamaterial Based High Pass Filter Using CSRR At Cut Off Frequency 0.9 Ghz,” *International Journal of Engineering Research*, Vol. 1, No. 2, PP. 34–35, 2012.
- [78] D. Pozar, “Microwave Engineering,” in *John Wiley & Sons Inc.*, 2005, PP. 1–756.
- [79] S. Yang, “A Dual-Band Bandstop Filter Having Open Stubs And Two Equivalent T-Shaped Lines,” *International Journal of Electromagnetics and Applications*, Vol. 5, No. 3, PP. 108–111, 2015.
- [80] L. Chiu and Q. Xue, “A Simple Microstrip Bandstop Filter Using Cross-Coupling Stubs,” *International Journal of Microwave Science and Technology*, PP. 1–6, 2012.
- [81] S. Ramya and I. S. Rao, “Design Of Compact Ultra-Wideband Microstrip Bandstop Filter Using Split Ring Resonator,” *IEEE International Conference on Communication and Signal Processing, ICCSP*, PP. 105–108, 2015.
- [82] I. Transactions and C. Pyo, “Novel U-Slot And V-Slot DGSs For Bandstop Filter With Improved Q Factor,” *IEEE transactions on microwave theory and techniques*, Vol. 54, No. 6, PP. 2840–2847, 2006.
- [83] B. Belkadi, Z. Mahdjoub, and M. L. Seddiki, “Design And Analysis Of Dual-Band Rejection Microwave Filter Employing SRR,” *5th International Conference on Electrical Engineering*, PP. 1–7, 2017.

- [84] Q. Bu, J. Ding, and C. J. Guo, “New Design Of Ultra-Wideband Bandpass Filter Using Interdigitated Coupled Lines CRLH-TL Structure,” *10th International Symposium on Antennas, Propagation and EM Theory*, PP. 486–489, 2012.
- [85] G. S. A. Shaker and S. Safavi-naeini, “Microstrip Band Rejection Filter Using Open Loop Resonator,” *Microwave and Optical Technology Letters*, Vol. 50, No. 5, PP. 1550–1551, 2008.
- [86] A. Boutejdar and S. D. Bennani, “Design And Fabrication Of Tri-Stopband Bandstop Filters Using Cascaded And Multi-Armed Methods,” *Advanced Electromagnetics*, Vol. 6, No. 3, PP. 18–24, 2017.

الخلاصة

في هذه الدراسة، تم استخدام خصائص الميتاماتيريال (metamaterial) لاقتراح تصميم مرشحات مانعة للحزمة تناسب منظومات (WLAN). تشترك المرشحات المقترحة باحتوائها على عنصر رنين على شكل شق مطوي على هيئة الحرف U. تم تضمين الشق في خط الشريط الدقيق (Microstrip Line)، وبهذا يكون طول المرشح ربع الطول الموجي المؤثر، ولا يزيد عرض المرشح عن عرض الخط الشريطي الدقيق. يتميز التصميم المقترح بصغر حجمه مقارنة بالمرشحات التي تستخدم عناصر رنين أخرى مثل: الحلقات أو دوائر الايتر المفتوحة النهاية أو المقصورة النهاية (open and short circuited stubs).

تم تصميم ودراسة أربعة مرشحات، أحتوى المرشح الأول على شق واحد على شكل حرف U، فيما ضم كل من المرشحات الثلاثة الأخرى شقين على شكل الحرف U، وضعت بإحدى الهيئات الثلاث: وجهًا لوجه أو ظهرًا لظهر أو بشكل متداخل. أجريت دراسة مستفيضة لخواص المرشحات المصممة باستخدام برنامج (CST Microwave Studio). بسبب طبي الشق على شكل الحرف U يكون المجال الكهربائي (E-field) داخل الساقين في اتجاهين متعاكسين وهذا يجعل الإشعاع الصادر من الشق الى خارج المرشح في قيمته الدنيا وبما يخفض الخسائر في المرشح.

تم استخراج السماحية والنفاذية المؤثرتين من القيم المحسوبة لمعامل التمرير ومعامل الانعكاس، حيث تبين أن المرشحات المقترحة تسلك سلوك الميتاماتيريال (metamaterial). تم التحقق من صحة التصاميم المقترحة بالقياسات العملية التي أجريت على النماذج المطبوعة باستخدام محلل الشبكات المتجه (Vector Network Analyzer).

بناء على ما تقدم فقد استخدمت الخاصية الانتقائية للتردد التي أظهرها الشق ذو شكل الحرف U في تصميم الأسطح المختارة للتردد (FSS). استخدمت الشريحة الموصلة المطبوعة على ركيزة

عازلة والشق المحفور في سطح موصل لتنفيذ فكرة الأسطح المختارة للتردد، حيث تمت المحاكات باستخدام طريقة الخلية الواحدة وبرنامج (CST Microwave Studio). لوحظ أن اتجاه المجال الكهربائي للموجة الساقطة نسبة الى امتداد الشق أو الشريحة ذو تأثير كبير في سلوك السطح المختار للتردد (FSS). أظهرت اختبارات كل من توزيع المجال الكهربائي داخل الشق وتوزيع كثافة التيار على سطح الشريحة حالة رنين عندما يكون طول الشق أو الشريحة عددًا صحيحًا من مضاعفات نصف الطول الموجي المؤثر (effective wavelength). دراسة نمط الإشعاع الناتج عن الموجة المنتقلة خلال السطح المختار للتردد أكدت صحة نتائج خصائص انتقال الموجة خلال السطح في حالتها منع الحزمة بالنسبة للشريحة على شكل حرف U وحالة تمرير الحزمة بالنسبة للشق على شكل حرف U. وأظهرت النتائج المحسوبة للسماحية والنفاذية المؤثرة على خصائص الميتاماتيريال (metamaterial) للسطوح مختارة التردد المقترحة في هذه الدراسة.



جامعة الموصل

كلية هندسة الالكترونيات

دراسة حول تطبيقات الميتاماتيريال (Metamaterial) في نبائط الموجات الدقيقة

رسالة تقدم بها

مأمون عمار الاطرقجي

إلى

مجلس كلية هندسة الالكترونيات

جامعة الموصل

كجزء من متطلبات نيل شهادة الماجستير

في

هندسة الاتصالات

بإشراف

الأستاذ الدكتور خليل حسن سيد مرعي

الأستاذ الدكتور رائد عبدالحميد